



POLITECNICO
DI TORINO



Master's Thesis

Master of Science in NANOTECHNOLOGIES FOR ICTS

Academic Year 2018/2019

Novel field emission devices for vacuum nanoelectronics and optoelectronic applications

Author: Alberto NARDI

Advisor: Karl K. BERGGREN

Co-advisor: Phillip D. KEATHLEY

Supervisor: Fabrizio GIORGIS

Co-supervisor: Carlo RICCIARDI



Massachusetts
Institute of
Technology

Abstract

Novel field emission devices for vacuum nanoelectronics and optoelectronic applications

There has been a recent surge of interest in nanostructured materials for vacuum nanoelectronic devices and optoelectronic applications. Specifically, the high electric fields surrounding a nanostructure can create highly nonlinear tunnelling currents across few-nanometer free-space gaps. Such nanostructures can be used for creating low-power, high-speed nonlinear electronic circuit elements for operation in harsh environments, or novel optoelectronic devices exhibiting petahertz-level bandwidths. While noble metals exhibit high field enhancement, especially in the optical regime due to their plasmonic behavior, they are prone to damage and performance degradation because of their low melting point. Refractory plasmonic materials are promising for applications in harsh environments due to their high bulk melting point. Titanium nitride is a refractory and CMOS-compatible alternative material for plasmonic applications. The tunability of its optical properties by adding Si and O₂ dopants was recently demonstrated, enabling many applications. In this work, we simulated the optical response of titanium silicon oxynitride (TiSiON) bow-tie nanoantennas, highlighting their advantages and drawbacks with respect to noble metals and other materials. We also pointed out the influence of the geometry on their optical response. We successfully developed a reliable cleanroom etching procedure to fabricate bow-tie nanostructures arrays with sub-10-nm wide gaps and aspect ratio larger than 5. We performed electrical and optical testing on fabricated arrays. We obtained an electric current of 5 nA/tip with a bias voltage of 10 V in an array of about 2000 bow-tie nanostructures with an average gap size of 14 nm. From the same array, we obtained a photocurrent of 150 nA/tip using an incident laser with a power of 13 mW and an applied bias voltage of 5 V. We also demonstrated that TiSiON has not degraded with testing, when not electromigrated. In conclusion, we proved the suitability of titanium silicon oxynitride for vacuum nanoelectronics and optoelectronic applications. With further optimization, TiSiON could be a good candidate to replace the state-of-the-art materials and improve the performances of the devices in harsh environments.

Résumé

Nouveaux dispositifs d'émission de champ pour les nanoélectroniques sous vide et les applications optoélectroniques

Récemment il y avait une augmentation d'intérêt dans les matériaux nanostructurés pour les dispositifs nanoélectroniques sous vide et les applications optoélectroniques. Spécifiquement, les champs forts autour d'une nanostructure peuvent créer des courants de tunnel très non linéaire qui travers des fentes vides de quelques nanomètres. Ces nanostructures peuvent être utilisées pour créer des éléments de circuits électronique non linéaire de faible puissance et haut vitesse pour fonctionnement dans les milieux hostiles, ou nouveaux dispositifs optoélectroniques avec une bande passante spectrale de largeur de niveau petahertz. Tandis que les métaux nobles présentent une forte augmentation de champs, en particulier dans le régime optique en raison de leur comportement plasmonique, ils sont sensibles aux dommages et à la dégradation des performances à cause de leur bas point de fusion. Par contre, les matériaux plasmoniques réfractaires sont prometteurs pour les applications dans les milieux hostiles en raison de leur point de fusion élevé. Le nitrure de titane est un matériau possible pour les applications plasmoniques qui est aussi réfractaire et compatible avec CMOS. L'accordabilité de ses propriétés optiques en ajoutant des dopants Si et O₂ a été récemment démontrée, permettant de nombreuses applications. Dans cette thèse, on a simulé la réponse optique des nanoantennes en forme nœud papillon de oxynitrure de silicium titane (TiSiON), en soulignant leurs avantages et inconvénients par rapport aux matériaux nobles et aux autres matériaux. On a également souligné l'influence de la géométrie de leur réponse optique. On a mis en point avec succès une procédure fiable de graveur en salle blanche pour la fabrication des réseaux nanostructures en forme nœud papillon avec des fentes vides inférieur à 10 nm et un rapport largeur supérieur à 5. On a effectué des tests électriques et optiques sur des réseaux fabriqués. On a obtenu un courant électrique de 5 nA/pointe avec une tension appliquée de 10 V dans un réseau d'environ 2000 nanostructures en forme nœud papillon avec une fente moyenne de 14 nm. À partir du même réseau, on a obtenu un photocourant de 150 nA/pointe induit par un laser incident avec un puissance moyen de 13 mW et une tension appliquée de 5 V. On a démontré que TiSiON ne s'était pas dégradé avec les tests, lorsqu'il n'était pas électromigré. En conclusion, on a prouvé que l'oxynitrure de silicium titane convient aux applications de la nanoélectronique sous vide et de l'optoélectronique. Avec une optimisation supplémentaire, TiSiON pourrait être intéressant de remplacer les matériaux de pointe et améliorer la performance des dispositifs dans les milieux hostiles.

Sintesi

Nuovi dispositivi ad emissione di campo per nanoelettronica nel vuoto ed applicazioni optoelettroniche

Recentemente si é assistito ad un aumento di interesse verso materiali nanostrutturati per dispositivi nanoelettronici nel vuoto e per applicazioni optoelettroniche. In particolare, elevati campi elettrici circondanti una nanostruttura possono creare correnti di tunnel altamente non lineari attraverso spazi di qualche nanometro nel vuoto. Queste nanostrutture possono essere utilizzate per creare elementi non lineari per circuiti elettronici a bassa potenza e ad alta velocità per operare in ambienti ostili, o nuovi dispositivi optoelettronici con una banda passante al livello dei petahertz. Nonostante i metalli nobili presentino un elevato aumento del campo, soprattutto nel regime ottico grazie al loro comportamento plasmonico, essi sono predisposti a danni e a degradazione delle prestazioni a causa dei loro bassi punti di fusione. I materiali plasmonici refrattari sono promettenti per applicazioni in ambienti ostili, dati i loro punti di fusione elevati. Il nitrato di titanio é un materiale refrattario alternativo per applicazioni plasmoniche che é anche compatibile con la tecnologia CMOS. É stata recentemente dimostrata la possibilità di modificare le proprietà ottiche del nitrato di titanio aggiungendo Si e O₂ come dopanti, permettendo numerose applicazioni. In questa tesi, si é simulato la risposta ottica di nanoantenne a forma di papillon fatte di ossinitrato di silicio e titanio (TiSiON), mettendone in risalto i vantaggi e gli svantaggi rispetto ai metalli nobili e ad altri materiali. Si é anche analizzato l'influenza della geometria sulla loro risposta ottica. Si é sviluppato con successo un processo di etching in cleanroom affidabile per fabbricare matrici di nanostrutture a forma di papillon con spazi inferiori a 10 nm e aspect ratio maggiore di 5. Si sono effettuati test elettrici e ottici su delle matrici fabbricate. Si é ottenuta una corrente elettrica di 5 nA/punta con una tensione di bias di 10 V per una matrice di circa 2000 nanostrutture a forma di papillon con una dimensione media degli spazi di 14 nm. Dalla stessa matrice, si é ottenuta una fotocorrente di 150 nA/punta usando un laser incidente con una potenza di 13 mW, applicando una tensione di bias di 5 V. Si é anche dimostrato che il TiSiON non si é danneggiato durante i test, nel caso in cui i dispositivi non siano stati elettromigrati. In conclusione, si é dimostrato l'adeguatezza dell'ossinitrato di silicio e titanio per nanoelettronica nel vuoto e applicazioni optoelettroniche. Con ulteriori ottimizzazioni, il TiSiON potrebbe essere un buon candidato per sostituire i materiali utilizzati fino ad ora e migliorare le prestazioni dei dispositivi in ambienti ostili.

Acknowledgements

This thesis represents the final piece of the puzzle that the last two years of my life have represented. It has been a wonderful and interesting journey full of experiences and great people to share them with. I would like to thank everyone who crossed their path with mine: it has been a blast.

I would like to thank my advisor, Prof. Karl K. Berggren, for giving me the opportunity to join the QNN group, for his advices and for creating an awesome friendly environment in the group.

A heartfelt thank you goes to Phillip D. Keathley, for his experience, the constant guidance he provided throughout the whole project, and his friendly approach that never made me feel uncomfortable or inadequate, even during the toughest periods. I have a new example to follow in my life from now on.

I am thankful to Marco Turchetti for everything he taught me, for his limitless patience and the help and support he gave me during every day I spent in the group.

To Mina Bionta and the whole "*we don't superconduct*" part of the QNN group for all the laughs, the meals and friendly moments we shared: I have never felt like I was working when we were together.

To Akshay Agarwal for his kindness and great experience with FIB and TEM lamella preparation.

To Marco Colangelo for his unstoppable charisma, incredible passion and readiness to help whenever there was a problem.

To the whole QNN group for the great atmosphere we can breath in the office. It hasn't just been a place to work in, but a friendly environment for sharing life.

To Mark K. Mondol and Jim Daley for their technical knowledge on nanofabrication and for making everything possible in the NanoStructures Laboratory.

To Nicoletta, Flavia, Fiorenza and Giulia for their friendship and great support even with an ocean and some thousands kilometres separating us. There are challenges I couldn't have faced without them. I am glad to have them in my life.

To my whole family for being my first supporters, for letting me follow my dreams from the very beginning and never pulling me back, for helping me to build my life together step by step. It is a great example for me to follow, and, as you know, I will always come back home.

To my grandmother, nonna Marcella, for always pushing me over my limits even though that implies being so far apart. I have fought for both of us.

And last, to myself for being happy of who I am, for always going on and believing in myself, and mostly for never forgetting what life means. With the heart full of hope that I will find many other pieces to add to my life. The puzzle isn't over.

Contents

1	Introduction	1
1.1	Field Electron Emission	2
1.2	Light-matter interactions and Surface Plasmon Resonances	5
1.2.1	Photoemission regimes	7
1.3	TiSiON as plasmonic nanostructure	9
1.4	Master's Thesis project	12
1.4.1	Motivation	12
1.4.2	Thesis's structure	13
2	Bow-ties FEM simulations	15
2.1	TiSiON film as deposited	16
2.1.1	Comparison with Au nanostructures	20
2.1.2	Comparison with other materials	26
2.1.3	Geometric parameters study	30
2.2	TiSiON film after annealing	41
3	Tools and techniques	47
3.1	Fabrication techniques	47
3.1.1	Electron Beam Lithography	47

3.1.2	Reactive Ion Etching	50
3.1.3	DWL - direct writing (photo)lithography	51
3.1.4	Focused Ion Beam	52
3.2	Characterization techniques	54
3.2.1	Ellipsometry	55
3.2.2	Transmission Electron Microscopy	58
4	Fabrication process for Titanium Silicon Oxynitride	63
4.1	Sputtering of the film	64
4.2	Elemental composition study	64
4.2.1	TEM lamella preparation	64
4.2.2	TEM analysis and EELS results	71
4.3	Material etch study: etchants comparison	75
4.3.1	CF ₄ /O ₂ plasma	78
4.3.2	CF ₄ plasma	79
4.3.3	Cl ₂ plasma	79
4.3.4	Other etchants for wet etching procedures	82
4.4	Investigation of hard masks for patterning nanostructures of TiSiON	83
4.4.1	Aluminum	86
4.4.2	Molybdenum	93
4.4.3	Titanium	93
4.4.4	Chromium	97
4.4.5	Aluminum/Chromium bi-layer	101
4.5	Bow-ties arrays patterning and pads fabrication	104
5	Electrical and optical testing	109

5.1	Electrical testing: experimental setup	110
5.2	Optical testing: experimental setup for photocurrent detection	110
5.3	TiSiON17: film as deposited	112
5.3.1	TiSiON17 set 6C	113
5.3.2	TiSiON17 set 6B: after electromigration	119
5.4	TiSiON19 set 7C: annealed film	127
6	Conclusions and future work	135
6.1	Summary	135
6.2	Results and conclusions	136
6.3	Future works	137

List of Figures

1.1	Schematics of Fowler-Nordheim emission mechanism. (a) Non-biased source and drain electrodes. (b) A current is flowing from the source to the drain due to a bias voltage, which reduces the tunnelling distance.	3
1.2	Schematics of both surface plasmon polaritons and localized surface plasmons. (a) Surface plasmon polaritons. The propagation is along the x- and y-directions, while the plasmon decays evanescently along the z-direction. (b) Localized surface plasmons for a sphere. The electron cloud of the metal sphere oscillates along the electric field direction. The plasmon does not propagate along the surface. [23]	6
1.3	Schematics of the four different photoemission regimes. (a) Photofield emission. (b) Multiphoton photoemission. (c) Above-threshold photoemission. (c) Tunnelling photoemission (or optical field emission). [32]	10
1.4	Comparison between different noble metals and refractory materials. Parameters in the axes: bulk melting point, crossover wavelength and imaginary part of the permittivity at 1000 nm. [31]	11
2.1	Electric field profiles of a pair of bow-ties with and without connector bars.	17

2.2	Permittivity components for TiSiON film as deposited.	19
2.3	Extinction spectra of both gold and TiSiON films. Gold has a very narrow peak, but it is an order of magnitude larger than the TiSiON one.	22
2.4	Comparison of Au and TiSiON transfer functions.	23
2.5	Field enhancement at the tip of both gold and TiSiON bow-ties structures.	24
2.6	Comparison of Au and TiSiON field profiles in time. The TiSiON response better resembles the incident pulse.	25
2.7	Comparison of extinction spectra and field enhancement of bow-ties made of different materials (TiSiON, Au, Al, Ti, TiN, W). (Altitude = 250 nm; Base/altitude ratio = 0.75; Metal thickness = 50 nm; ROC = 10 nm; Gap = 10 nm.)	28
2.8	Phase delay for different materials (TiSiON, Au, Al, Ti, TiN, W). . .	29
2.9	Normalized fields for aluminum. In red: normalized incident radiation. In blue: normalized excited radiation at the tip. Aluminum exhibits a similar behavior to gold.	30
2.10	Comparison of titanium and tungsten field profiles in time. They both show a similar behavior to TiSiON.	31
2.11	Normalized fields for TiN bow-tie structures. In red: normalized incident radiation. In blue: normalized excited radiation at the tip. . . .	32
2.12	Comparison of field enhancement and extinction spectrum with different altitude dimensions with and without the etched oxide. Continuous lines: with 50 nm of etched oxide. Dashed lines: no etched oxide. (Base/altitude ratio = 0.75; Metal thickness = 50 nm; ROC = 10 nm; Gap = 10 nm.)	34

2.13	Phase delay for different altitudes.	35
2.14	Comparison of field enhancement and extinction spectrum with different etched oxide thicknesses. (Altitude = 250 nm; Base/altitude ratio = 0.75; Metal thickness = 50 nm; ROC = 10 nm; Gap = 10 nm.)	36
2.15	Comparison of field enhancement and extinction spectrum with different base/altitude ratios. (Altitude = 250 nm; Metal thickness = 50 nm; Etched oxide thickness = 0 nm; ROC = 10 nm; Gap = 10 nm.) .	38
2.16	Field enhancement at the tip with different gap dimensions. (Altitude = 250 nm; Base/altitude ratio = 0.75; ROC = 10 nm; Metal thickness = 50 nm; Etched oxide thickness = 50 nm.)	39
2.17	Comparison of field enhancement and extinction spectrum with different connectors widths. (Altitude = 250 nm; Base/altitude ratio = 0.75; Metal thickness = 50 nm; Etched oxide thickness = 50 nm; ROC = 10 nm; Gap = 10 nm.)	40
2.18	Permittivity components for annealed TiSiON film.	43
2.19	Extinction spectra for different altitudes. Continuous lines: annealed film. Dashed lines: film as deposited.	44
2.20	Field enhancement for different altitudes. Continuous lines: annealed film. Dashed lines: film as deposited.	45
2.21	Phase delay for different altitudes. Continuous lines: annealed film. Dashed lines: film as deposited.	45
2.22	Incident field and excited field at the tip for a bow-tie structure with an altitude of 250 nm made of annealed TiSiON.	46
3.1	Schematic diagram of a FIB system. [41]	53
3.2	Schematic diagram of FIB platinum deposition process. [41]	54

3.3	Schematic diagram of a two-beam configuration, combining both a FIB and a SEM column. [41]	55
3.4	Model of light reflection in a three mediums system with different refractive indexes. Multiple reflections happen within the thin film and the total reflected light is given by the interference (constructive or destructive) of all the reflected contributions. [44]	56
3.5	Model of the spectroscopic ellipsometry principle. An incident linearly polarized beam is reflected on the surface of the sample. The reflected beam is elliptically polarized light. [44]	57
3.6	Schematic of a transmission electron microscope equipped for additional x-rays and electron energy loss spectroscopy. [42]	59
3.7	Schematic of a magnetic prism used for EELS. The paths inside the prism will depend on the speed, and so on the energy, of the electrons. An energy-loss spectrum is produced on a plane passing through the image point at the end of the prism. [43]	61
4.1	Setup of the FIB stage for a TEM lamella preparation. The sample, the TEM grid holder and the TEM copper grid are pointed out.	65
4.2	TEM lamella preparation. (a) Ion beam image showing the lamella after Pt deposition and trenches milling. (b) Pattern of the J-cut to perform with the ion beam at 30°. (c) Ion beam image of the J-cut. (d) Electron beam image of the J-cut. It images the opposite side with respect to the one we can see with the ion beam.	67

4.3	TEM lamella preparation. (a) Omniprobe insertion above the TEM lamella. (b) Pt deposition to anchor the omniprobe to the lamella. (c) Cut of the last part of the lamella that is keeping it connected to the sample. (d) Raise of the omniprobe and removal of the lamella from the sample.	69
4.4	TEM lamella preparation. (a) The lamella is placed on the TEM grid. (b) Pt deposition to anchor the lamella to the TEM grid. Mill the omniprobe in order to free the lamella. (c) TEM lamella attached to the TEM grid after omniprobe removal.	70
4.5	TEM lamella preparation. (a) Top view of the lamella after thinning. (b) Cross section of the TEM lamella after thinning. (c) Zoomed in top view of the lamella after thinning. The lamella thickness is smaller than 84 nm. (d) Zoomed in cross-section of the TEM lamella after thinning. The Pt protection layer is now about 100 nm thick. TiSiON is visible in the dark thin layer right under the platinum. A different composition in the oxide is present in the shallow oxide layer under TiSiON.	72
4.6	TEM image showing the e-beam deposited Pt layer, the TiSiON thin film and the silicon substrate.	73
4.7	TEM image at high magnification. The silicon substrate, the native oxide, the TiSiON thin film and its interface with the platinum protective layer are visible.	74
4.8	EELS line scan along the TiSiON thin film.	75
4.9	EELS spectrum. The energy for the location of the edges for TiSiON are highlighted.	76

4.10	Thickness (nm) versus time (min) of the etching of as deposited TiSiON with CF ₄ :O ₂ 9:1 sccm, at 10 mTorr. Both powers of 100 W and 200 W are shown.	80
4.11	Thickness (nm) versus time (min) of the etching of annealed TiSiON with CF ₄ :O ₂ 9:1 sccm, at 10 mTorr. Both powers of 100 W and 200 W are shown.	80
4.12	Thickness (nm) versus time (min) of the etching of as deposited TiSiON with CF ₄ 15 sccm, at 10 mTorr. Both powers of 100 W and 200 W are shown.	81
4.13	Thickness (nm) versus time (min) of the etching of as deposited TiSiON with Cl ₂ plasma. Different parameters were used for each point. First step: 100 W, 10 sccm, 20 mTorr. Second step: 100 W, 10 sccm, 10 mTorr. Third step: 150 W, 20 sccm, 20 mTorr.	82
4.14	Fabrication steps for patterning nanostructures using a metal as hard mask. (a) Spin of e-beam positive resist. (b) Exposure with electron beam lithography. (c) Patterned resist after development. (d) Evaporation of the hard mask. (e) Resist lift-off. (f) Reactive ion etching of TiSiON. (g) Hard mask removal by wet etching.	85
4.15	SEM image taken after 30-nm thick aluminum evaporation. Structure exposed with 3500 μC/cm ² dose. Gap dimension from design: 0 nm.	87
4.16	SEM image taken after CF ₄ RIE at 200 W. The plasma has widened the gap. Some nanometers of gold cover the sample. Gap dimension from design: 0 nm. Dose of the exposure: 3500 μC/cm ²	88
4.17	SEM image showing 200-nm wide lines after CF ₄ RIE at 200 W. The walls have a taper angle of 70-75°. Some nanometers of gold cover the sample. Dose of the exposure: 3500 μC/cm ²	88

4.18	SEM image taken after CF ₄ /O ₂ RIE at 100 W, using aluminum as hard mask. The gap is narrow and the profile are not rounded. Some nanometers of gold cover the sample. Gap dimension from design: 0 nm. Dose of the exposure: 3500 μC/cm ²	89
4.19	SEM image showing 50-nm wide lines after CF ₄ /O ₂ RIE at 100 W, using aluminum as hard mask. Some nanometers of gold cover the sample. Dose of the exposure: 5000 μC/cm ²	89
4.20	SEM image taken before etching. Gap dimension from design: 0 nm. Dose of the exposure: 3500 μC/cm ²	91
4.21	SEM image after CF ₄ /O ₂ RIE at 100 W, using aluminum as hard mask. Gap dimension from design: 0 nm. Dose of the exposure: 3500 μC/cm ²	91
4.22	SEM image taken before etching. Gap dimension from design: 0 nm. Dose of the exposure: 3500 μC/cm ²	92
4.23	SEM image after CF ₄ /O ₂ RIE at 200 W, using aluminum as hard mask. Gap dimension from design: 0 nm. Dose of the exposure: 3500 μC/cm ²	92
4.24	SEM image showing a bow-tie structure after 2 minutes of MF CD-26 soak.	94
4.25	SEM image showing TiSiON after 1 minute of Al etch type A soak.	94
4.26	Comparison of a structure etched with CF ₄ and CF ₄ /O ₂ plasmas, using molybdenum as hard mask. The structures were fabricated on the same sample and went through the same processes, except for the dry etching. The correlation is very high.	95

4.27	Comparison of etched lines with CF_4 and CF_4/O_2 plasmas, using molybdenum as hard mask. The lines were fabricated on the same sample and went through the same processes, except for the dry etching. The correlation is very high.	96
4.28	Bowties etched with CF_4 and CF_4/O_2 plasmas, using titanium as hard mask.	98
4.29	Bowties and lines etched with CF_4 plasma at 200 W, using chromium as hard mask.	99
4.30	Bowties etched with CF_4/O_2 plasma at both 100 W and 200 W, using chromium as hard mask.	100
4.31	SEM image showing bow-ties fabricated with a chromium hard mask after 3 minutes of Cr-7 etch soak. The chromium thin layer was not removed.	101
4.32	SEM image showing bow-ties fabricated with 15-nm thick aluminum and 15-nm thick chromium bi-layer hard mask after CF_4/O_2 RIE at 100 W. The overetched thickness into the silicon substrate is well-defined.	102
4.33	Structures after a 3 minutes long wet etching in pure TMAH. The lift-off worked with some structures, while the mask still has to lift-off on others.	103
4.34	SEM image of a bow-tie structure with wires after 15 minutes soak in TMAH in an ultrasonic bath.	104
4.35	Process flow for pads fabrication. (a) Sample after hard mask removal from the previous step. (b) Spin a resist bi-layer: PMGI SF-9 and S1813. (c) Exposure with DWL and develop. (d) Evaporation of the pads: 50 nm Ti and 250 nm gold. (e) Resist bi-layer lift-off.	105

4.36	Final layout. First zoom in on two groups of arrays with two different doses. Second zoom in on a single array.	107
4.37	Array of bow-ties fabricated on silicon with TiSiON as deposited. . .	108
5.1	Experimental setup for electrical testing.	111
5.2	Experimental setup for optical testing.	112
5.3	Source's spectral power density used for optical testing.	113
5.4	SEM image of TiSiON17 set 6C.	114
5.5	Field emitted current of TiSiON17 set 6C. Voltage sweep from -10 V up to 10 V.	115
5.6	Pzt scan maps of both voltage amplitude and phase delay on TiSiON17 set 6C with a bias voltage of -2 V. Some regions are more active than others.	117
5.7	Photocurrent and phase delay of TiSiON17 set 6C. Voltage sweep from -5 V up to 5 V.	118
5.8	Potential of the structures when a bias voltage is applied. An opposite bias flips the current sign, which is equivalent to a phase shift of π . (a) Positive applied bias voltage. (b) Negative applied bias voltage. .	119
5.9	Measured extinction spectrum of TiSiON17 set 6C. No peak is present in the near infrared, we are probably working in the multiphoton emission because of a too small field enhancement factor of the structures.	120
5.10	Electrical current in time to electromigrate the connected bow-ties of the set 6B. Bias voltage set to 10 V. The steps in the current derive from openings in the connections.	122
5.11	Electrical current of the set 6B. Bias voltage sweep from -10 V up to 10 V.	123

5.12	Linear and logarithmic plots of the photocurrent of set 6B after electromigration. Voltage sweep from -5 V up to 5V.	124
5.13	Phase delay of the set 6B for different laser power. Bias voltage sweep from -5 V up to 5 V.	125
5.14	SEM image of the set 6C of bow-ties after electrical and optical testing. The gaps shrank and some damages are present on the surface.	126
5.15	SEM image of the set 6B of bow-ties after electrical and optical testing. The gaps shrank.	127
5.16	SEM image of the leads of the set 6B of bow-ties after electromigration. Many leads got cut and the wires that were connected to them are wider than the others.	128
5.17	SEM image of TiSiON19 set 7C before testing.	129
5.18	I-V curve of TiSiON19 set 7C after electromigration.	130
5.19	Excited photocurrent and phase delay of TiSiON19 set 7C after electromigration. Voltage sweep from -5 V up to 5V.	131
5.20	SEM image of TiSiON19 set 7C after testing. No damage is present in this area and we can see how the gaps shrank down to dimensions smaller than the SEM resolution.	132
5.21	SEM images showing the damages the electrical and optical testing caused to TiSiON19 set 7C.	133

List of Tables

2.1	Optical parameters for TiSiON film as deposited.	18
2.2	Fixed dimensions used during the FEM simulation of bow-ties.	20
2.3	Real and imaginary parts of the permittivity of different materials at 1200 nm.	26
2.4	Optical parameters for annealed TiSiON film.	41
4.1	Edge types and energies where the edges of each material are located.	73
4.2	Relative concentrations of the elements in six different spatial points.	76
4.3	Etchants and recipes to etch TiN with relative etch rates.	77
4.4	Etchants used in wet etching procedures and etch rate on TiSiON. . .	83
4.5	Etching parameters used for CF ₄ /O ₂ and CF ₄ for hard masks investi- gation.	84
5.1	Nominal and obtained dimensions of the TiSiON17 set 6C of bow-ties before testing.	113
5.2	Nominal and obtained dimensions of the TiSiON17 set 6B of bow-ties before testing.	121

Chapter 1

Introduction

Nanoparticles exhibiting localized surface plasmon resonances (LSPR) already have several applications: surface-enhanced Raman spectroscopy (SERS) [1], high-resolution imaging [2], metamaterials [3], sensors [4, 5], optoelectronics [6] and nanolithography [7]. At high intensities, light-matter interactions are controlled by the electric field of optical waveforms. At the surfaces of nanostructures, optical-field photoemission can be driven at frequencies above 100 THz by enhanced electric fields [8, 9, 10, 11, 12, 13]. The optical-field emitted photocurrent is also characterized by the sensitivity to the phase delay between the carrier wave and the intensity envelope of an ultrafast pulse, i.e. the carrier envelop phase (CEP) [8, 9, 10, 14]. Optical-field-controlled photoemission and CEP-sensitivity have also been demonstrated with plasmonic gold nanoantennas [8, 15]. Gold nanorod arrays are often damaged by intense optical radiation [16]. Refractory plasmonic materials have gained attention in the last years [32] as a possible solution due to their high bulk melting points and, thus, their robustness under illumination. Titanium nitride is a CMOS-compatible refractory material that represents a good alternative for plasmonics and metamaterials applications [17, 18].

Furthermore, complete tunability of the optical dispersion of titanium nitride has been demonstrated by altering its composition with added Si and/or O₂ impurities [19].

In the next sections, we will present the physical principle of field electron emission. We will also show how light-matter interactions are described in presence of localized surface plasmon resonances, which can exploit light to realize optical field detectors (i.e. for CEP detection or enhanced photodetectors). We will introduce titanium silicon oxynitride, the new plasmonic material this thesis project has been focusing on. Finally, the motivation of this thesis and its outline will be presented.

1.1 Field Electron Emission

The electron emission in strong electric fields was studied for the first time in the 1920s by R. H. Fowler and L. Nordheim [20]. Schottky had already started the study of the emission of electrons between two electrodes, but the emission mechanism was completely different. The Fowler-Nordheim tunnelling mechanism is basically based on a tunnel effect that happens when the energy level of the vacuum gap between two electrodes is lowered and the tunnelling distance is thus reduced. If we consider two electrodes with the same band structure as shown in Figure 1.1(a), we will have a square barrier and a certain tunnelling distance between source and drain. As soon as we apply a bias (or we perturb the system with a radiation), the band structure changes. Thus, the shape of the barrier and the tunnelling distance change as well, leading to a flow of electrons from the source to the drain as shown in Figure 1.1(b). These electrons have flown passing through the barrier, and not above it.

The phenomenon is described by the F-N equation [21]:

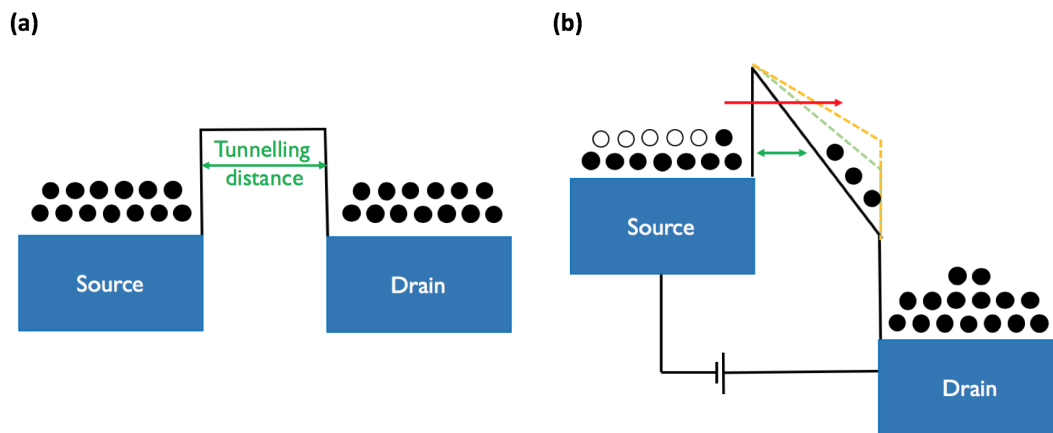


Figure 1.1: Schematics of Fowler-Nordheim emission mechanism. (a) Non-biased source and drain electrodes. (b) A current is flowing from the source to the drain due to a bias voltage, which reduces the tunnelling distance.

$$J = \frac{e^3 F^2}{8\pi h \phi t(y)} \exp \left[- \frac{8\pi (2m)^{\frac{1}{2}} \phi^{\frac{3}{2}}}{3heF} v(y) \right] \quad (1.1)$$

where J is the current density, e is the electron charge, F is the electric field at the negatively biased electrode, h is Planck's constant, ϕ is the work function at the negative electrode, $t(y)$ and $v(y)$ are approximated constants, with y parametric function of F and ϕ . We can notice that the electric field F and the work function ϕ can be exploited to enhance the tunnelling current. Unfortunately, using low-work-function materials is quite difficult, because of their low reliability in large scale processes. Therefore, we will try to increase the tunnelling current by enhancing the electric field. It is possible to re-write the tunnelling current from Eq. (1.1) to the following formula [21]:

$$I = aV^2 \exp \left(- \frac{b}{V} \right) \quad (1.2)$$

where a and b are given by:

$$\begin{aligned} a &= \frac{1.56 \times 10^{-6} \alpha \beta^2}{1.1 \phi} \exp\left(\frac{10.4}{\phi^{\frac{1}{2}}}\right) \\ b &= \frac{6.44 \times 10^7 \phi^{\frac{3}{2}}}{\beta} \end{aligned} \quad (1.3)$$

where α is the emitting area and β is the enhancement factor. For high voltages, the current has a quadratic behavior, while it is exponential when the applied voltages are low. The best way to enhance the current of Eq. (1.2) is to increase the field-enhancement factor β . The field enhancement factor is dependent on the geometry of the device and, if we consider an emitter with a tip shape, the field enhancement can be modelled as follows when a DC voltage is applied:

$$\beta = \frac{2l/r}{\ln(l) - 2} \cdot \frac{1}{d} \quad (1.4)$$

where l is the length of the emitter, r is the radius of curvature (ROC) of the tip, and d is the gap between emitter and collector. Thus, by playing with the geometry, we can enhance the electric field at the tip and increase the tunnelling current. Optical field enhancement factors are more complex. However, smaller emitter radii still lead to larger β -values, and plasmonic resonances can be used to excite charge oscillations that lead to much larger field enhancements than possible using non-plasmonic materials.

1.2 Light-matter interactions and Surface Plasmon Resonances

If we want to realize an optical detector, we can use a laser to bend the potential barrier of the device and excite the field electron emission. The main limiting factor of nonlinear photoemission is given by the damage induced by the light on solid materials [22]. Limiting the laser-matter interaction time by using ultrashort laser pulses increases the damage threshold. Furthermore, as we have seen in Section 1.1, at sharp metal tips, field enhancement occurs, making it possible to reach high local intensities limiting the damages over the surface. But we can do better.

When a material interacts with light, the electrons of the surface are affected by its electric field. These field-controlled interactions were first studied using gas excitations. Materials that possess a negative real and small positive imaginary permittivity are capable of supporting surface plasmon resonances (SPR) [23]. This resonance is a coherent oscillation of the surface conduction electrons excited by electromagnetic radiation. We need to distinguish between propagating surface plasmons (also called surface plasmon polaritons) and localized surface plasmons. Surface plasmon polaritons are surface electromagnetic waves that propagate in the x- and y-directions along the material-dielectric interface and decay evanescently along the z-direction both within the thin film and in the outside dielectric medium (see Figure 1.2(a)). The propagation goes on for tens or hundreds of micrometers [24, 25, 26]. For a localized surface plasmon, the light interacts with particles that are much smaller than the incident wavelength. Thus, the plasmon starts oscillating locally around the nanoparticle with a frequency that is called localized surface plasmon resonance (see Figure 1.2(b)) [27].

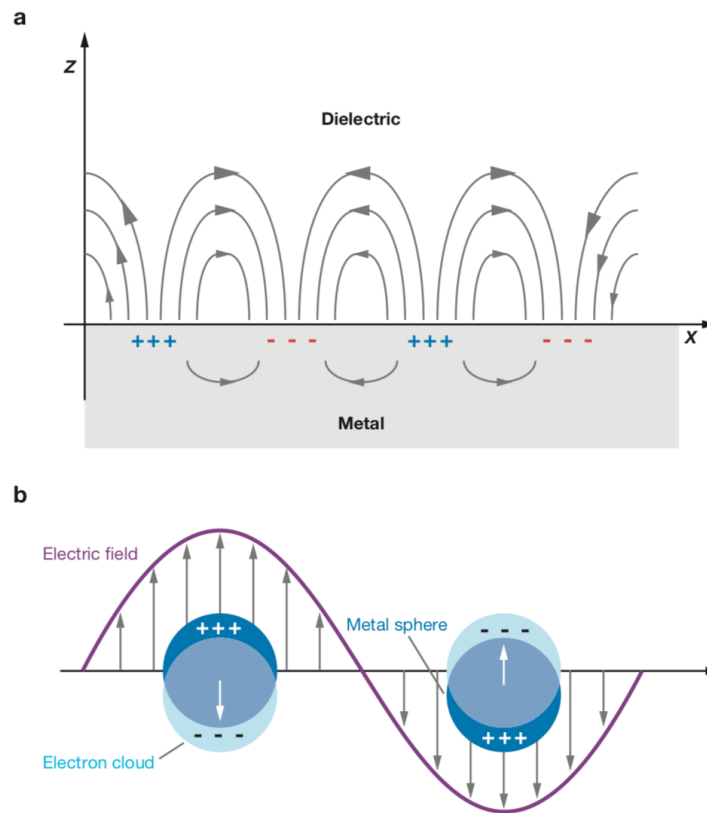


Figure 1.2: Schematics of both surface plasmon polaritons and localized surface plasmons. (a) Surface plasmon polaritons. The propagation is along the x - and y -directions, while the plasmon decays evanescently along the z -direction. (b) Localized surface plasmons for a sphere. The electron cloud of the metal sphere oscillates along the electric field direction. The plasmon does not propagate along the surface. [23]

A plasmonic nanoantenna is a metallic nanoparticle that allows surface plasmon resonances due to the nature of its refractive index. We can use a plasmonic nanoantenna as an electron emitter. If we combine the geometry of the emitter and the plasmonic nature of the material, the emission can be further enhanced thanks to the energy of the oscillating electrons under the control of an exciting field. The resonance frequency of the surface plasmon can be found by studying the transmitted power spectral density of the light incident on the nanoantenna. Taking the ratio of the spectrum of the radiation passing through the plasmonic nanoantenna to that of the incident radiation, we can define the transmission spectrum. At the plasmon resonance, the transmission spectrum will show a dip, due to the power absorbed by the plasmon. At other frequencies, since the plasmon has not been activated, the power detected by the spectrum analyzer will be the same as when the laser doesn't pass through the sample. In order to make this kind of measurement, we need the substrate to be transparent for the radiation we use.

1.2.1 Photoemission regimes

Depending on the laser parameters and material properties, we can define different regimes of photoemission. The Keldysh theory describes these regimes [28]. This theory was originally formulated for the ionization of a single atom, but Bunkin and Fedorov extended it to the photoemission from a metal surface [29].

Keldysh formulated a characteristic parameter γ that separates two limiting regimes: the multiphoton regime ($\gamma \gg 1$) and the tunnelling regime ($\gamma \ll 1$) [31]. The tunnelling regime is called optical field emission for metals. For a metal with work function ϕ , the Keldysh parameter γ is given by [31]:

$$\gamma = \sqrt{\frac{\phi}{2U_p}} \quad (1.5)$$

where U_p is the ponderomotive energy and is defined as:

$$U_p = \frac{q^2 E_0^2}{4m\omega^2} \quad (1.6)$$

and corresponds to the mean kinetic energy of a free electron oscillating in a monochromatic light field of frequency ω and peak electric field E_0 . The ponderomotive energy scales linearly with the intensity. q is the electron charge, m is the mass of the electron. If we want to get into the tunnelling regime, we can either increase the intensity or decreasing the carrier frequency. Nevertheless, there are validity limits to the Keldysh tunnelling theories. For example, if we keep increasing the intensity, the tunnelling barrier gets suppressed [30], so long as we do not first damage the material.

Photofield emission happens when an electron acquires a multiple of the photon energy due to the incident radiation and then tunnels through the barrier at a higher energy than the Fermi level (see Figure 1.3(a)). If we are in the multiphoton regime, a minimum number n of energy quanta $\hbar\omega$ is required to overcome the work function of the metal. In this regime, the photocurrent scales with the power law I^n (see Figure 1.3(b)). If we increase the laser intensity, more than the minimum required number of photons will be absorbed, leading to the so-called above-threshold photoemission (ATP) (see Figure 1.3(c)). Strong-field effects mark the transition to a tunnelling regime and optical field emission. In this regime, the ponderomotive energy is not negligibly small due to the very high field intensity. The Keldysh parameter is much smaller than 1. The laser field is so strong that the barrier becomes

penetrable and electrons tunnel from states in the proximity of the Fermi level. (see Figure 1.3(d)) The evidence for optical field emission is marked by a deviation from the multiphoton intensity scaling of the photocurrent.

1.3 TiSiON as plasmonic nanostructure

Noble metals like Au and Ag are good candidates for plasmonic applications thanks to their large negative real permittivities. Nevertheless, their actual application is confined, due to their low melting points, easy degradation in harsh environments, and lack of CMOS-compatibility. Furthermore, noble metals exhibit a narrow bandwidth and high losses depending on the optical region of application.

Refractory materials are defined as those with a high melting point and chemical stability at temperatures above 2000 °C [32]. This kind of materials could solve some of the main issues noble metals have for applications in harsh environments. Metals have been studied as refractories, but their optical properties are not suitable for plasmonic applications in the visible to near-infrared spectral regions.

Figure 1.4 shows a comparison between many materials, pointing out their bulk melting point, their crossover wavelength in the real part of the permittivity and the value of their imaginary part of the permittivity at 1000 nm. The bulk melting point is important if we want to be able to use these materials in harsh environments and prevent their damage. The crossover wavelength of the real part of the dispersion plays a key role defining the optical range over which we can use our devices. The value of the imaginary part of the dispersion represents losses in the material: if the losses are too high, the surface plasmon resonance will get damped, preventing a high field enhancement. Tungsten and metallic alloys have high melting points (thus, they are refractory), but also show a relatively high imaginary permittivity.

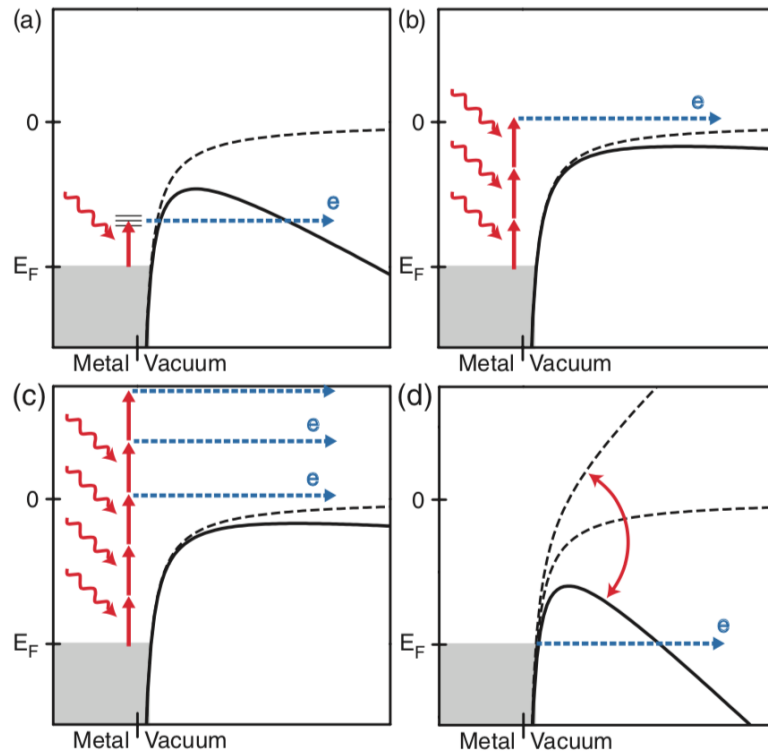


Figure 1.3: Schematics of the four different photoemission regimes. (a) Photofield emission. (b) Multiphoton photoemission. (c) Above-threshold photoemission. (d) Tunnelling photoemission (or optical field emission). [32]

Gold and silver have a low melting point, but their imaginary permittivity is very low, which is the reason why they are good plasmonic materials. Aluminum has a low melting point like Au and Ag, but shows high losses instead.

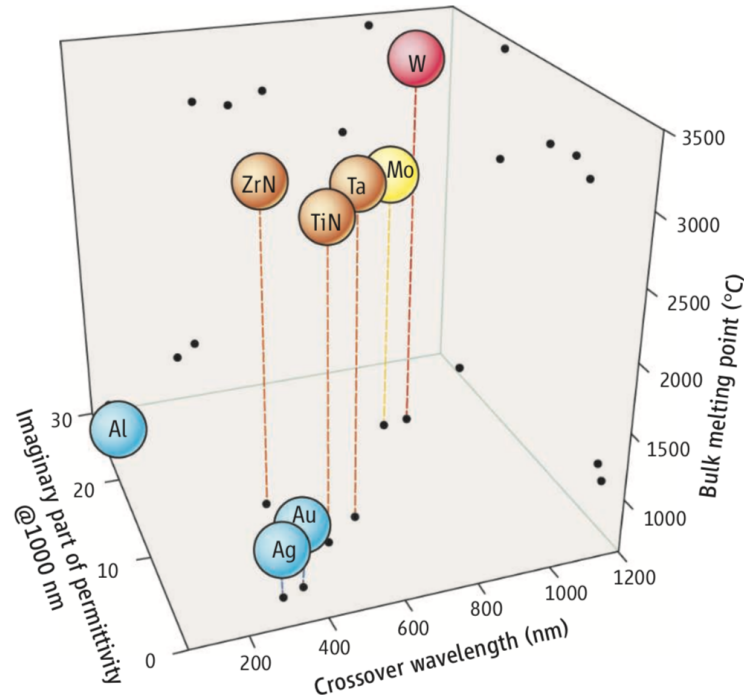


Figure 1.4: Comparison between different noble metals and refractory materials. Parameters in the axes: bulk melting point, crossover wavelength and imaginary part of the permittivity at 1000 nm. [31]

Metallic alloys, intermetallics and metallic compounds represent a good alternative for plasmonic materials [33]. They show large free electron densities, which is translated into a negative real permittivity, and can be very resistant to high temperatures and harsh environments. Most importantly, there is a way to tune their optical properties by adding two or more elements to the noble metals as dopants. The proportion of the alloyed elements will lead to different values of the real and

imaginary parts of the permittivity, which means different optical properties.

Transition-metal nitrides have also been studied as alternative plasmonic materials. TiN has emerged as a good candidate in the visible and NIR spectral range, due to its reduced optical losses compared to the conventional noble metals [34]. By doping TiN with both silicon and oxygen, the dispersion of the film can be modulated, leading to good plasmonic properties to design metasurfaces, i.e. nanoantennas for optical applications. A double-plasmon broadband response can be obtained by engineered titanium silicon oxynitride. The optical properties of this metamaterial have been studied by modifying the concentration of Si and O₂ dopants in the titanium nitride layer and by analyzing how the post-deposition annealing can affect the material dispersion [19]. Furthermore, TiSiON shows a broad bandwidth, which cannot be achieved using noble metals like Au and Ag due to their large negative real permittivity.

1.4 Master's Thesis project

This master's thesis reports the work carried out in the Research Laboratory of Electronics (RLE) at Massachusetts Institute of Technology (MIT), in the Quantum Nanostructures and Nanotechnologies (QNN) group, under the supervision of Prof. Karl K. Berggren and Phillip D. Keathley, starting from March 2019 until August 2019.

1.4.1 Motivation

This thesis project has mainly dealt with the development of a fabrication process to etch a new plasmonic material: titanium silicon oxynitride. It has allowed the

fabrication of plasmonic nanoantennas and their electrical and optical testing. These nanoantennas have also been simulated using a finite element method simulator called MEEP.

The project has originated from a collaboration with Prof. L. Dal Negro and W. Britton from the Nanogroup at Boston University (BU). They had already worked on the material and its sputtering techniques, pointing out the strengths in its optical parameters [19] and the differences between the film as deposited or annealed. Our goal has been to fabricate nanostructures for vacuum electronics, optical field detection and optoelectronics applications where traditional plasmonic materials have proved limiting due to their low damage threshold.

The obtained results have allowed the group to start the testing and the optimization of the sputtering of the film and design of the plasmonic nanoantennas. They will possibly allow an advance of field emission based devices and state-of-the-art optical field detectors.

1.4.2 Thesis's structure

The structure of this thesis is here reported.

In Chapter 2 we will first simulate the plasmonic nanoantennas, comparing them to others fabricated both with a non-plasmonic material like tungsten and with a state-of-the-art plasmonic material like gold. We will then carry out a study over the different geometric parameters we can change in the design of the nanoantennas.

In Chapter 3 we will present the main fabrication techniques we used during the fabrication of the plasmonic nanoantennas, like Electron Beam Lithography, Reactive Ion Etching, Direct Writing Laser for photolithography and Focused Ion Beam. We will also talk about the techniques we used to characterize the film and

the structures we fabricated. Ellipsometry was used to characterize the film thickness during the etch tests we carried out. Transmission Electron Microscopy was used instead to image the grain of the material and to perform an Electron Energy Loss Spectroscopy to characterize the chemical composition of the film.

In Chapter 4 we will show the development of the fabrication process for patterning TiSiON. All the etchants comparison and the hard masks study will be shown, pointing out the results we obtained from each different etching recipe, leading to the successful fabrication of the final devices.

In Chapter 5 we will see the results of both electrical and optical testings we performed on devices fabricated on different films (as deposited and after annealing).

Chapter 2

Bow-ties FEM simulations

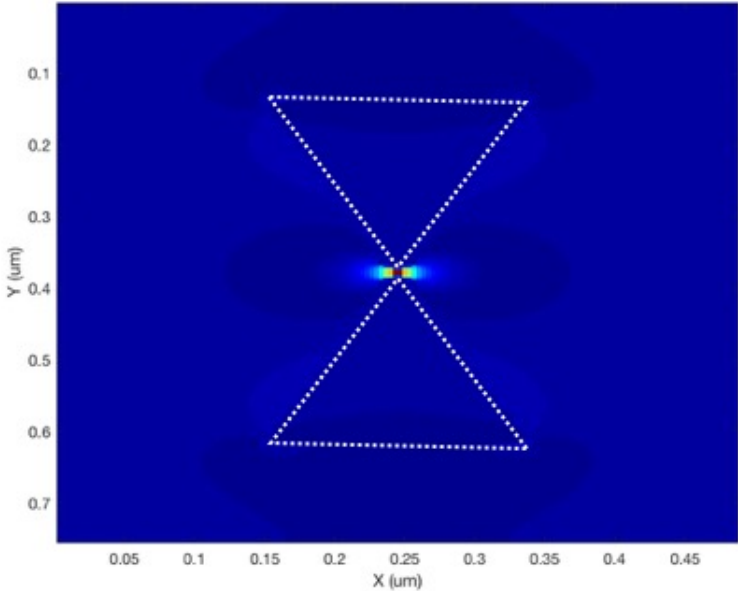
We simulated bow-tie nanoantennas using a finite element method simulator called MEEP, an open-source software package for electromagnetics simulation via the finite-difference time-domain (FDTD) method. It is a numerical analysis technique, which can cover a wide frequency range and can treat non-linear material properties using a time-domain method. A time-domain electromagnetic simulation performs numerical experiments over time within a finite computational volume by numerically solving Maxwell's equations. These kinds of simulations provide the study of the transmittance and reflectance spectra, of resonant modes and frequencies, and of the field profile of the system in response to an incident short pulse. Meep defines a cell space where the structures are, fixing periodic boundary conditions at the boundaries of the cell. We put three monitors inside the cell, in order to analyze the electromagnetic behavior of the structure on three different surfaces. A first monitor is put between the structure and the short pulse source, a second one is put just on the surface of the structure, and the third one is put below the structure. This way we are able to evaluate both the reflected, transmitted and absorbed radiations.

The monitor on the surface allowed us to evaluate the electromagnetic behavior of the metamaterial, relating the incident field and the excited field at the tip in time. MEEP always performs two simulations: a first one without the structures in order to evaluate the background, and a second one with the structures. We make the difference between the two simulations and the results are finally evaluated. A qualitative representation of the field profiles of the simulated structures (with and without connectors) are shown in Figure 2.1.

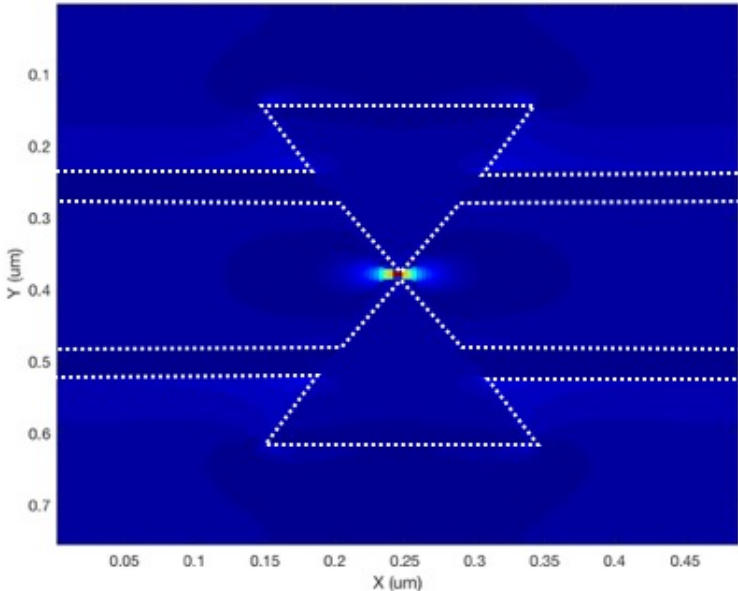
In the following sections we will show the results of the MEEP simulations on plasmonic nanoantennas made of TiSiON. The film as deposited will be analyzed first, while the influence of the annealing on the film will be shown later. For both cases, we will start by showing the real and imaginary parts of the permittivity extracted from the Drude-Lorentz model. During the study of the film as deposited, a first comparison with gold and other materials (like tungsten, titanium and aluminum) has been carried out, pointing out the advantages and drawbacks of using TiSiON as metamaterial. A thorough study on the geometry has been performed both on bow-ties with and without connector bars. As last step, the difference with the TiSiON film after annealing will be shown.

2.1 TiSiON film as deposited

We start analyzing the FEM simulations from the TiSiON film as deposited. The optical properties of a metal in the near infrared can be described by means of the Drude model [35]. The inability of the model to calculate the relative permittivity of a material over a wide frequency range has also been demonstrated with gold [36]. The Drude-Lorentz model can overcome the limits of the previous model by adding some Lorentzian terms to describe the oscillators represented by the electrons around



(a) Electric field profile without connector bars.



(b) Electric field profile with connector bars.

Figure 2.1: Electric field profiles of a pair of bow-ties with and without connector bars.

their nuclei. We use the following formula for the dispersion [37]:

$$\tilde{\epsilon}(h\nu) \equiv \epsilon_1 + \epsilon_2 = \epsilon_{1\infty} + \sum_k \frac{Am_k}{En_k^2 - (h\nu)^2 - iBr_k h\nu} \quad (2.1)$$

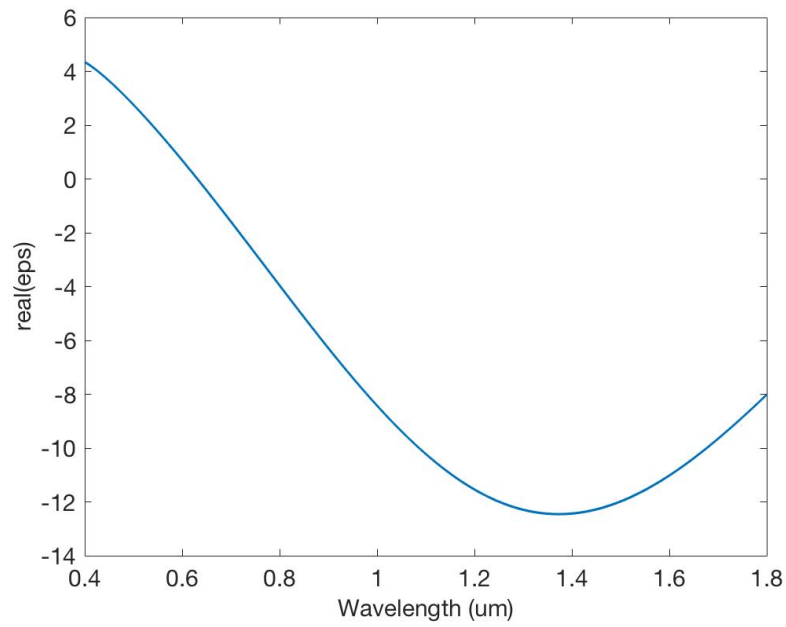
where $h\nu$, E_k and B_k are in units of eV , while A_k is in units of eV^2 . Table 2.1 shows the Drude-Lorentz coefficients that have been used to extract the real and imaginary permittivities of TiSiON as deposited. The Lorentz terms describe interband transitions with a strength of Am_i , a broadening of Br_i and an energy of En_i ($i = 1, 2, 4$). Drude term is represented by a Lorentz Oscillator where E_k is equal to 0 (i.e. En_3). Thus, Am_3 and Br_3 represent the Drude term.

e1(inf)	2.5459 ± 0.724
Br1	3.2286 ± 0.335
Br2	0.919 ± 0.0382
Br3	0.54652 ± 0.276
Br4	18.368 ± 74
Am1	100.36 ± 28.3
Am2	21.396 ± 5.8
Am3	13.856 ± 6.11
Am4	75.721 ± 420
En1	4.8153 ± 0.141
En2	0.70543 ± 0.0154
En4	6.3328 ± 15.1

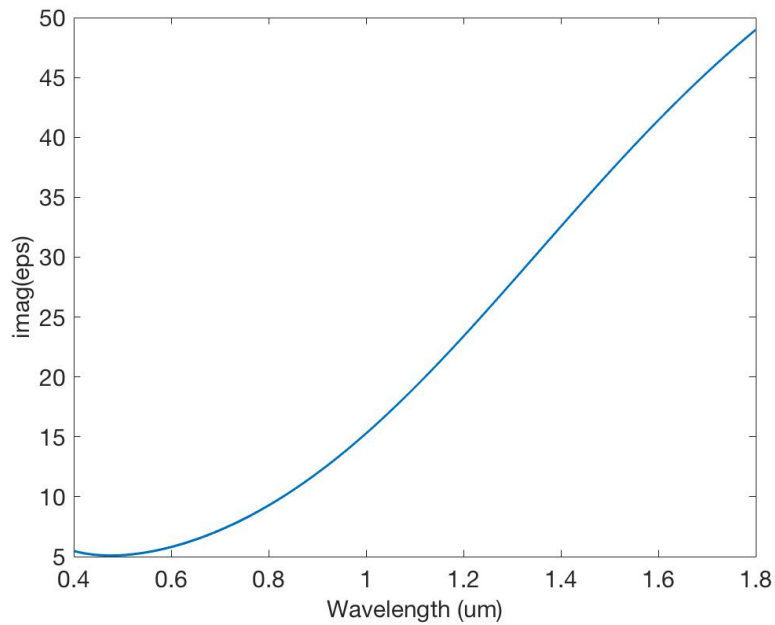
Table 2.1: Optical parameters for TiSiON film as deposited.

The real and imaginary parts of the permittivity of the film are shown in Figure 2.2. As we can see, the real part shows a single crossover to negative ranging from $0.4 \mu\text{m}$ and $1.8 \mu\text{m}$ and the losses increase with the wavelength.

We are going to consider the difference between gold and TiSiON. Then we will present a study on the different geometric parameters that can affect the behavior of



(a) Real part of the permittivity.



(b) Imaginary part of the permittivity.

Figure 2.2: Permittivity components for TiSiON film as deposited.

the nanoantennas. For all these simulations, we used bow-ties nanostructures with the dimensions reported in Table 2.2. It's important to note that we considered a 50-nm deep overetch in the substrate in the TiSiON bow-ties case. We don't make the same choice for tungsten and gold, since the two fabrication processes are intrinsically different: with TiSiON we need to etch, while with the other materials we would usually use deposition and lift-off procedures. Titanium nitride needs to get etched as well, but the substrate wouldn't get etched by using chlorine plasma, so we do not consider any underetch for titanium nitride.

Altitude	250 nm
Base/altitude ratio	0.75
Metal thickness	50 nm
Etched oxide thickness	50 nm
Radius of curvature	10 nm
Gap	10 nm

Table 2.2: Fixed dimensions used during the FEM simulation of bow-ties.

2.1.1 Comparison with Au nanostructures

The first thing we need to do is to justify why TiSiON is a good candidate as a metamaterial for optical field detection compared to the materials that are already used in the same applications. We made this comparison using gold as investigated noble metal. At 1200 nm, gold has a large negative real part of the permittivity ($\epsilon_1 = -69$) and a very low imaginary part ($\epsilon_2 = 4.7$). Because of the nature of its refractive index, gold is a good plasmonic material.

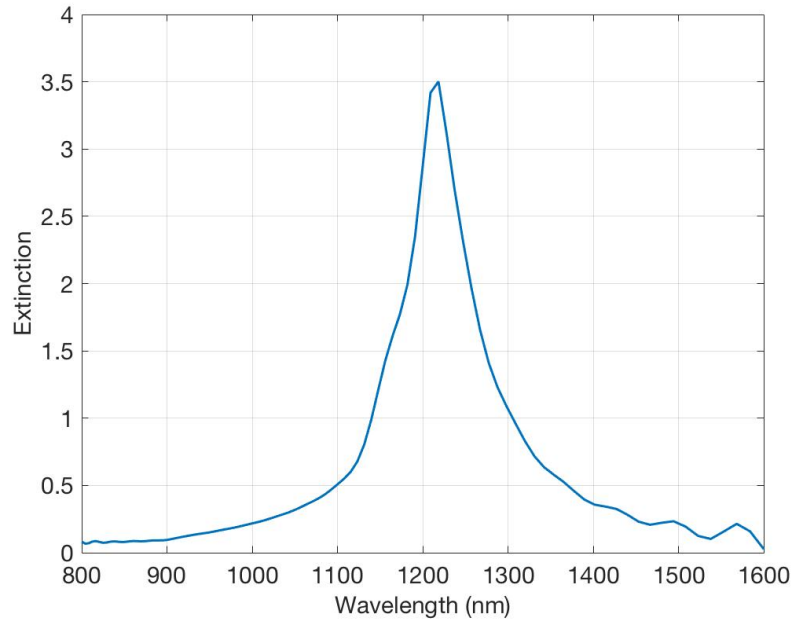
First of all, we define the extinction spectrum of a structure as follows:

$$E = -\log T \tag{2.2}$$

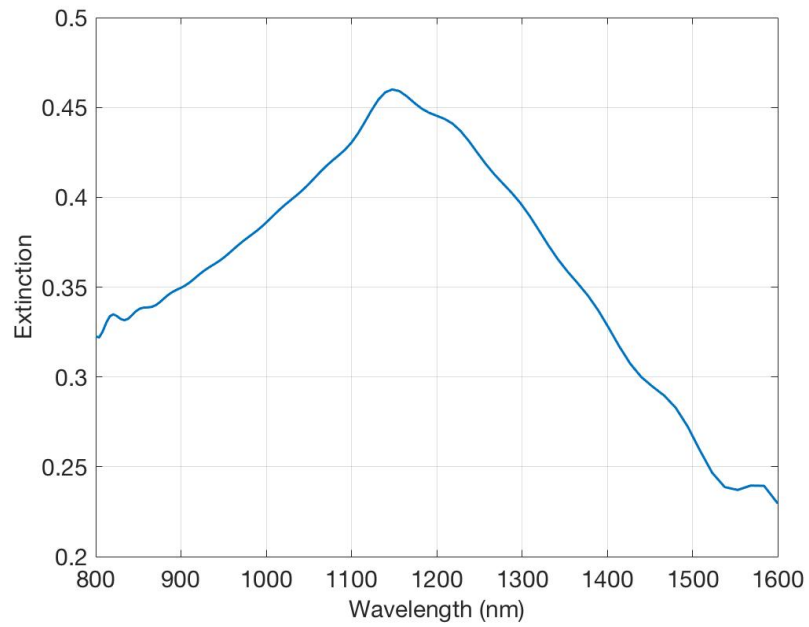
where T is the transmission spectrum. Like all the other noble metals, gold has a very narrow bandwidth, but the extinction spectrum reaches much higher peaks than titanium silicon oxynitride. The two extinction spectra, both for gold and TiSiON, are shown in Figure 2.3.

As we can deduce from the extinction spectra, since the two structures have the same dimensions, the bow-ties made of gold absorb much more radiation than the TiSiON ones. In terms of transfer function, it is translated into very large values of magnitude for gold, even though with a very narrow bandwidth. TiSiON shows a low value of magnitude but a much wider bandwidth. The transfer functions of the two materials are compared in Figure 2.4. While gold nanoantennas work better at a defined central frequency, the TiSiON nanoantennas behave like a low-pass filter, cutting on the low wavelengths, i.e. the high frequencies. The phase shift turns out to be wider for gold, but most of the shift happens in a very confined region of wavelengths. The phase shift for TiSiON is more gradual and smooth. It will lead to an excited field much more similar to the incident one. In fact, if a non-monochromatic radiation impinges on gold nanoantennas, the different wavelengths will be subject to different and large phase delays, which imply a loss about the received information. The phase delay is much more contained in the case of TiSiON.

The field enhancement is the square root of the magnitude of the transfer function. In Figure 2.5 we plot the field enhancement for the two materials. It is important to notice that the simulation were carried out just considering structures made of gold and titanium silicon oxynitride. For the fabrication of bow-ties made of gold, it would be a process based on lift-off, and not on the etching of the structures. To ensure the gold's adhesion to the substrate, we need to add a titanium adhesion layer of few nanometers. This layer would slightly reduce the field enhancement of the structures [16]. Thus, a field enhancement of about 150 would be impossible to

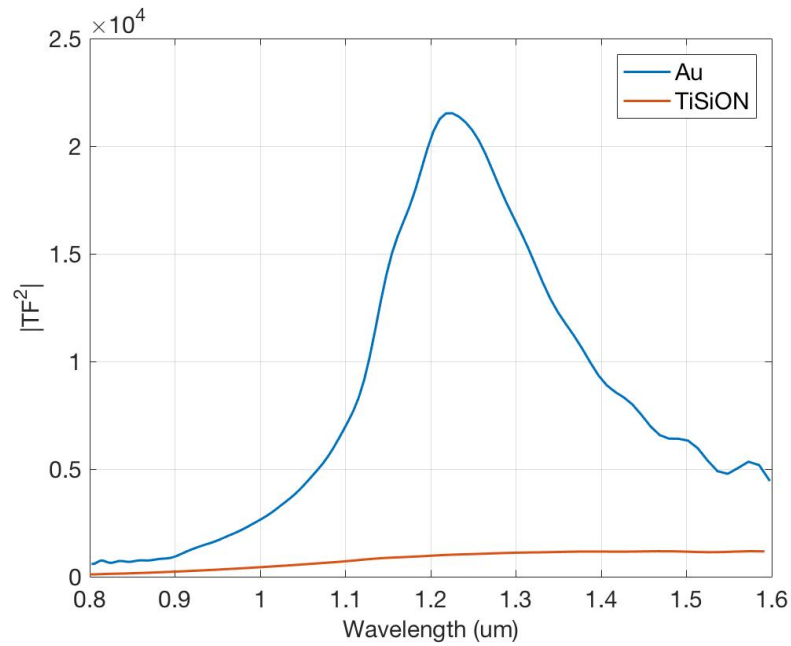


(a) Extinction spectrum of gold.

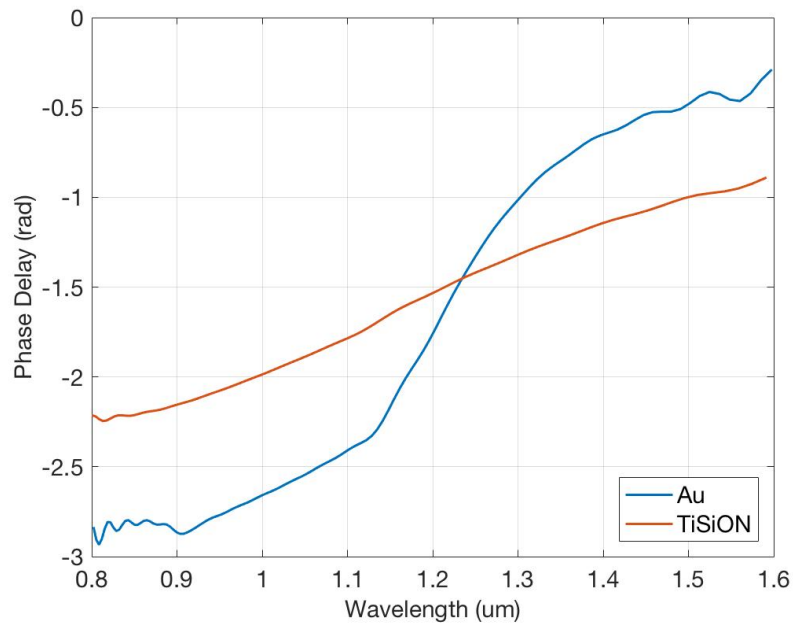


(b) Extinction spectrum of TiSiON.

Figure 2.3: Extinction spectra of both gold and TiSiON films. Gold has a very narrow peak, but it is an order of magnitude larger than the TiSiON one.



(a) Magnitude of the transfer functions of both gold and TiSiON.



(b) Phase delay of the transfer functions of both gold and TiSiON.

Figure 2.4: Comparison of Au and TiSiON transfer functions.

reach even with gold.

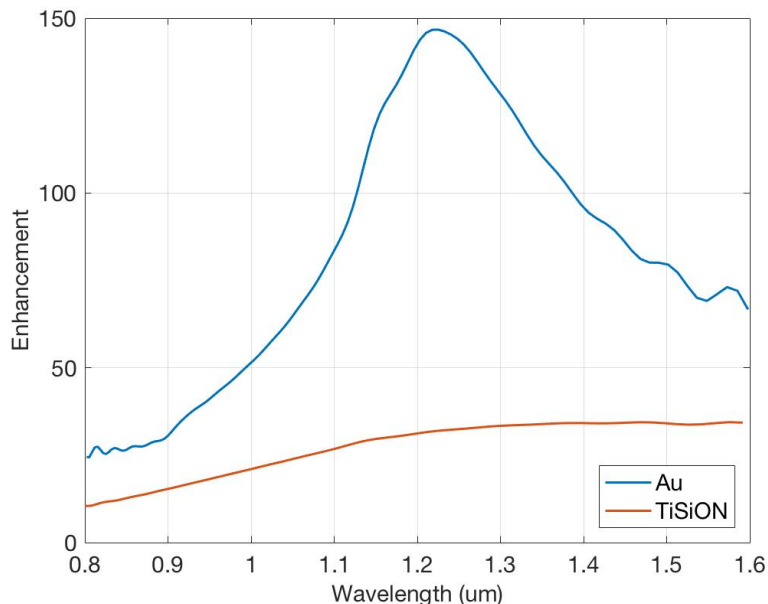
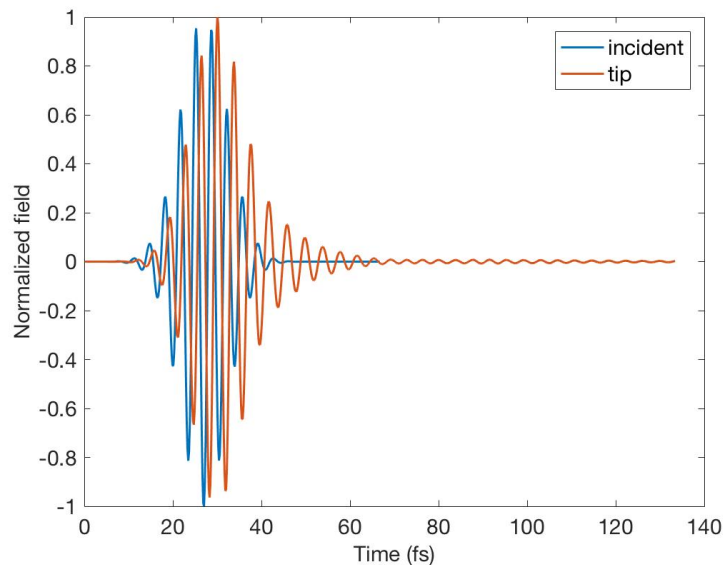
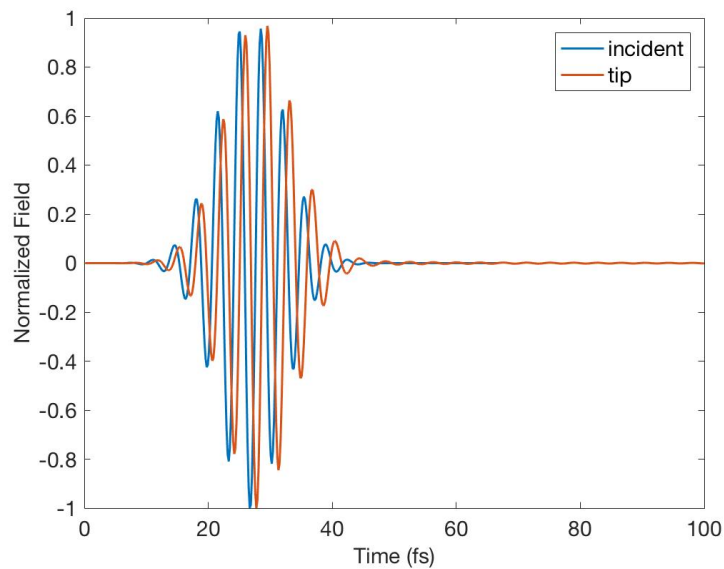


Figure 2.5: Field enhancement at the tip of both gold and TiSiON bow-ties structures.

If we want to use these bow-tie structures for optical field detection, they must be good enough to detect an incident field and to reproduce the incoming information into an electrical quantity that we can measure. We can measure the voltage between the two structures, or the current flowing between them. We need this voltage or current to be the most similar to the incident radiation profile. From Figure 2.6 we can understand the greatest strength of TiSiON: the field at the tip basically has the same shape of the incident field. For gold, the incoming information has been altered. Furthermore, the resonance in gold needs much longer to get completely damped. These time-responses are strongly correlated to the phase delays of the transfer functions of the two systems.



(a) Normalized fields for gold. In red: normalized incident radiation. In blue: normalized radiation at the tip.



(b) Normalized fields for TiSiON. In red: normalized incident radiation. In blue: normalized excited radiation at the tip.

Figure 2.6: Comparison of Au and TiSiON field profiles in time. The TiSiON response better resembles the incident pulse.

2.1.2 Comparison with other materials

We want to point out the advantages and drawbacks of using titanium silicon oxynitride compared to other materials, which are not usually used for plasmonic applications. We simulated the behavior of bow-tie nanoantennas made of aluminum, titanium, titanium nitride and tungsten. It might be interesting to compare the permittivities (with real part ϵ_1 and imaginary part ϵ_2) of these materials at a wavelength of 1200 nm in order to better understand their behaviors. The permittivity values are reported in Table 2.3. Gold is reported in the table and in the following graphs for reference (for a complete comparison between gold and TiSiON, see subsection 2.1.1).

Material	ϵ_1	ϵ_2
TiSiON	-11.5	23.4
Gold	-69	4.7
Aluminum	-145.4	29.9
Titanium	1.22	25.1
Titanium nitride	-19.79	20.26
Tungsten	-7.8	26.8

Table 2.3: Real and imaginary parts of the permittivity of different materials at 1200 nm.

Among the materials reported in Table 2.3, TiN and TiSiON have the lowest losses. Nevertheless, none of these materials shows losses as small as the ones we saw for gold, which may impact their plasmonic behavior. At 1200 nm, titanium has a positive ϵ_1 , while ϵ_1 for aluminum is much larger. Not considering aluminum, TiN has the largest negative ϵ_1 .

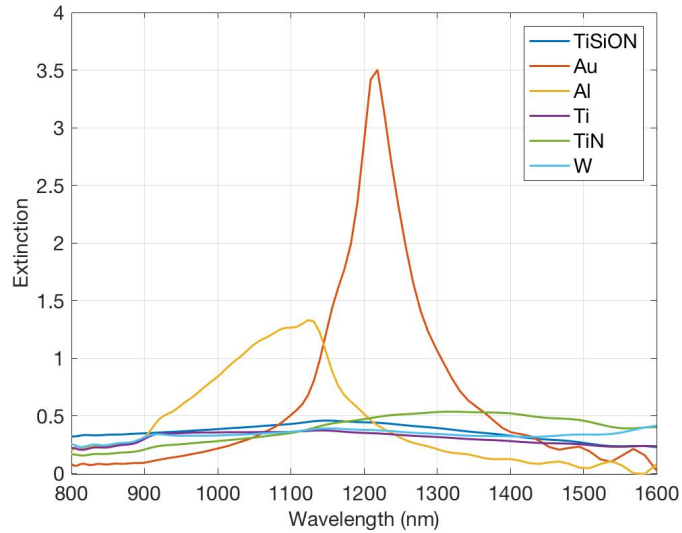
As shown in Figure 2.7a, aluminum exhibits a very high peak around 1100 nm. The very large negative ϵ_1 makes it possible for aluminum to have a surface plasmon

resonance in the near infrared despite the high losses described by the high ϵ_2 [38]. TiSiON, TiN, Ti and W have a comparable behavior, but TiN is the one that shows a higher extinction. TiN has a resonance over a wider range of frequencies. It is mainly due to the higher negative ϵ_1 and the lower losses in ϵ_2 . Furthermore, the ϵ_1 of TiN keeps decreasing with larger wavelengths. This behavior is right in between the one of aluminum, gold and other noble metals with large resonances, and the one of the other materials, whose negative ϵ_1 becomes smaller and the large ϵ_2 dampens the resonance. A similar trend can be found for the field enhancement (see Figure 2.7b). While at low wavelengths, aluminum has a much larger field enhancement than the other materials, at high wavelengths this difference tends to be smaller and smaller. TiSiON, TiN and titanium have a flat response in the field enhancement at high wavelengths, while for tungsten the enhancement starts increasing again around 1.4 μm . TiN is the one that shows the highest field enhancement (i.e. around 50 for wavelengths exceeding 1400 nm).

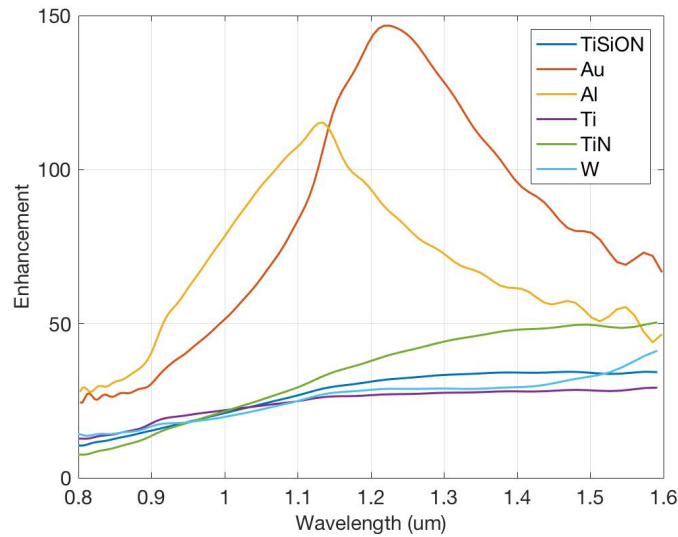
Considering the phase delay for the different materials (see Figure 2.8), aluminum is characterized by a quick variation starting from 900 nm. All the other materials have a more gradual transition. Aluminum is the material with the widest range in the phase delay over the wavelengths we simulated, while tungsten shows the narrowest. TiSiON, TiN and Ti have a similar behaviour.

Now we will analyze the different responses to an incident pulse in time for the different materials. Aluminum (see Figure 2.9) exhibits a similar behavior to the one we have already seen for gold in subsection 2.1.1. The localized surface plasmon resonance goes on for tens of femtoseconds after the incident pulse has extinguished. The plasmonic behavior of aluminum is likely due to the large negative ϵ_1 which overcomes the losses of the materials.

The responses to an exciting pulse for titanium and tungsten are shown in Fig-



(a) Extinction spectrum with different altitude dimensions with and without the etched oxide.



(b) Field enhancement with different altitude dimensions with and without the etched oxide.

Figure 2.7: Comparison of extinction spectra and field enhancement of bow-ties made of different materials (TiSiON, Au, Al, Ti, TiN, W). (Altitude = 250 nm; Base/altitude ratio = 0.75; Metal thickness = 50 nm; ROC = 10 nm; Gap = 10 nm.)

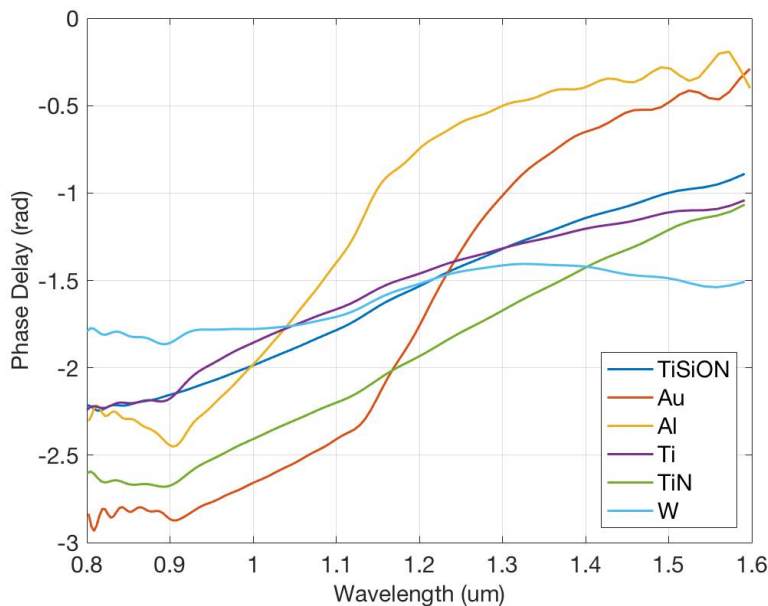


Figure 2.8: Phase delay for different materials (TiSiON, Au, Al, Ti, TiN, W).

ure 2.10. Their behavior is more similar to the one of TiSiON, as seen in subsection 2.1.1. The localized surface plasmon resonance gets damped very quickly as soon as the exciting pulse has extinguished.

Titanium nitride represents a good trade off: its response is very similar to the incident radiation and the resonance gets dampened in a limited time (see Figure 2.11).

In short, due to its large ϵ_2 , TiSiON shows a field enhancement and extinction much smaller than other metals like aluminum. At the same time, since its negative ϵ_1 is larger than the one of titanium and tungsten, TiSiON represents a better solution. Titanium nitride has better performances than TiSiON, but its versatility is limited compared to the titanium silicon oxynitride. TiSiON has indeed the great advantage of modifying the optical properties based on the dopant concentrations and produce a different optical response depending on the practical applications it is needed for.

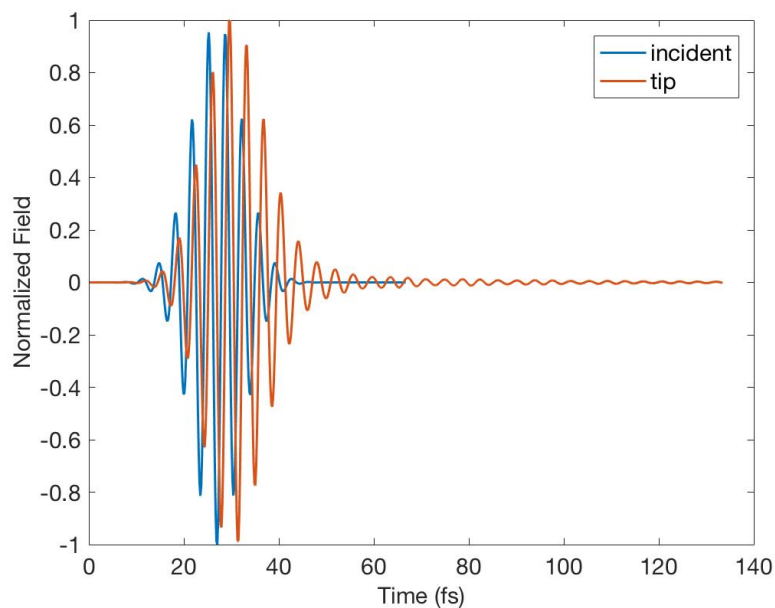
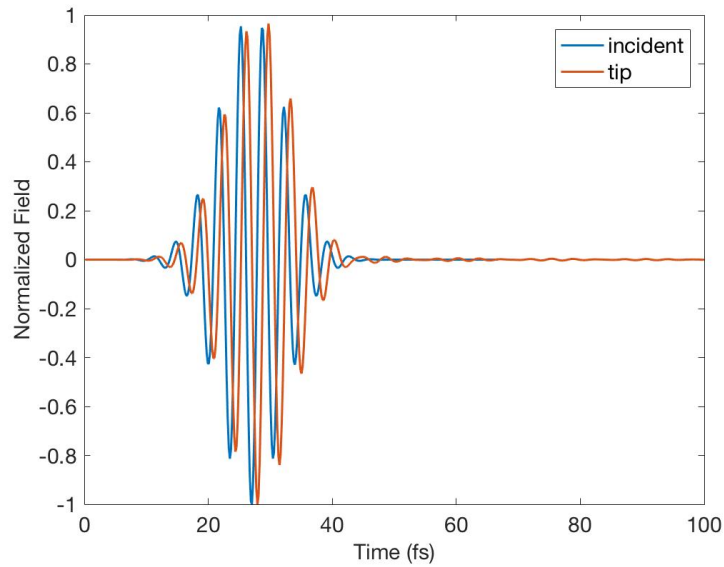


Figure 2.9: Normalized fields for aluminum. In red: normalized incident radiation. In blue: normalized excited radiation at the tip. Aluminum exhibits a similar behavior to gold.

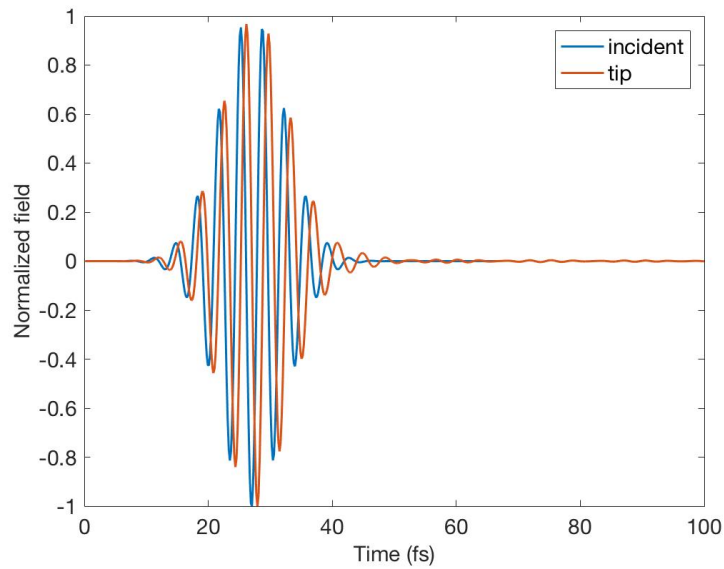
In fact, there is continuing effort to engineer the dopant concentrations in TiSiON in order to achieve a larger negative ϵ_1 and smaller losses, thus enhancing its plasmonic response and make it comparable to the titanium nitride.

2.1.3 Geometric parameters study

We will now focus on the analysis of the influence of several geometric parameters on the performance of TiSiON bow-ties. In particular, we will analyze the triangle altitude, the influence of the etched substrate thickness, the base/altitude ratio, the gap size and the connectors width.



(a) Normalized fields for titanium. In red: normalized incident radiation. In blue: normalized excited radiation at the tip.



(b) Normalized fields for tungsten. In red: normalized incident radiation. In blue: normalized excited radiation at the tip.

Figure 2.10: Comparison of titanium and tungsten field profiles in time. They both show a similar behavior to TiSiON.

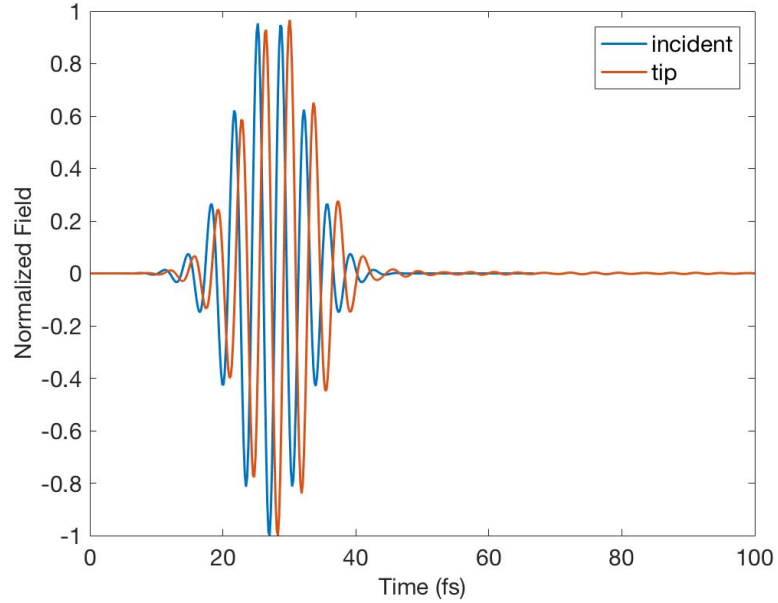


Figure 2.11: Normalized fields for TiN bow-tie structures. In red: normalized incident radiation. In blue: normalized excited radiation at the tip.

Triangle altitude study

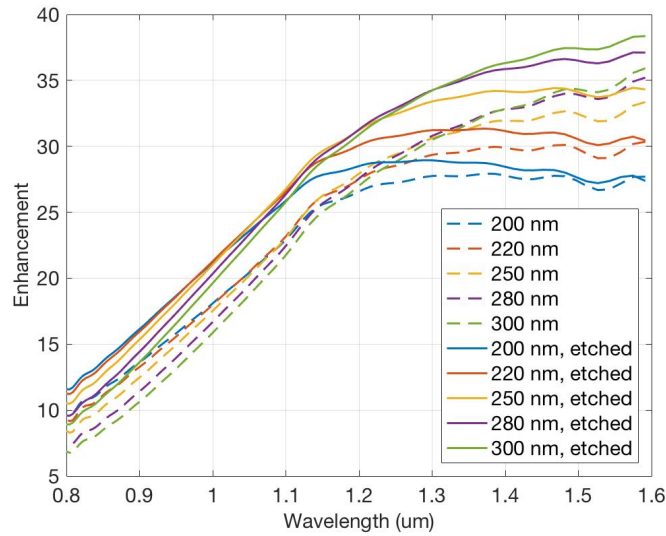
The first parametric sweep we performed is the altitude of the triangles. We swept the altitude starting from 200 nm up to 300 nm. As we can notice from Figure 2.12a, the field enhancement increases with the altitude. Since the incident field is polarized parallel to the surface, the larger the altitude the more free electrons will oscillate on the same direction of the gap and will be emitted and flow from a triangle to the other. By increasing the altitude, at high wavelengths the slope of the field enhancement increases until it is not a flat anymore. Thus, if we want a high field enhancement, we need to accept a different enhancement for different wavelengths. We reported the same simulations carried out without the overetch into the oxide. As we can see, the enhancement is lower, since many trajectories of the electrons are

forbidden due to the substrate. By etching into the oxide, the peak also blue-shifts (to lower wavelengths). As regards the extinction spectrum, Figure 2.12b shows how the extinction changes depending on the altitude. While we increase the altitude, we are also increasing the base dimension, which leads to larger structures. Thus, the absorbed energy increases as the structures become bigger. Nevertheless, we can clearly notice the cut-off wavelength around $1.2\ \mu\text{m}$ and that the peak is red-shifting (to higher wavelengths). We can see that the bow-ties with etched substrate have a blue-shifted and narrower peak, compared to the ones without an overetch into the substrate.

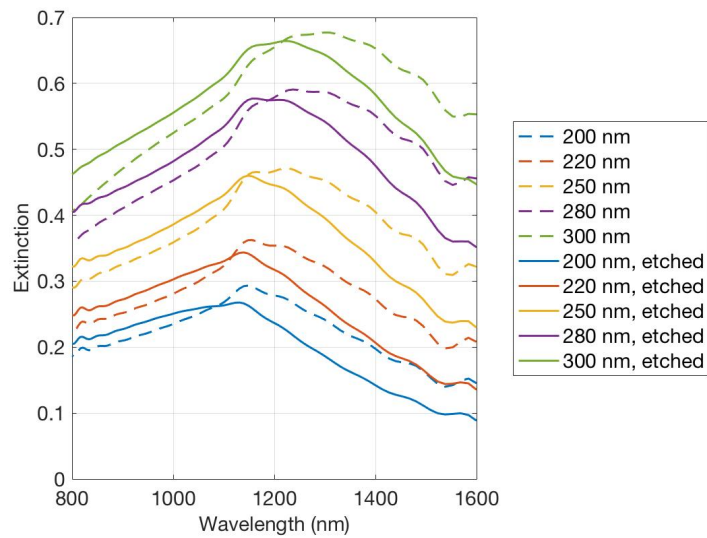
We also want to make sure that the field at the tip still follows the incident field profile in the same way even with different altitudes. In order to check it, it's worthy to plot the phase delay of the structures for different altitudes. As we can see from Figure 2.13, the phase delay just shifts vertically, without any variation on the shape of the curve. It means that the components of the incident radiation will be shifted differently if the bow-ties have a different altitude, but the relative shifting among incident wavelengths on the same structure will be constant. Thus, the field profile will be maintained.

Influence of the etched substrate

Furthermore, we simulated the behavior of the structures with different etched oxide thicknesses. We chose to compare 20 nm, 50 nm and 80 nm of etched oxide because they are reasonable values that can be achieved during the fabrication process. In Figure 2.14a we can see how etching the substrate actually leads to an increase of the field enhancement. As the etched thickness increases, the effect on the field enhancement tends to become always smaller. We are basically adding free space



(a) Field enhancement with different altitude dimensions with and without the etched oxide.



(b) Extinction spectrum with different altitude dimensions with and without the etched oxide.

Figure 2.12: Comparison of field enhancement and extinction spectrum with different altitude dimensions with and without the etched oxide. Continuous lines: with 50 nm of etched oxide. Dashed lines: no etched oxide. (Base/altitude ratio = 0.75; Metal thickness = 50 nm; ROC = 10 nm; Gap = 10 nm.)

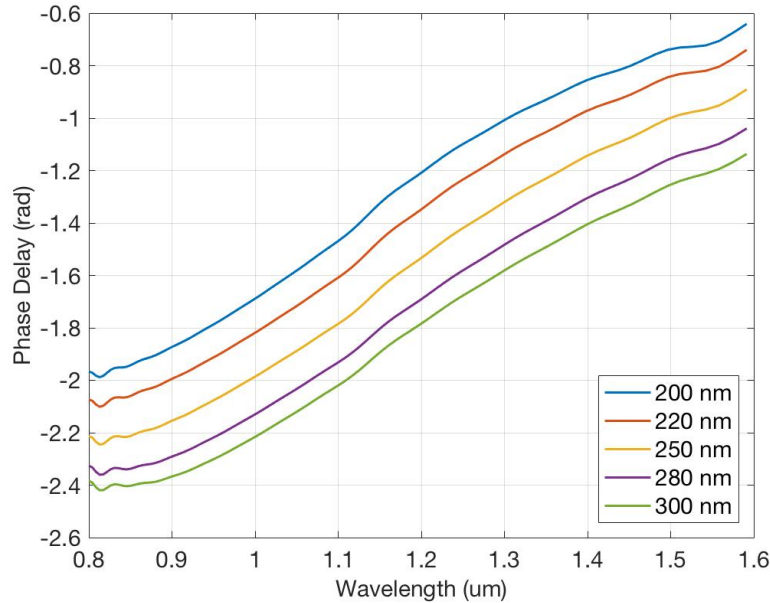
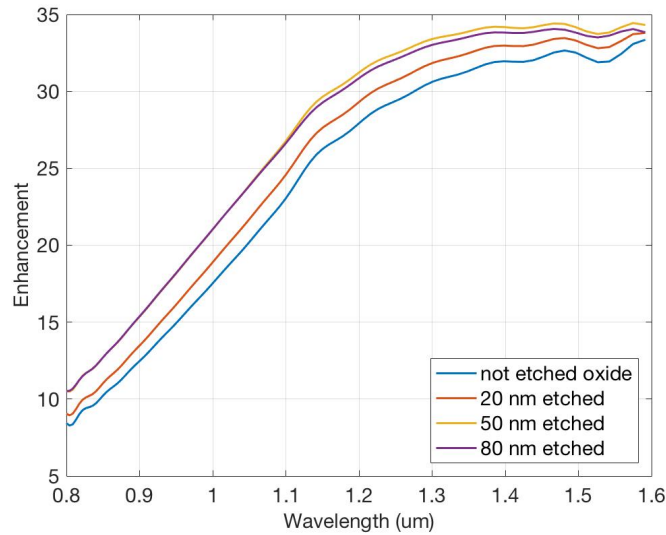


Figure 2.13: Phase delay for different altitudes.

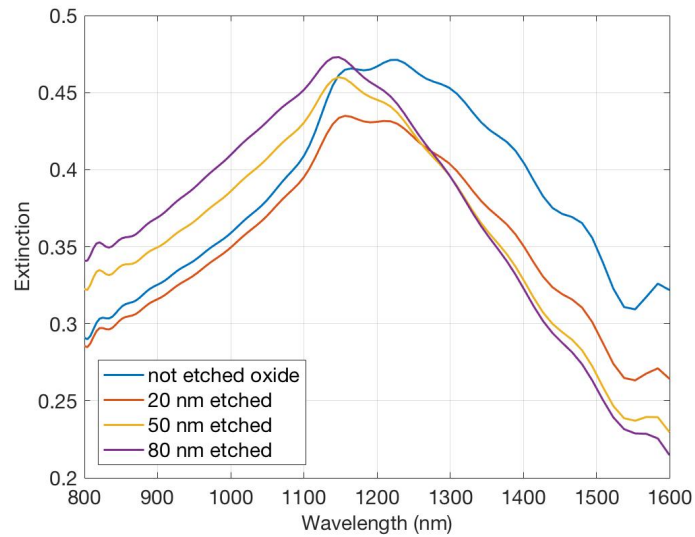
where the electrons can flow when they are emitted from the electrodes, but this space becomes negligible as it gets much larger than the gap between electrodes itself. As regards the extinction spectrum, it is interesting to notice from Figure 2.14b that the absorption of the higher wavelengths is reduced as soon as the oxide gets etched and the extinction peak slightly blue-shifts increasing the etched oxide thickness.

Base/altitude ratio study

Now that we have analyzed how the change in altitude affects the field enhancement, we can see what happens if we change the proportions of the triangle dimensions. In particular, we are going to study the variation of the base/altitude ratio. As we can see from Figure 2.15a, the enhancement keeps increasing with the base/altitude ratio. It is even higher when the base is larger than the altitude. A similar result had



(a) Field enhancement with different etched oxide thicknesses.



(b) Extinction spectrum with different etched oxide thicknesses.

Figure 2.14: Comparison of field enhancement and extinction spectrum with different etched oxide thicknesses. (Altitude = 250 nm; Base/altitude ratio = 0.75; Metal thickness = 50 nm; ROC = 10 nm; Gap = 10 nm.)

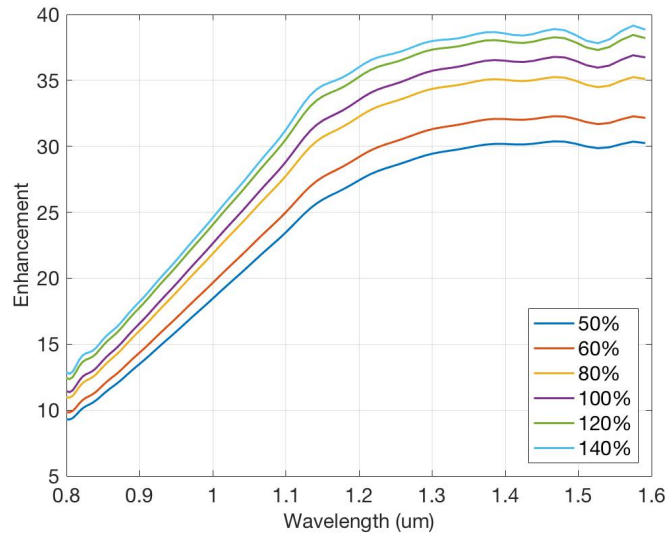
already been shown for nanotips with large opening angles [39]. At the same time, in Figure 2.15b we can see how the extinction trend is maintained unvaried for different ratios, even though it is shifted vertically because of the increasing dimensions of the structures.

Gap size study

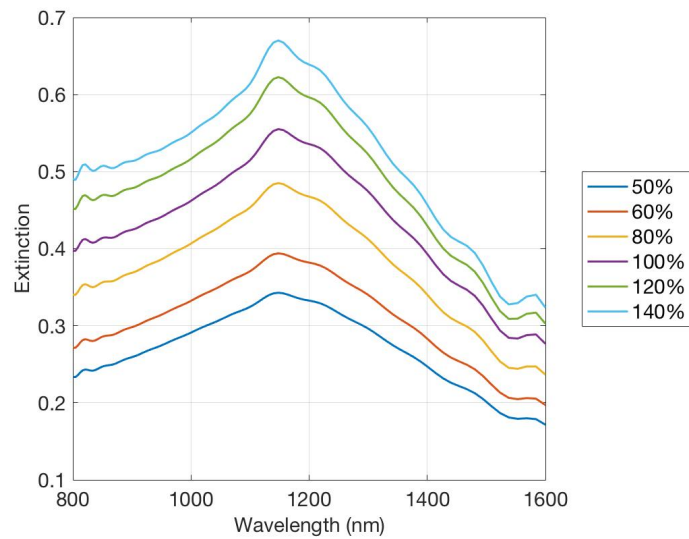
The dimension of the gap is the parameter that affects the field enhancement most. As the dimensions of the gap shrink, the field enhancement slightly increases. The simulated results with different gap dimensions are shown in Figure 2.16. As we can notice, reducing the gap from 20 nm to 10 nm, the field enhancement has basically doubled. The enhancement obtained with a gap of 30 nm is almost one third of the one obtained with a 10-nm wide gap. This trend completely agrees with the Fowler-Nordheim emission mechanism. As we have seen in Eq. (1.1), the enhancement factor is inversely proportional to the gap between the electrodes. Thus, doubling the gap, we should have a halved enhancement factor, whereas, with a three times larger gap, the enhancement will become one third of the initial value.

Connectors width study

The last analysis we performed on the TiSiON film as deposited concerns the width of the connector bars. During the previous simulations, we just defined the bow-tie structures without any connectors. In order to realize an optoelectronic detector, we need to introduce some connectors that will be used to allow a current flow through the structures and to create a network of connected devices to enhance the detection efficiency. As shown in Figure 2.17a, the field enhancement decreases as soon as a connector is introduced into the structure but the increase in the connectors



(a) Field enhancement with different base/altitude ratio.



(b) Extinction spectrum with different base/altitude ratio.

Figure 2.15: Comparison of field enhancement and extinction spectrum with different base/altitude ratios. (Altitude = 250 nm; Metal thickness = 50 nm; Etched oxide thickness = 0 nm; ROC = 10 nm; Gap = 10 nm.)

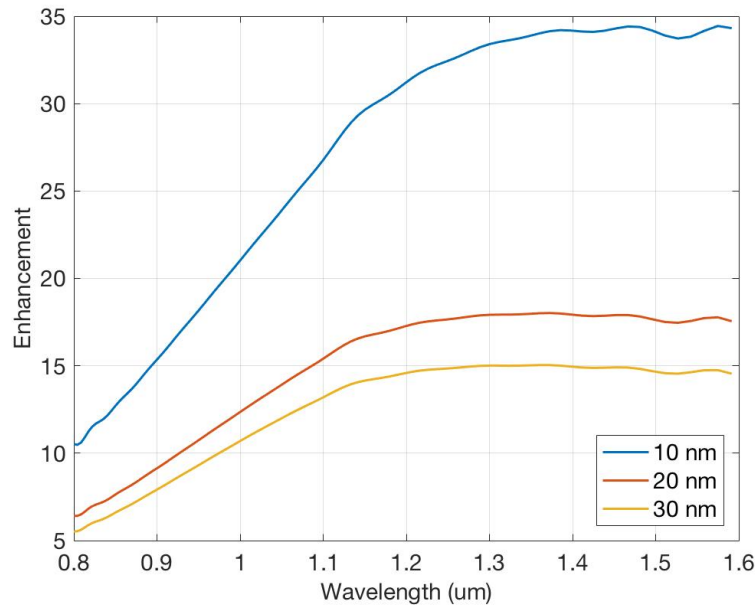
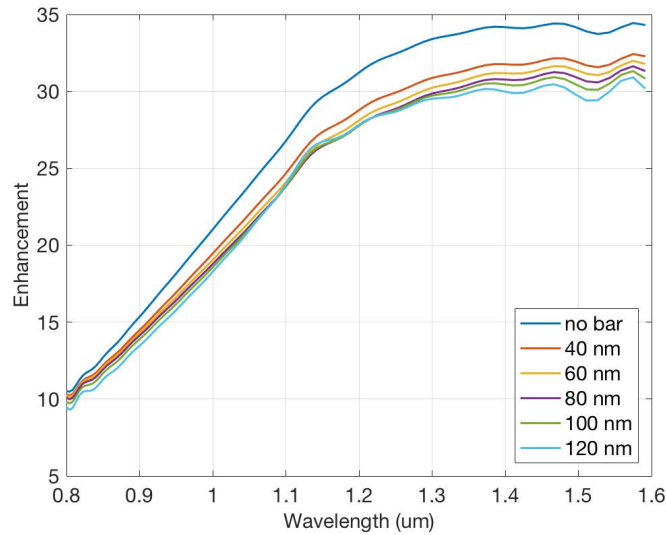
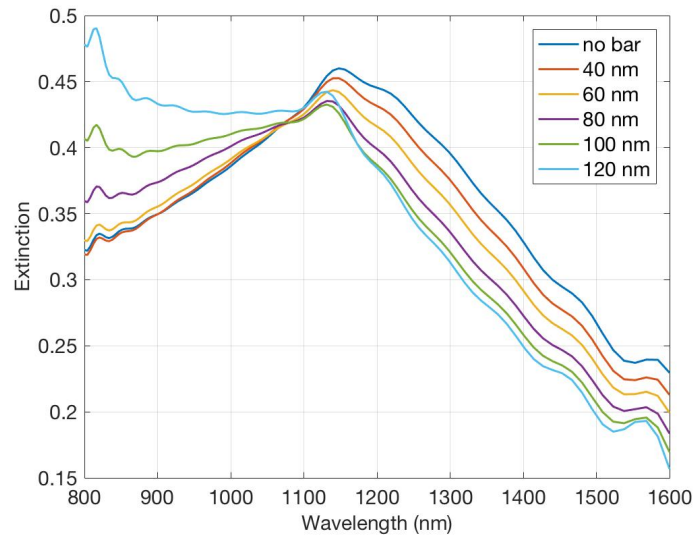


Figure 2.16: Field enhancement at the tip with different gap dimensions. (Altitude = 250 nm; Base/altitude ratio = 0.75; ROC = 10 nm; Metal thickness = 50 nm; Etched oxide thickness = 50 nm.)

width doesn't degrade the enhancement considerably. At the same time, looking at the extinction spectra in Figure 2.17b, we notice that the extinction peak slightly blue-shifts by increasing the bars dimensions. Furthermore, at low wavelengths, the extinction significantly increases as the connectors width becomes larger than 80 nm. The area between the connectors has basically become a cavity allowing its own resonant frequencies. The field at the tip remains unvaried, but the incident radiation loses more energy since the new resonant modes of the system have led to larger absorption of radiation by the wires.



(a) Field enhancement with different connectors widths.



(b) Extinction spectrum with different connectors widths.

Figure 2.17: Comparison of field enhancement and extinction spectrum with different connectors widths. (Altitude = 250 nm; Base/altitude ratio = 0.75; Metal thickness = 50 nm; Etched oxide thickness = 50 nm; ROC = 10 nm; Gap = 10 nm.)

2.2 TiSiON film after annealing

The annealing of TiSiON layer has been shown to lead to a more negative ϵ_1 , enhancing the plasmonic behavior of the film compared to the same layer as deposited [19]. We have carried a sweep of altitude for the annealed film, to point out the differences we would get fabricating devices out of as deposited or annealed film.

Table 2.4 shows the Drude-Lorentz coefficients that have been used to extract the real and imaginary permittivities of the film.

e1(inf)	2.6065 ± 0.0791
Br1	1.2528 ± 0.0853
Br2	0.81142 ± 0.0171
Br3	0.55494 ± 0.0546
Br4	2.8755 ± 0.129
Am1	6.2279 ± 1.27
Am2	19.118 ± 1.44
Am3	20.606 ± 1.55
Am4	113.21 ± 5.05
En1	3.6814 ± 0.025
En2	0.82745 ± 0.00483
En4	5.3963 ± 0.0571

Table 2.4: Optical parameters for annealed TiSiON film.

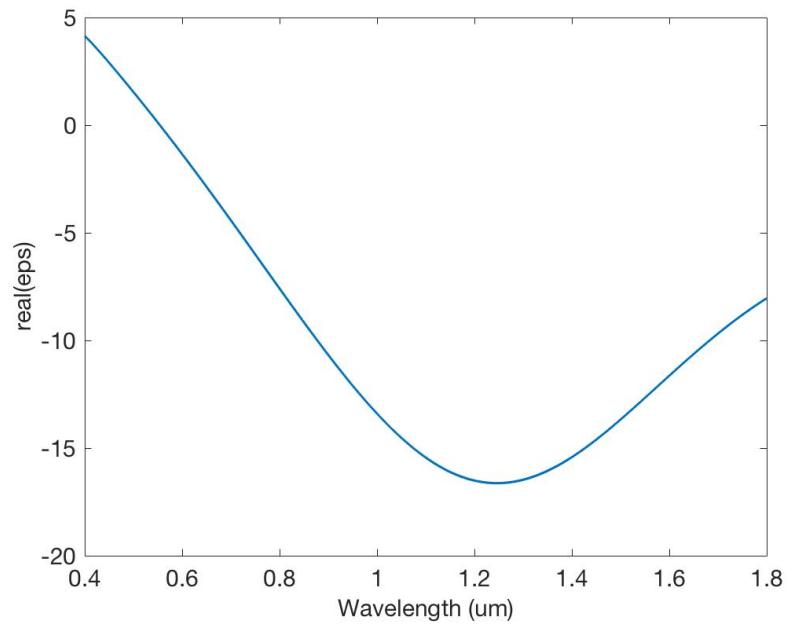
The real and imaginary parts of the permittivity of the film are shown in Figure 2.18. As we can see, the real part shows a single crossover to negative ranging from $0.4 \mu\text{m}$ and $1.8 \mu\text{m}$ and the losses increase with the wavelength. Compared to the permittivity components of the film as deposited reported in Figure 2.2, we can notice that the losses given by the imaginary part of the permittivity are comparable in the two cases. The crossover to negative in the real part of the permittivity happens around the same wavelengths (i.e around $0.6 - 0.7 \mu\text{m}$). The annealed film reaches more negative values for the real part of the permittivity, compared to the

film as deposited. This feature makes the plasmonic resonance for the annealed film stronger and its optical properties get enhanced.

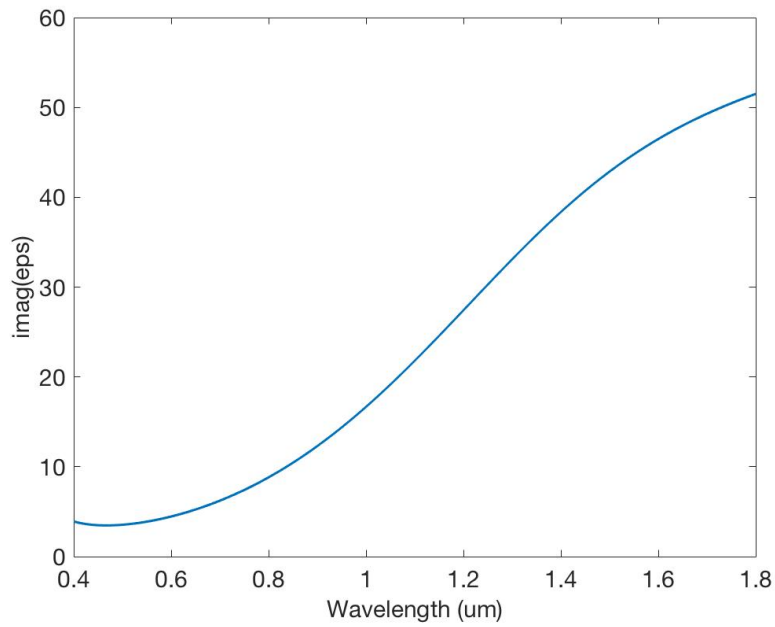
The set parameters to simulate the annealed film are the same as reported in Table 2.1. Here we will perform a sweep in the altitude. We start analyzing the annealed film performances comparing its extinction spectrum with the one of the film as deposited. Figure 2.19 shows different spectra for the two films. We can notice as the peak of the extinction slightly blue-shifts, with respect to the film as deposited. Furthermore, the peak is much higher for the annealed film. It means the plasmonic resonance is stronger and thus it absorbs more power from the incident radiation. The larger the altitude, the larger is the difference between the extinction peaks for the two different films. At low wavelengths, the absorption of the annealed film results to be higher, while at high wavelengths the two films' behaviors are similar.

As regards the field enhancement, Figure 2.20 shows the field enhancement of the two films for different altitudes. The enhancement peak of the annealed film blue-shifts and it is higher than the one of the film as deposited. For low altitudes, the enhancement decreases at large wavelengths, getting closer to the values of the as deposited film's enhancement. As the altitude becomes higher, the enhancement starts showing a flat at high wavelengths. While the flat is achieved with low altitudes for the film as deposited, if we want to get a flat with the annealed film, the bow-ties altitude must be higher. Depending on the different application, the structure's dimensions will be tuned properly.

As last step we will analyze the difference in excited field at the tip in response to an incident radiation. First, consider the phase delay of the systems given by their transfer functions. From Figure 2.21 we can see that the phase delay gets shifted vertically as the altitude changes, just like it happened with the film as deposited.



(a) Real part of the permittivity.



(b) Imaginary part of the permittivity.

Figure 2.18: Permittivity components for annealed TiSiON film.

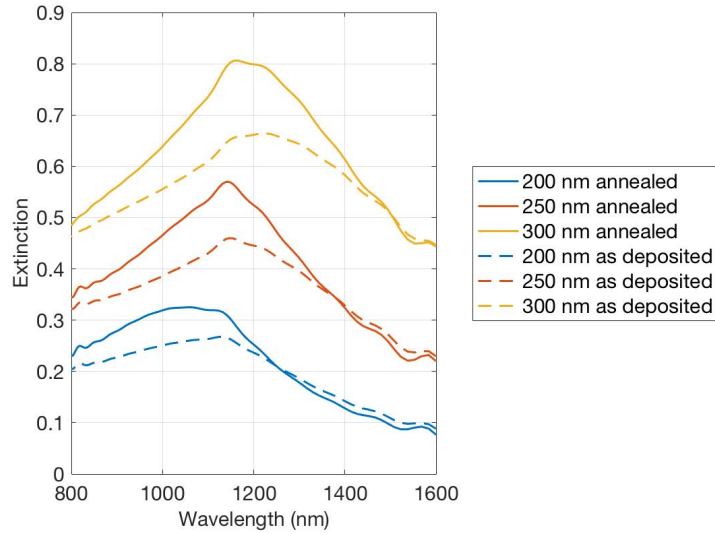


Figure 2.19: Extinction spectra for different altitudes. Continuous lines: annealed film. Dashed lines: film as deposited.

The phase delay range is a bit wider compared to the not annealed case, but the variation is still gradual and slow. To make sure the profile doesn't get affected by the different phase delay range, we can study the normalized excited field at the tip through the time and see what it looks like. We choose to study a bow-tie structure with an altitude of 250 nm. Figure 2.22 shows both the incident radiation and the excited field at the tip. We can see that even if the phase range has become wider because of the annealing, the field profile at the tip still follows the incident field.

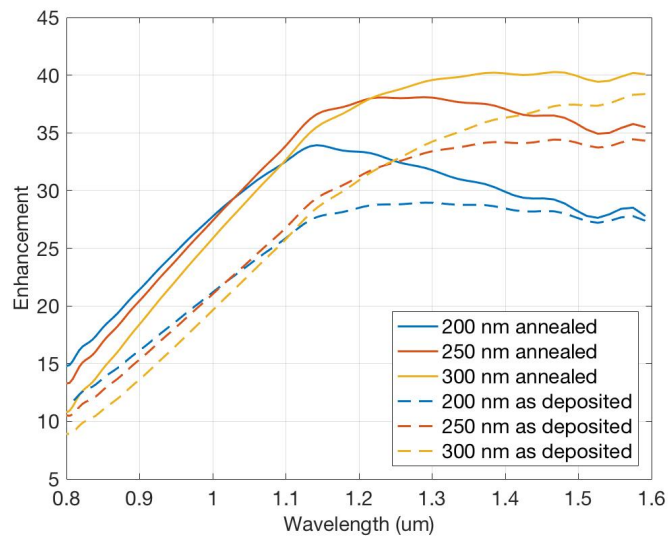


Figure 2.20: Field enhancement for different altitudes. Continuous lines: annealed film. Dashed lines: film as deposited.

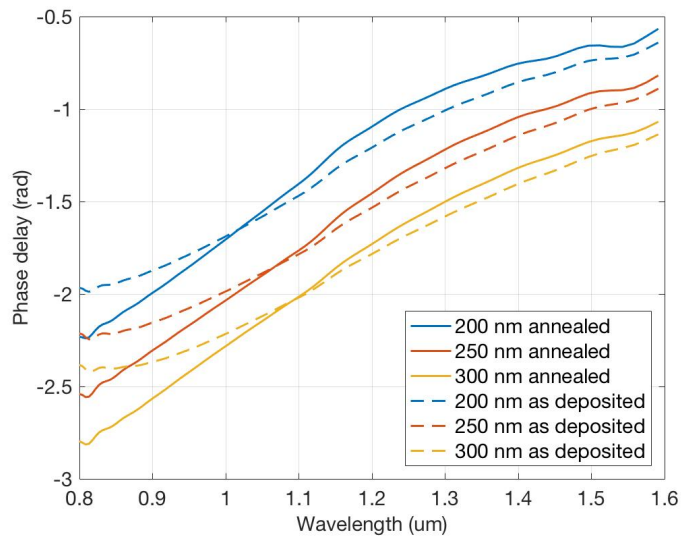


Figure 2.21: Phase delay for different altitudes. Continuous lines: annealed film. Dashed lines: film as deposited.

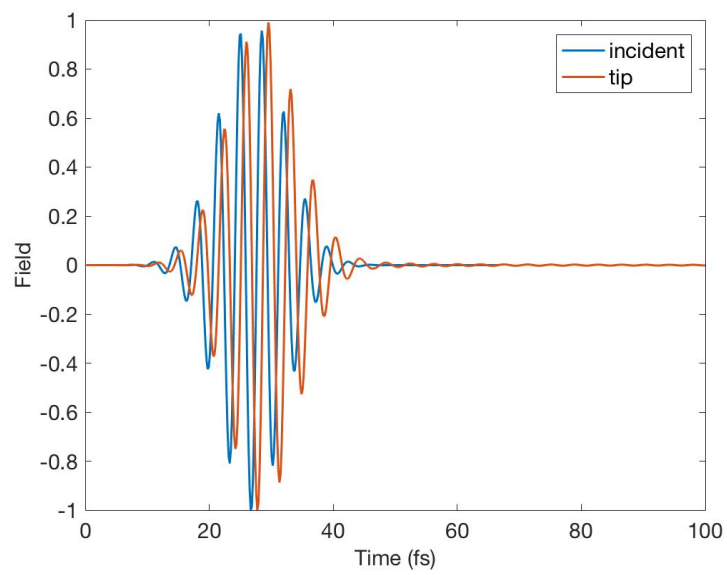


Figure 2.22: Incident field and excited field at the tip for a bow-tie structure with an altitude of 250 nm made of annealed TiSiON.

Chapter 3

Tools and techniques

In this chapter, the main fabrication and characterization tools and techniques that were used during this work will be analyzed. This chapter is meant to be a presentation of the main processes that will be used during the fabrication process development in Chapter 4.

3.1 Fabrication techniques

In this section we will present the main fabrication techniques used in our fabrication process. We will start presenting electron beam lithography (EBL), then passing to reactive ion etching (RIE) and to direct writing lithography (DWL), and ending with focused ion beam (FIB).

3.1.1 Electron Beam Lithography

Electron beam lithography (EBL) is the main fabrication step for scaling the dimension of the devices in the nanofabrication processes of the modern technologies. After

a wide use of photolithography with Direct Writing Laser or UV radiation and hard masks, to scale even more the dimensions of the features that could be written on a chip, electron beam lithography has started spreading. It is based on the use of electron sensitive materials called resists. There are positive and negative resists: the former gets weaker after the exposure to the electrons and the exposed part will be removed with the development, the latter crosslinks when exposed to the electrons and the exposed part will remain. Depending on the process, a positive or a negative resist could be more adequate.

The first step of EBL is to spin the resist over the substrate. Depending on the resist, a certain angular velocity will be used for the spinning. Afterwards, a soft bake is needed in order to remove the solvents still contained in the resist. Then the exposure can be carried out. The tool we use for EBL is Elionix ELS-F-125. Thanks to its accelerating voltage of 125 kV, Elionix can achieve features with a resolution down to 1 nm.

Before exposing a sample we need to decide the dose we want to use to write the different features. The dose is the charge used to expose the sample over the area of one pixel. The dose is calculated given a certain beam current and a certain exposure time for one pixel. If a very small resolution is required, we should set a small current, which means a large amount of time. On the other hand, if the features are large and the resolution is not an issue, a larger current can be chosen in order to reduce the exposure time. In fact, it is good practice to design the layouts on multiple layers: the small features should be written on a layer where small currents will be used, whereas high currents will be used for large features located on a different layer. A dose test is usually carried out as first optimization step in a nanofabrication process when studying the lithographic steps.

Proximity effects and their correction

Even if the diameter of the impinging beam is very small, many factors affect the actual exposed area. When the electron beam impinges on the resist, the electrons are subjected to a small angle forward scattering due to the resist electron population. Many secondary electrons are also produced in the resist and their scattering broadens the exposed area. Moreover, when the electron beam gets to the bottom of the resist, the substrate will add its own contributions due to backscattered electrons, which will go back into the resist and will expose areas that were far away from the central point the beam impinged on. The backscattered electrons from the substrate are usually assumed to be the largest contribution to the spreading of the beam dimensions. The exposing beam can be ideally approximated as a point exposure. Nevertheless, the point exposure is limited by the optics of the exposure tool and by the forward scattering in the resist. The radius of the disk we obtain under these conditions is denoted by σ_f and should be smaller than the smallest feature we want to expose in our pattern. On the other hand, the backscattered energy is distributed over a larger region of radius σ_b . The ratio between the total backscattered energy and the forward scattered one in the photoresist is the backscatter coefficient, and is indicated by η_e . Thus, if we want to take into account the interactions of the beam with the resist and the substrate, the point spread function can be modelled as the sum of two gaussians [40]:

$$E = QK \left[\frac{1}{\sigma_f^2} \exp\left(-\frac{r^2}{\sigma_f^2}\right) + \frac{\eta_e}{\sigma_b^2} \exp\left(-\frac{r^2}{\sigma_b^2}\right) \right] \quad (3.1)$$

where E (Jm^{-3}) is the energy density deposited in the resist at a location distance r from a pattern pixel irradiated with a charge of Q coulombs. For each point we

expose, the pixels in its proximity will be exposed as well, with an energy given by Eq. (3.2). Fortunately, since the acceleration voltage of the EBL system is very large, the electron beam will go through the resist limiting the forward scattering angle. But we cannot neglect the contribution given by the backscattered electrons. We can simulate the effect of a substrate and its interaction with the electron beam, and accordingly modify the dose each point receives during the exposure. The Elionix conversion software embeds a PEC script which calculates the dose correction for each point given a certain material substrate, resist thickness and layout. If the density of structures we want to expose is very high and we want to achieve a high resolution, the PEC is highly recommended.

3.1.2 Reactive Ion Etching

Reactive Ion Etching (RIE) is a dry etching technique that uses a gas glow discharge to dissociate and ionize relatively stable molecules, forming chemically reactive species. It is important to choose the gases, such that the ionized species reacts with the material to be etched to form volatile products.

The process starts with a glow-discharge to initiate the dissociation and ionization of the gas phase in order to create the etching environment, consisting of electrons, radicals, photons, positive and negative ions. The samples are placed in the same chamber on a silicon wafer, which is connected to an rf voltage source. Since the electron mobility is higher than the ion mobility, after the ignition of the plasma, the sample will acquire negative charges, setting a DC self-bias voltage. At this point, the transport of reactive intermediates from the plasma will happen by diffusion, while the positive ions will be lead to the sample by the negative DC self-bias. A reaction between the species in the plasma and the material to etch must take place.

The main etching techniques are based either on fluorine or on chlorine chemistry. Depending on the material, we will choose the appropriate chemistry. If we want to add a ballistic mechanism to the etching, argon ions can be introduced into the plasma. Its contribution will not be related to the chemistry, but rather to ballistic effects. As such, the directionality of the etching can be affected. The desorbed species from the sample will diffuse into the plasma and will be pumped out in order to avoid redeposition.

In order to achieve a good etch quality, we can tune three parameters: power, pressure and gas concentration. The higher the power, the higher the etch rate. Depending on the power, the DC self-bias voltage will vary in order to reach the power set-point. Moreover, depending on the self-bias voltage, the sample will be subjected to a higher heating process. We use a Plasma-Therm RIE, which is provided with a He cooling system in the bottom electrode, in order to limit the heating of the sample and its damage.

The pressure has a key role in the etching processes. The lower the pressure, the higher the etch rate. Furthermore, a low pressure increases the directionality of the etching, enhancing the chemical contribution to the process. A high pressure leads instead to tilted sidewalls and poor resolution.

The gas flow (sccm) also affects the etch rate. The higher the concentration, the larger the chemical contribution to the etching. If we use a gas flow consisting of different etchants, we can tune the etch rate by using different relative concentrations.

3.1.3 DWL - direct writing (photo)lithography

Direct writing photolithography is a maskless lithographic techniques used to pattern photoresists with a resolution down to about 1 μm . We use a Heidelberg μPG 101.

The exposure of the resist is carried out by a 405 nm laser diode. It is mounted on a mechanical head z-driven by a stepper motor and a piezo motor to focus on the photoresist. The substrate is loaded on a x-y movable stage: it scans the sample under the laser during the exposure. The layout is controlled by the software and, during the exposure phase, the sample is raster scanned along the x and y direction. If an area or line does not have any feature to expose, the system will skip it, directly passing to the following one. For our purposes, we will use DWL to fabricate the electrical contact pads for our devices, since they are larger in scale and do not need a high resolution.

3.1.4 Focused Ion Beam

The focused ion beam is a tool used for surface nanofabrication. It is mainly used for both nano-deposition and nano-machining. The ion beam uses a liquid metal ion source. Gallium is generally used because of its low melting point, high mass and low volatility. From the ion source, the ions are field evaporated and focused into a narrow beam using several electrostatic lenses and apertures. The schematic of the FIB configuration is shown in Figure 3.1.

To perform nano-machining, the focused ion beam is used as miller. The ions are scanned over the sample surface and their impact generates elastic ion-atom collisions, which lead to the removal of the surface atoms. If we want to perform FIB deposition instead, a gas injection system (GIS) needle must be introduced above the sample surface. A gas phase organometallic compound is let flow in the path of the ion beam. When the beam strikes the gas, it decomposes and the metallic part gets adsorbed on to the sample surface. Secondary emission products like organic atoms are then removed thanks to a vacuum system. A schematic of the platinum

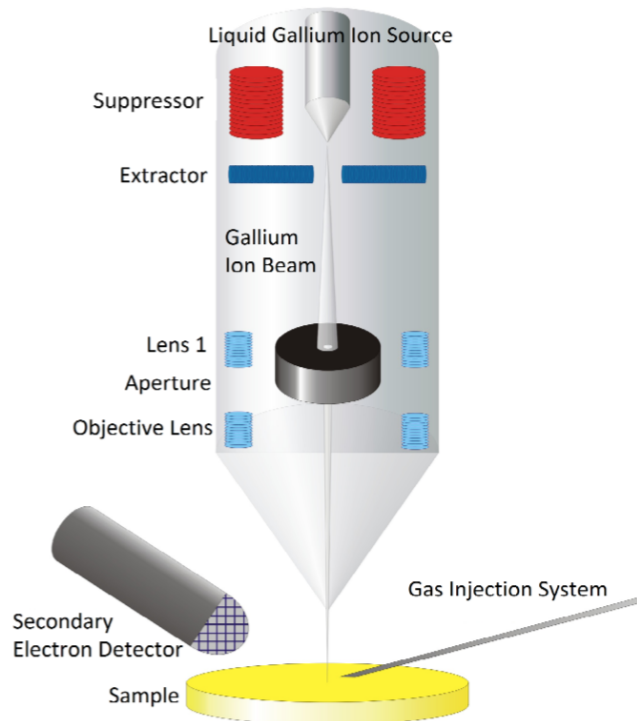


Figure 3.1: Schematic diagram of a FIB system. [41]

deposition process is shown in Figure 3.2.

We use a FEI-Helios 600 Nanolab dual beam FIB. It is provided both with a FIB system and a SEM column. Their combined use can achieve tasks beyond the limitations of either individual system, like for the preparation of a TEM lamella (see subsection 4.2.1). The schematic of a dual beam system is reported in Figure 3.3. As we can see, the two beams have two different incident angles on the surface: the SEM electron beam is perpendicular to the surface, while the ion beam impinges at 52° if the sample is not tilted. By finding the eucentric-height and a co-incident point, tilting the sample will not affect the position of the two beams and they will be focused on the same point over the surface. We can perform both e-beam and ion

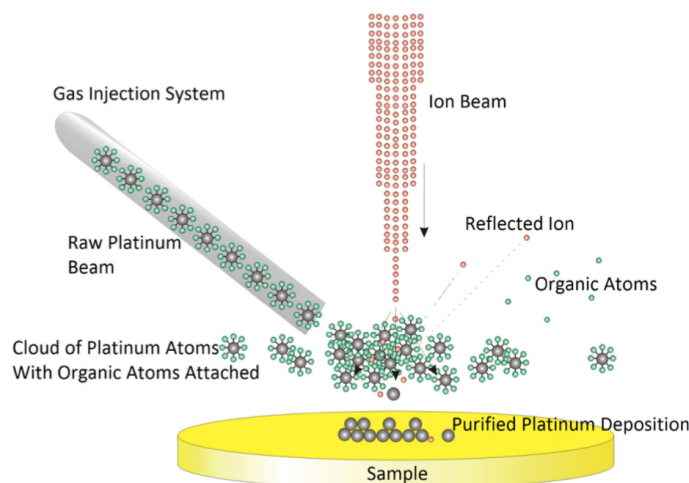


Figure 3.2: Schematic diagram of FIB platinum deposition process. [41]

beam deposition/milling. The electron beam will be slower but more gentle on the sample, while the ion beam is usually faster but more aggressive. The two techniques are usually combined in order to manage both to protect the sample and to achieve a reasonable process speed. Thanks to the tilting, we can either mill the sample with the ions perpendicular to the surface (when the sample is tilted at 52°) or mill the profile when we are looking at the cross-section with the sample tilted at 0° .

3.2 Characterization techniques

In this section we will present the main characterization tools and techniques we used during this thesis project. We will analyze ellipsometry and transmission electron microscopy (TEM), which allows us to carry out the electron energy loss spectroscopy (EELS) for the chemical characterization of a material.

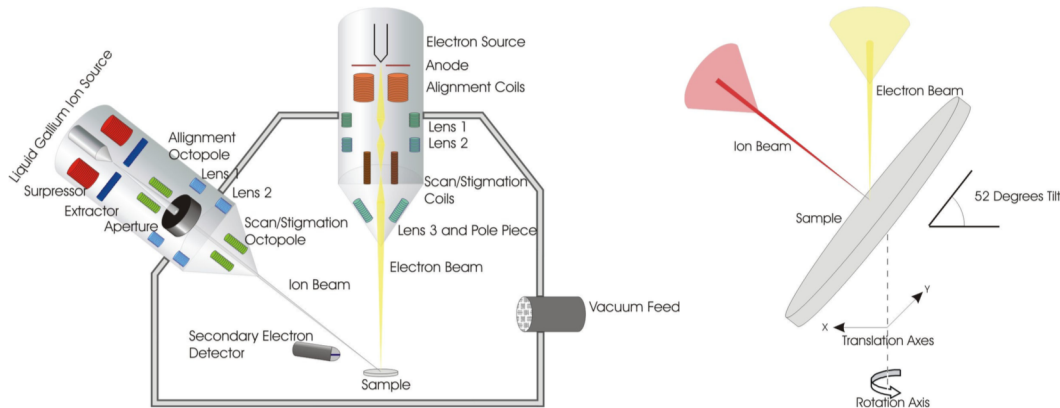


Figure 3.3: Schematic diagram of a two-beam configuration, combining both a FIB and a SEM column. [41]

3.2.1 Ellipsometry

Spectroscopic ellipsometry is a fundamental technique used to measure the thickness of dielectric thin films. We consider a three mediums system: air, a dielectric thin film and the substrate. When polarized light travelling in the air impinges on a dielectric thin film, part of it will be reflected by the same incident angle, while the other part will be refracted into the thin film. When the refracted light gets to the substrate, again it will be both reflected and refracted. Within a thin film, multiple reflections happen, such that the reflected light in the air is given by a summation of many components. These components are coming both from the very first reflection of the impinging light and all the other contributions given by the light refracted and reflected within the thin film (see Figure 3.4). Thus, depending on the thickness of the thin film, the light will travel for a larger or smaller distance, causing different interferences in the reflected light.

The main concept behind ellipsometry is the analysis of the change in polarization

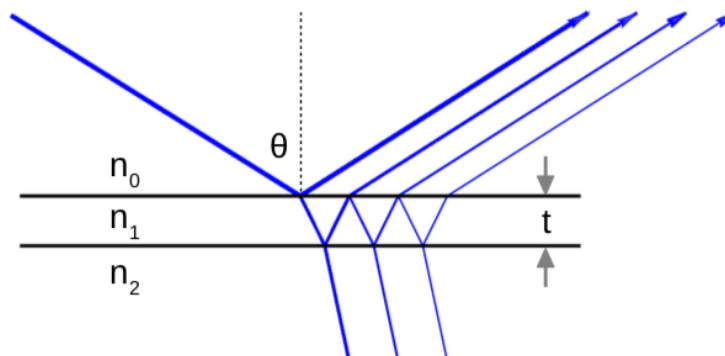


Figure 3.4: Model of light reflection in a three mediums system with different refractive indexes. Multiple reflections happen within the thin film and the total reflected light is given by the interference (constructive or destructive) of all the reflected contributions. [44]

of the light beam reflected from the surface of the sample. We use a Film Sense FS-1 Multi-Wavelength Ellipsometer. It acquires ellipsometric data at four different wavelengths: 465 nm (blue), 525 nm (green), 590 nm (yellow) and 635 nm (red) [44]. Ellipsometry is insensitive to the intensity of the reflected beam: the phase of the polarization carries the information, regardless the particular kind of film the light is reflected on.

A beam of light contains an electric field component oscillating perpendicular to the direction of propagation of the beam itself. The orientation and the phase of the electric field define the polarization state of the beam. A coordinate system can be defined by the plane of reflection of the incident beam on a sample: the component of the electric field oscillating parallel to the plane of incidence is defined as "p-polarized", while the component oscillating perpendicular to the plane of incidence is said "s-polarized". An ellipsometer is provided with a polarizer that linearly polarizes the incident light along the p- and s-planes. When the light interacts with the sample under measurement, the reflected light will show a different polarization,

which will be a generic elliptical one (see Figure 3.5). The name "ellipsometry" was given after the elliptical polarization of the reflected light.

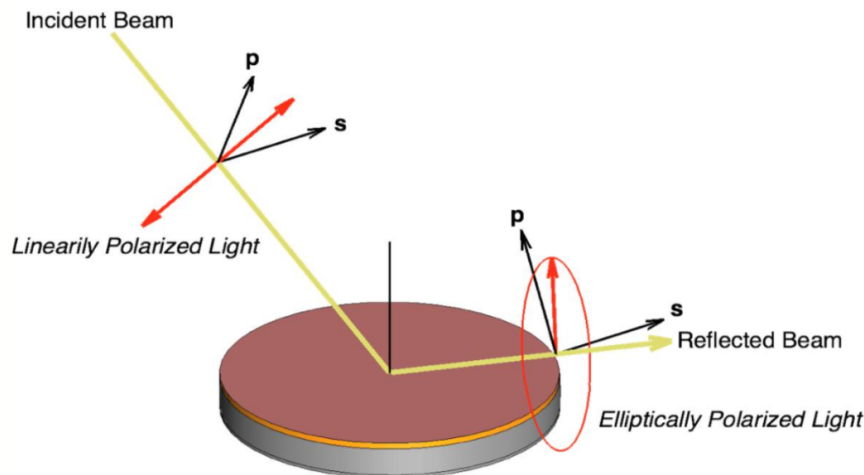


Figure 3.5: Model of the spectroscopic ellipsometry principle. An incident linearly polarized beam is reflected on the surface of the sample. The reflected beam is elliptically polarized light. [44]

An analyzing detector will evaluate the elliptical polarization in output. Ellipsometry measure the ratio and phase difference between the p-polarized and s-polarized reflected light. An ellipsometric measurement is usually given as:

$$\frac{R_p}{R_s} = \tan \Psi e^{i\Delta} \quad (3.2)$$

where R_p and R_s are the complex reflection coefficients for p- and s-polarized light. Ψ is related to the magnitude of the ratio between p- and s-reflected light, while Δ is the phase difference between the two components.

After a sample is measured, a model is constructed to calculate the predicted response of the reflection. Since the phase delay is a periodic function, there are multiple combinations of model fit parameters that generate the same ellipsometric data.

Finding the best match between the model and the experiment is typically achieved through regression. By using estimator, like the Mean Squared Error (MSE), the difference between the model curves and the experimental results is calculated. The model fit parameters are allowed to vary until the minimum MSE is reached. Many local minima are usually present, which are given by different sets of parameters, but the absolute minimum will give the most accurate result in the thickness value.

3.2.2 Transmission Electron Microscopy

In a conventional transmission electron microscope, a thin specimen is irradiated with an electron beam of uniform current density. An electron gun emits electrons by thermionic emission from tungsten hairpin cathodes or LaB₆ rods, or by field emission from pointed tungsten filament [42]. A two-stage condenser-lens system is used to tune the illumination aperture and the dimension of the illuminated area on the specimen. The electron intensity distribution is imaged with a lens system onto a fluorescent screen. A schematic of a TEM is shown in Figure 3.6.

Electrons strongly interact with atoms by elastic and inelastic scattering. Depending on the composition of the specimen and on the resolution we want to achieve, the specimen must be very thin. Usually the TEM specimen have a thickness smaller than 100 nm. Transmission electron microscopy can achieve a sub-nm resolution. It is mainly due to the elastic scattering, which is a highly localized process happening between the electrons and the nucleus of the atoms composing the imaged region. We use a HRTEM JEOL 2010F, which is a high resolution TEM. It uses acceleration voltages between 120 kV and 200 kV and has a nominal point to point resolution of 0.19 nm. It is provided with the setup to perform scanning electron microscopy (STEM) and electron energy loss spectroscopy (EELS).

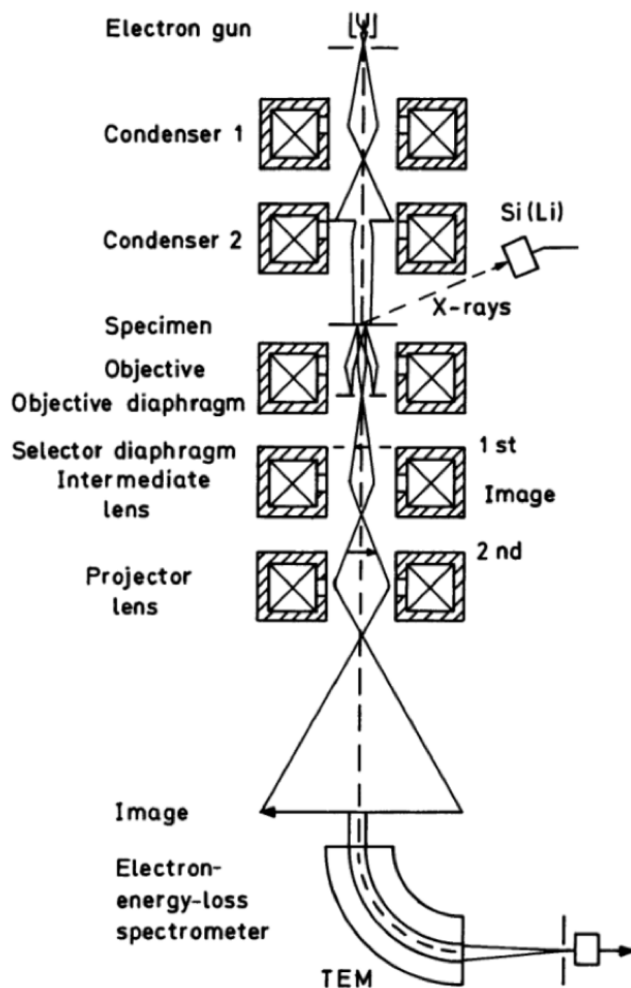


Figure 3.6: Schematic of a transmission electron microscope equipped for additional x-rays and electron energy loss spectroscopy. [42]

Scanning Transmission Electron Microscopy

STEM is composed by a field emission gun, an electromagnetic lenses system to focus the electrons into a "probe" of very small dimensions (about 1 nm or less), an electron-detection system and an electron spectrometer, used for electron energy loss

spectroscopy. The spectrometer separates the currents of unscattered electrons $I_u n$, of elastically scattered electrons $I_e l$ and of inelastically scattered electrons $I_i n$. The main advantage of using a STEM is that the contrast can be enhanced by collecting different signals and by elaborating them to display differences and/or ratios. The sub-atomic resolution is then improved compared to a conventional TEM system.

Electron Energy-Loss Spectroscopy

Electron energy-loss spectroscopy involves the measurement of the energy distribution of the electrons that have interacted with the specimen and lost their energy due to inelastic scattering. Thanks to the small beam dimension a TEM can achieve, EELS carried out in a TEM has a very high resolution. TEM-EELS is mainly based on a magnetic prism, in which an uniform magnetic field B of the order of 0.01 T is generated. In a magnetic field, the electron trajectory is bended to a circular path, whose radius R is given by the following equation:

$$R = \frac{mv}{eB} \quad (3.3)$$

where m is the electron mass, e is the elemental charge of the electron, B is the applied magnetic field and v is the speed of the electron, which means its energy. Electrons that have lost different energies will have different paths. Depending of the radius of curvature of their trajectories, electrons will experience an increase or decrease in their path length within the field, related to a larger or smaller deflection angle. If the beam impinging on the prism has originated from a point object (as it happens in a STEM), then the electrons of a given energy are returned to a single image point. Thus, the different electron energies will generate a focused spectrum in a plane passing through that point. The EELS detector is placed on this plane, in

order to collect the data of the energy spectrum. Figure 3.7 shows the schematic of the magnetic prism and how its working principle to form the energy-loss spectrum on a plane at the output.

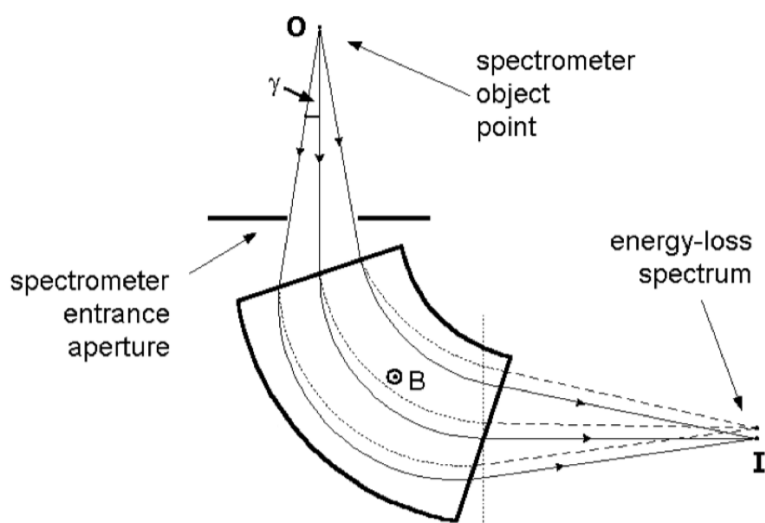


Figure 3.7: Schematic of a magnetic prism used for EELS. The paths inside the prism will depend on the speed, and so on the energy, of the electrons. An energy-loss spectrum is produced on a plane passing through the image point at the end of the prism. [43]

Energy-loss spectra show some common and peculiar features. In the low-loss region, up to tens of volts, a large peak occurs at 0 eV. For a very thin specimen, the 0 eV peak is the largest peak, since the electrons don't undergo inelastic scattering and the energy-loss due to elastic scattering is too low to be measured. Other smaller peaks usually occur in the low-loss region. They are called plasmonic peaks and arise from elastic scattering due to plasma resonances of conduction or valence electrons. Much smaller peaks are present at very high energies: these are the peaks we are interested in, if we want to carry out an analysis of the chemical composition. The

atomic electrons located in inner shells have binding energies that are hundreds or thousands of eV. Their excitation by a transmitted electron generates ionization edges in the energy-loss spectrum at very high energies. Since core-electron binding energies differ for each element and each kind of shell, the ionization shells are used to identify the elements that are present in the specimen. Each element also shows a peak at low energies (up to hundreds of eV). In our work, we will carry out a low energy EELS to evaluate the composition films.

Chapter 4

Fabrication process for Titanium Silicon Oxynitride

Titanium silicon oxynitride (TiSiON) is a new material which has been engineered and produced for the first time by the NanoGroup at Boston University. We are collaborating with them to develop a reliable process for fabricating nanostructures of TiSiON. We also performed the electrical and optical testings. Most of the work for the development of the fabrication process has been carried out in the NanoStructures Laboratory (NSL) at MIT.

In the following sections, the fabrication process development is discussed, starting from the elemental composition analysis of the material. We then develop an etching recipe, analyzing different etchants and several materials used as hard masks for nanopatterning bow-tie structures having few-nm tip radii for large field enhancement factors.

4.1 Sputtering of the film

A ≈ 50 -nm thick TiSiON film was sputtered using a reactive magnetron sputtering (MSP) deposition on both p-type (100) Si and glass substrates in a pure N₂ gas atmosphere with a flow rate of 10 sccm at a deposition rate of about 3.5 nm/min. A DC cathode was incorporated using a Ti (99.995% purity) target and powered at 200 W. When integrating Si-dopants, a reactive co-deposition was carried out by adding a RF cathode using either a Si (99.999%) or a SiO₂ (99.995%) target. The deposition was performed with cathodes in a confocal arrangement distanced approximately 100 mm from the substrate, with a tilting angle of about 30° from the substrate normal. A post-deposition annealing was performed on some samples for 1 hour at a temperature of 700 °C [19].

4.2 Elemental composition study

To start our fabrication process development, we analyzed the chemical composition of the material, in order to better understand its chemistry and to make clear the relative concentrations of the different elements in the film. Our work on the composition analysis is based on the preparation of a TEM lamella using the FIB, in order to finally carry out an electron energy-loss spectroscopy.

4.2.1 TEM lamella preparation

The preparation of a TEM lamella is a very delicate process. Our goal is to realize a TEM lamella with a thickness smaller than 100 nm. Since the FIB is an intrusive nanofabrication techniques, we need to pay attention not to damage the sample during the process. Figure 4.1 shows the setup of the FIB stage for the TEM lamella

preparation. We can see the sample on one side, while on the other side the TEM grid holder is placed. We placed one TEM copper grid in one slot of the holder. Our goal is to fabricate a lamella from the sample surface and then move it onto the TEM grid.

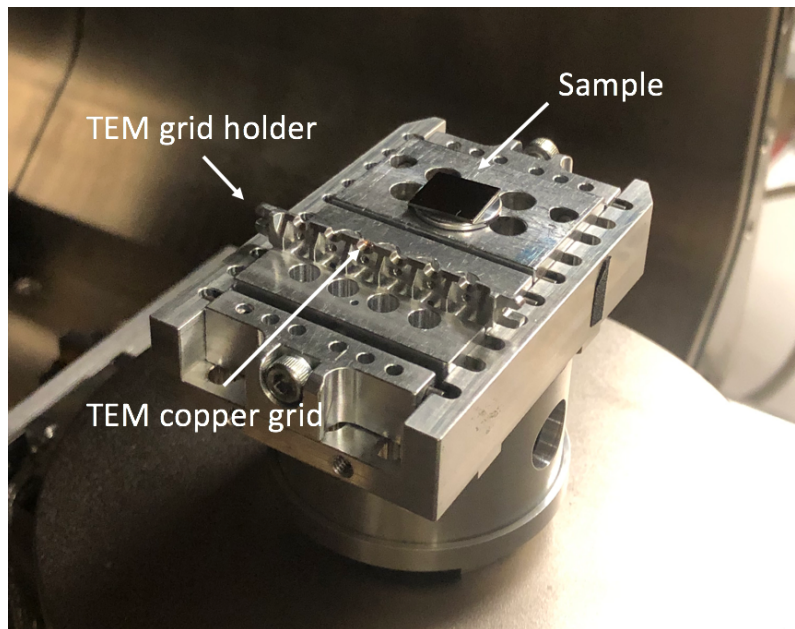


Figure 4.1: Setup of the FIB stage for a TEM lamella preparation. The sample, the TEM grid holder and the TEM copper grid are pointed out.

We need to tilt the stage many times during the process, so we first find the eucentric-height, which is that height of the stage that allows us to tilt the sample and have the beam still focused over the same point. The second preliminary step consists of finding a co-incident point for the electron and ion beams, such that they are both focused on the same point. This way, we can finally exploit the combined actions of the two beams to prepare a TEM lamella. The process is very aggressive on the sample, so we first need to deposit a protection layer of platinum localized on the surface of the sample where we want to fabricate the lamella. The

Pt deposition is carried out in two separate steps: a first thin deposition is made with the electron beam, while a second fast and thicker deposition is carried out with the ion beam. The former will be used to protect the surface of the sample from the second deposition, which is used to form a thick layer of platinum at a reasonable speed with higher acceleration voltage and current. The platinum layer will need to be around $3\ \mu\text{m}$, in order to withstand the whole process. Thus, we can mill two later trenches by using the ion beam. The thickness of the TEM lamella at this point is kept around $2\ \mu\text{m}$: it will get thinned in the end of the process. We want to drill about $5\text{-}10\ \mu\text{m}$. Figure 4.2(a) shows an image of the sample taken with the ion beam after Pt deposition and milling. Then we want to perform a J-cut in the TEM lamella as shown in Figure 4.2(b). This step is carried out at 30° with the ion beam. It is crucial to make sure the J-cut gets to the other side of the lamella, otherwise we won't be able to remove it from its location. At 30° , we are able to see one side of the lamella with the ion beam, as shown in Figure 4.2(c), while by tilting to 52° the electron beam will allow us to see the other side of the lamella (see Figure 4.2(d)). If the cut gets through the whole lamella, we can go on, otherwise we will mill the J-cut deeper.

The manipulation of the lamella is performed using an omniprobe, properly sharpened in the beginning of the process. Figure 4.3(a) shows the insertion of the omniprobe. We need to anchor the omniprobe to the lamella. Thus, we deposit some platinum to connect the omniprobe to the lamella (see Figure 4.3(b)). We can perform this step using the ion beam, since the sample is already protected by the platinum layer we deposited in the beginning. As soon as the omniprobe is anchored to the lamella, we can cut the last part we left uncut when we performed the J-cut (see Figure 4.3(3)). Now the lamella should be suspended, while the omniprobe is holding it. Thus, we can remove it from its location by raising the omniprobe, as

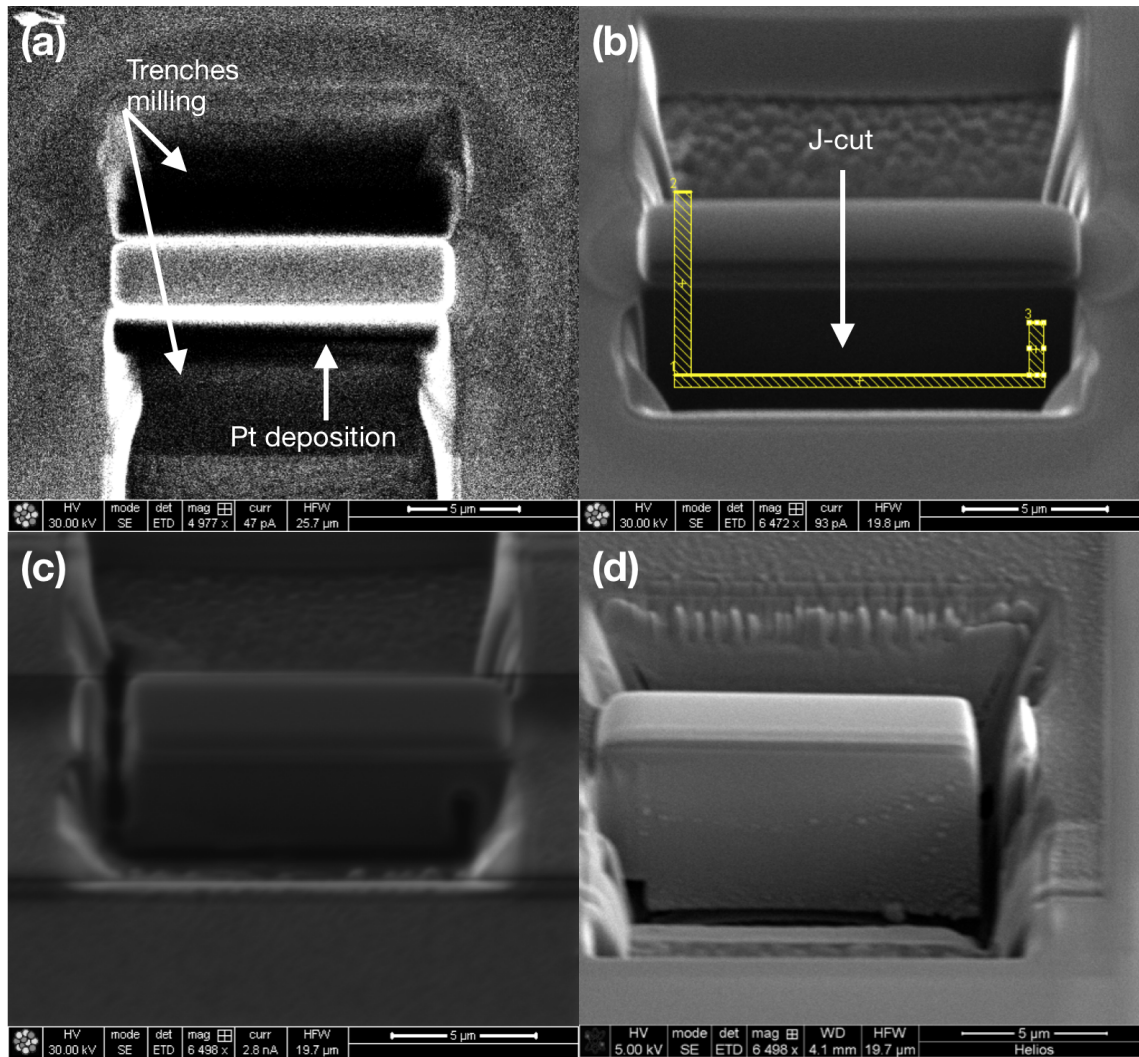


Figure 4.2: TEM lamella preparation. (a) Ion beam image showing the lamella after Pt deposition and trenches milling. (b) Pattern of the J-cut to perform with the ion beam at 30°. (c) Ion beam image of the J-cut. (d) Electron beam image of the J-cut. It images the opposite side with respect to the one we can see with the ion beam.

shown in Figure 4.3(d).

The omniprobe is used to bring the lamella on the TEM grid. Once we are on the grid, we need to place the lamella such that the two bottom corners touch the grid, as shown in Figure 4.4(a). Then we deposit some platinum on these corners and we cut the omniprobe (see Figure 4.4(b)). The lamella is now attached to the TEM grid and is ready to be thinned. Figure 4.4(c) shows the TEM lamella after removing the omniprobe before thinning.

The thinning of a TEM lamella is a very delicate process. We want to shrink the lamella thickness down to less than 100 nm. We use the ion beam to mill at 52° , but we need to be very careful and tune the acceleration voltage and the current at each step in order to preserve the lamella. We performed the thinning using a staircase fashion. At each step we shrank the width of the milled area, so that in the end our TEM lamella will look like a staircase. This technique allows us to have thick areas to try to perform the thinning on again, in case something goes wrong. The first steps are made with a high acceleration voltage and current, since the lamella is still thick. As soon as it gets thinner, we decrease both the acceleration voltage and the current. Focusing is crucial during this step, if we want to achieve a proper thickness. To make sure we mill until the bottom of the lamella, at each step we perform an additional milling by tilting the stage by $\pm 1.5^\circ$. Figure 4.5(a) shows a top view of the lamella after thinning. We can clearly see its staircase shape. It's also interesting to notice the deposited platinum on the bottom corners of the lamella, and the remains of the omniprobe we used to manipulate the sample. Figure 4.5(b) shows a cross-section of the lamella. The staircase shape is also clear from this point of view. It is important to see how the platinum protection layer has thinned in the central part because of the damages due to the ion beam. This is the reason why the initial platinum deposition must be thick enough. As we can see, the central part of

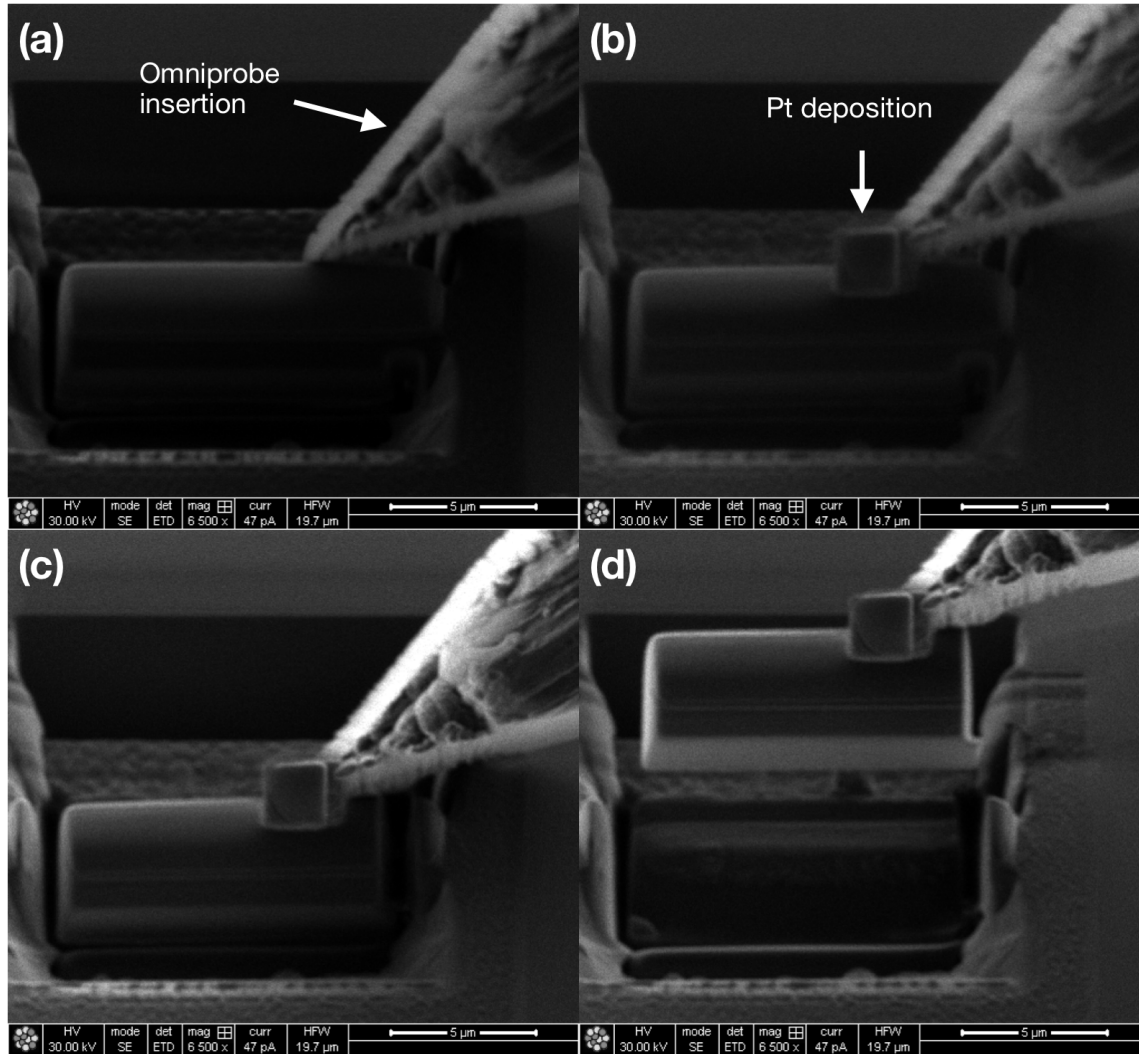


Figure 4.3: TEM lamella preparation. (a) Omniprobe insertion above the TEM lamella. (b) Pt deposition to anchor the Omniprobe to the lamella. (c) Cut of the last part of the lamella that is keeping it connected to the sample. (d) Raise of the Omniprobe and removal of the lamella from the sample.

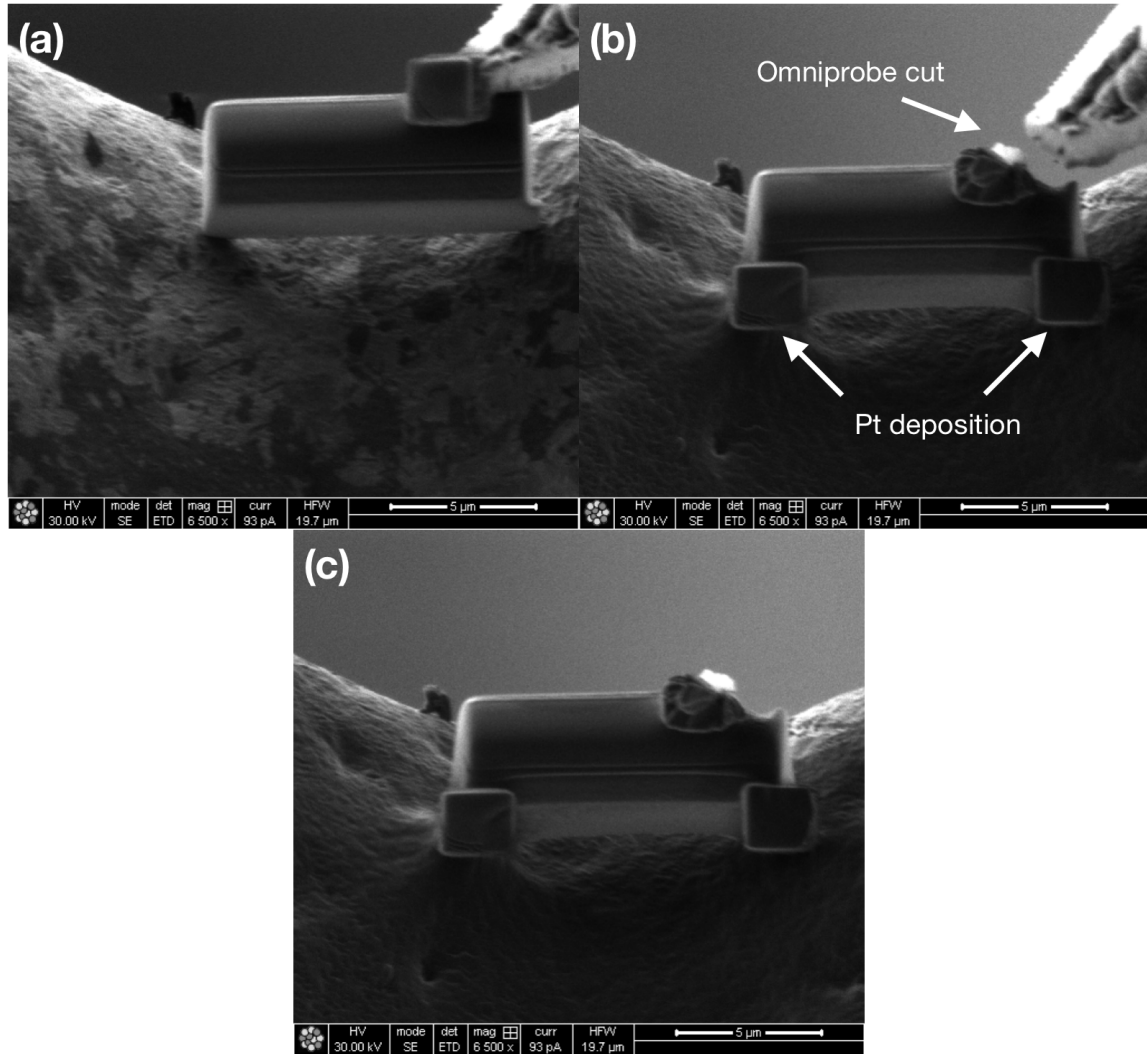


Figure 4.4: TEM lamella preparation. (a) The lamella is placed on the TEM grid. (b) Pt deposition to anchor the lamella to the TEM grid. Mill the omniprobe in order to free the lamella. (c) TEM lamella attached to the TEM grid after omniprobe removal.

the lamella has a different shade. It is due to the different production of secondary electrons due to the thickness of the lamella. Figure 4.5(c) shows a top view of the thinnest part of the lamella. The measured thickness is about 84 nm, but the image comes from a projection on a plane and the lamella is not uniformly thick in its height: the bottom part will be thicker than the superficial part. Thus, the thickness of the specimen we will analyze using the TEM is smaller than 84 nm, which is the maximum thickness of the lamella all over its height. Figure 4.5(d) is a cross-section of the thin part of the lamella. The ion-beam deposited platinum protection layer has been thinned to about 100 nm. The e-beam deposited layer can be clearly seen underneath. TiSiON is the dark 50-nm thick layer right under the two Pt layers.

4.2.2 TEM analysis and EELS results

We started analyzing the thin film morphology with an high resolution TEM. Using the TEM lamella we prepared with the dual beam FIB, we obtained the image shown in Figure 4.6. We can see that the deposited film is not uniform in space. The FIB deposited platinum has damaged the surface of TiSiON, such that the interface is not well-defined.

Figure 4.7 shows an image at a higher magnification. The native oxide is visible between the substrate and the thin film. It is also possible to notice the silicon lattice in the substrate.

We carried out low energy electron energy-loss spectroscopy on the thin film in order to analyze its chemical composition. We carried out several sweeps around the sample in order to get a proper information about how the dopant concentrations vary in space. The spectrum images we got are of the same type as shown in Figure 4.8.

The edges we want to find for titanium, silicon, oxygen and nitrogen are located

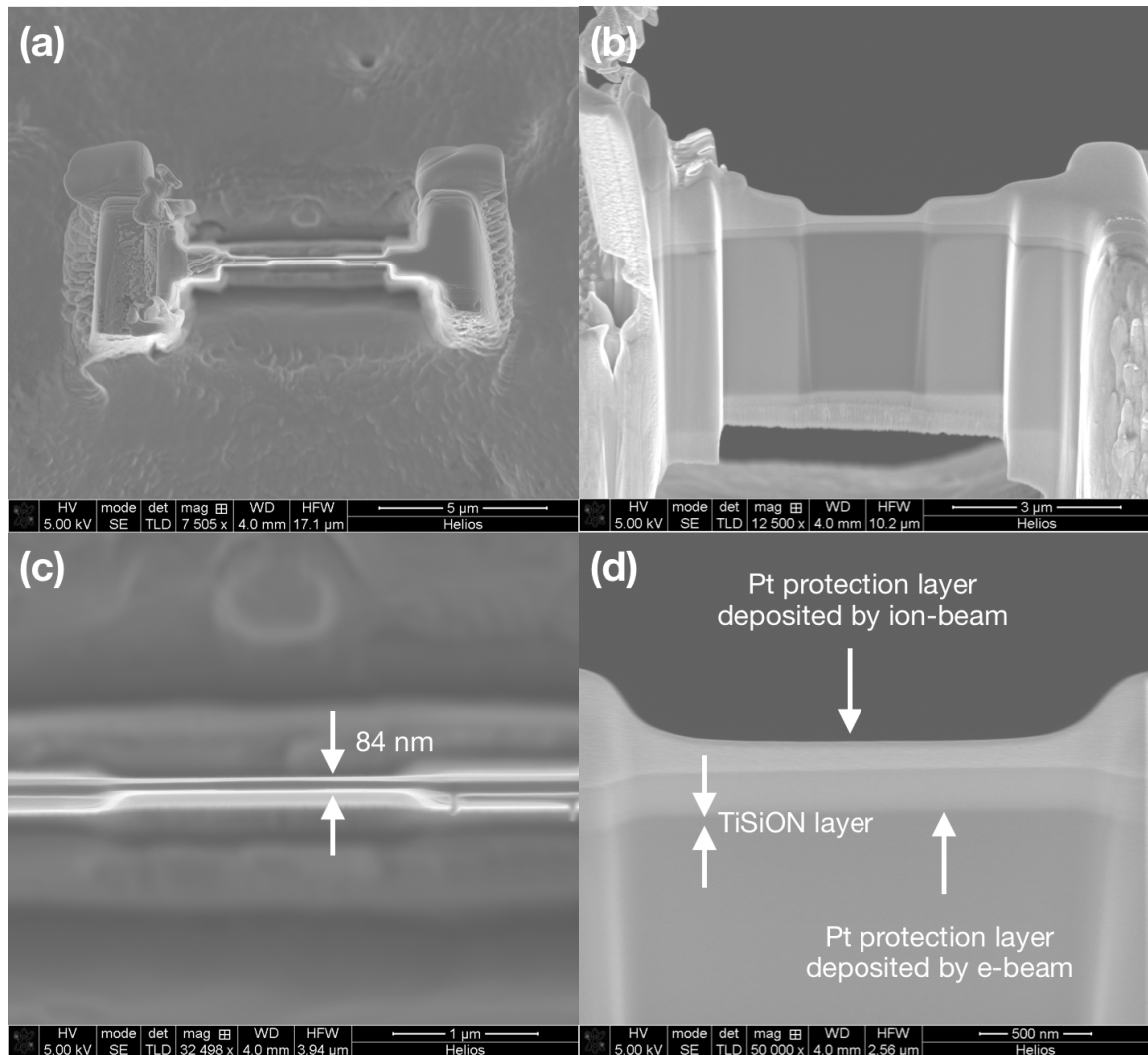


Figure 4.5: TEM lamella preparation. (a) Top view of the lamella after thinning. (b) Cross section of the TEM lamella after thinning. (c) Zoomed in top view of the lamella after thinning. The lamella thickness is smaller than 84 nm. (d) Zoomed in cross-section of the TEM lamella after thinning. The Pt protection layer is now about 100 nm thick. TiSiON is visible in the dark thin layer right under the platinum. A different composition in the oxide is present in the shallow oxide layer under TiSiON.

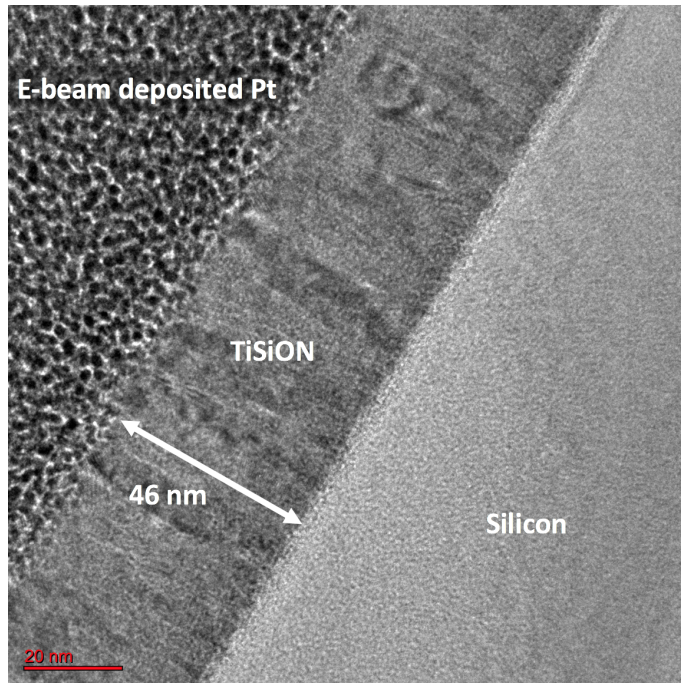


Figure 4.6: TEM image showing the e-beam deposited Pt layer, the TiSiON thin film and the silicon substrate.

at the energies reported in Table 4.1.

Element	Edge Type	Energy (eV)
Ti	L	462
Si	L	99
O	K	532
N	K	401

Table 4.1: Edge types and energies where the edges of each material are located.

For each point we scan (beam diameter smaller than 1 nm), we obtain a spectrum as reported in Figure 4.9: on the x-axis the electron energy-loss is reported, while the y-axis reports the number of electrons that have been detected with a certain energy-loss. By fitting the curve and subtracting the average counted electrons, we

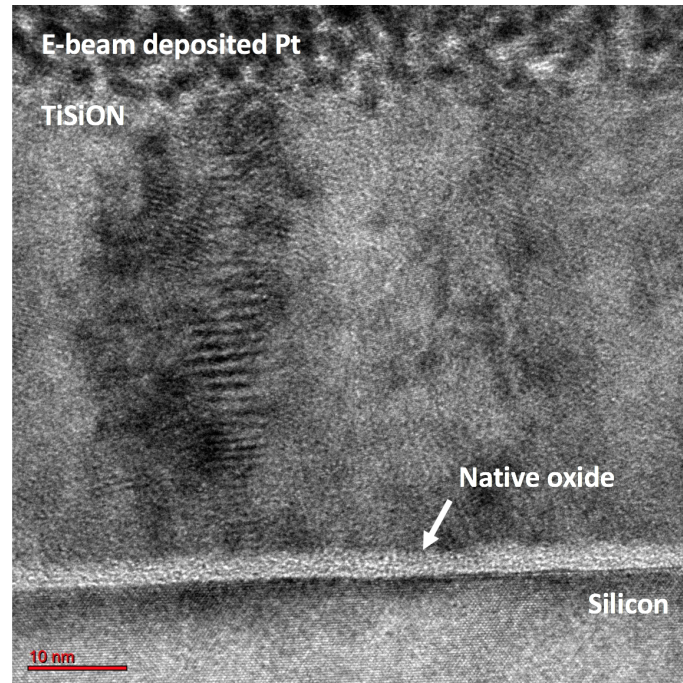


Figure 4.7: TEM image at high magnification. The silicon substrate, the native oxide, the TiSiON thin film and its interface with the platinum protective layer are visible.

can calculate the area of the obtained curve close to the edges. This way, we deduce the absolute and relative concentrations of the elements inside the thin film.

In Table 4.2 we report the results of the concentrations we obtained in different points of the film. It is clear how the dopant concentrations are inhomogeneous in different spatial locations. Oxygen concentration is usually very low, but it is present almost everywhere. Silicon has very high concentrations in limited areas of the film, whereas in a large area of the film it is not present at all. Silicon has sometimes a comparable concentration with the nitrogen one. This analysis was carried out along hundreds of nanometers, which means this inhomogeneity can lead to different optical properties in different regions of the sample. The optical properties we obtain from

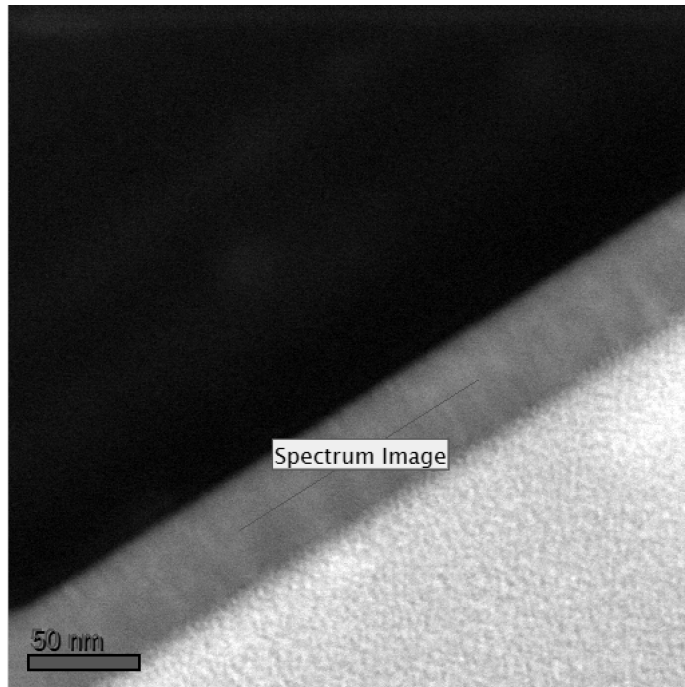


Figure 4.8: EELS line scan along the TiSiON thin film.

an ellipsometric analysis are an average over a large area of the sample. Nevertheless, since we are fabricating very small nanoantennas, the elemental inhomogeneity could be an issue. If the material properties in the proximity of the tip change, each tip could have a different behavior. Since the nanoantenna response is strongly dependent on the tip properties, its optical performances can slightly vary depending on each element concentration in the small region surrounding its tip.

4.3 Material etch study: etchants comparison

Since TiSiON is a material coming from the doping of titanium nitride with silicon and oxygen atoms, we started our investigation on different etchants considering the ones that are already present in literature for the etching of TiN. Table 4.3 reports

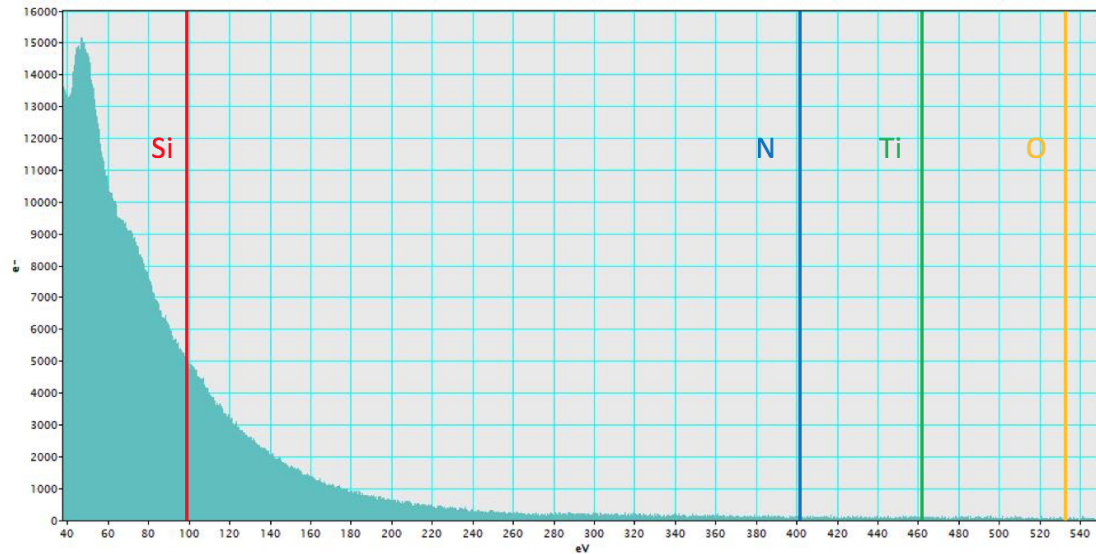


Figure 4.9: EELS spectrum. The energy for the location of the edges for TiSiON are highlighted.

Point	Ti (%)	Si (%)	O (%)	N (%)
1	34.3	0	4.2	61.5
2	45.7	0	0	54.3
3	47	0	9.4	43.6
4	68.5	5.7	7.2	18.6
5	46.5	26.7	3.5	23.3
6	45.2	23.5	2.1	29.2

Table 4.2: Relative concentrations of the elements in six different spatial points.

different etchants and recipes used to etch titanium nitride, with the relative etch rates. It is important to notice that all the plasma used in these recipes are based on helicon or inductively coupled plasmas, except for the CF_4/O_2 one.

Ar/ CHF_3 and Ar/ BCl_3 plasmas have been excluded, because the taper angles of the etched walls result to be of 70° and 45° , respectively [45], whereas we want to get very steep walls since we want to achieve extremely narrow gaps. Our investigation

	Ar/CHF ₃ [45]	Ar/Cl ₂ [45]	Ar/BCl ₃ [45]	Cl ₂ [46]	Cl ₂ /Ar/N ₂ [47]	CF ₄ /O ₂ [48]	SF ₆ /Ar [49]
Etch rate (nm/min)	10	188	30	450	66	14	150
Pressure (mTorr)	8	8	8	5	5	10	2.5
Temperature lower electrode (°C)	85	85	85	70	-20	70	5
Power upper electrode - source (W)	1000	1000	1000	1900	225		1700
Power lower electrode - bias (W)	85	85	85	40	16		60
Power density (W/cm ²)						0.2	
Voltage (V)						150	
Gas flow (sccm)	84:36	84:36	84:36	70	5:5:5	9:1	20:2

Table 4.3: Etchants and recipes to etch TiN with relative etch rates.

has mainly focused on chlorine, CF₄/O₂ and CF₄ plasmas. Chlorine is the plasma that has the highest etch rate with titanium nitride, while CF₄/O₂ is the plasma which usually attacks all the materials that don't get etched by chlorine based plasmas. CF₄/O₂ plasma achieves different etch rates depending on the relative gas concentrations. It is due to two concurrent processes. The first one is the oxidation of the superficial layer due to the presence of oxygen in the plasma. The oxidation can cause a change in the stoichiometry of the surface, leading to a different chemical interaction and, thus, a different etch rate. The second process happening due to the presence of oxygen in plasma is the variation of the fluorine concentration. A chemical reaction is triggered between CF₄ and oxygen, which makes the concentration of F atoms increase. The peak of the F atoms concentration is registered for O₂ concentrations equal to the 25% of the whole amount of gases in the chamber [50]. For these reasons, it is worth investigating what happens in the etching process if we completely remove the oxygen from the plasma. In the following paragraphs, the etching results of the three plasmas will be shown. Some etchants used during wet etching procedures will also be analyzed, since they could be used during in the next steps of the nanofabrication. Every thickness measurement has been performed with ellipsometry. In order to be able to use the ellipsometry, the etch tests have been carried out on films deposited on silicon, since glass is transparent and gives some issues with the thickness measurements through ellipsometry. Regardless, the final

devices will be fabricated on glass, as we desire a transparent substrate.

4.3.1 CF_4/O_2 plasma

CF_4/O_2 is the first plasma we have investigated. We started studying the etching of the film as deposited. Before etching, we performed an O_2 plasma ashing procedure at 50 W for 60 s to clean the sample. Then, following the recipe reported in Table 4.3, we performed the etching with the following parameters:

- Power: 100 W - 200 W
- Pressure: 10 mTorr
- Gas concentrations: $\text{CF}_4:\text{O}_2$ 9:1 sccm

With these parameters, the DC voltage measured during the etching with 100 W and 200 W is about 270 V and 430 V, respectively. After each minute of etching, we measured the thickness of the film with the ellipsometer. Figure 4.10 shows the trend of the film thickness in time. In the first minute of etching, the etched thickness is larger than the following steps. The oxidation of the surface after the sputtering of the film has been performed has changed the composition of the material and thus its etch speed is different. Furthermore, the oxygen plasma ashing might have even increased the oxidized region. After the first step, all the others are consistent. We calculate the etch rate of the material neglecting the first step, since the oxidized layer gets etched faster. For this kind of film, the etch rates with the used conditions at 100 W and 200 W result to be of 5.1 nm/min and 9.4 nm/min, respectively.

The same procedures have been applied to the etching of the annealed film as well. Figure 4.11 shows the etching of the annealed film using a power of both 100 W

and 200 W. In this case we didn't perform the oxygen plasma ashing before etching, in order to limit the oxidation of the surface. The etch rates for 100 W and 200 W are of 4.6 nm/min and 8.2 nm/min, respectively. The etch rate are pretty consistent with the ones calculated for the film as deposited. For the annealed film, they are a bit smaller, but it could be due either to the annealing of the film or to the belonging to different batches.

4.3.2 CF_4 plasma

As we said in the introduction to Chapter 4, it is worth studying the behavior of a CF_4 plasma without the presence of oxygen. We studied the etch rate of the film as deposited with the following etching parameters:

- Power: 100 W - 200 W
- Pressure: 10 mTorr
- Gas concentration: CF_4 15 sccm

As result, the etch rates with 100 W and 200 W are equal to 4.3 nm/min and 9.2 nm/min, respectively. These values are a bit lower than the ones obtained with CF_4/O_2 plasma. It is in agreement with what we know about the addition of oxygen to CF_4 in a dry plasma etching.

4.3.3 Cl_2 plasma

Another dry plasma we have investigated is Cl_2 plasma. Cl_2 plasma achieves the highest etch rate with titanium nitride [46]. Since the etch rate on TiN is around hundreds of nanometers, we tuned the etching parameters in order to achieve an

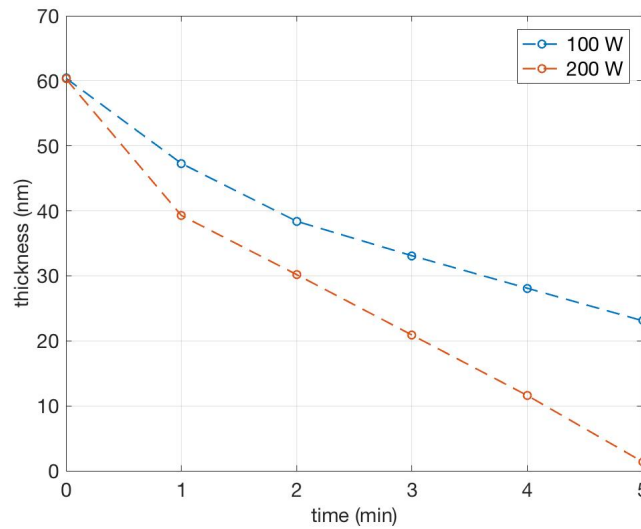


Figure 4.10: Thickness (nm) versus time (min) of the etching of as deposited TiSiON with $\text{CF}_4:\text{O}_2$ 9:1 sccm, at 10 mTorr. Both powers of 100 W and 200 W are shown.

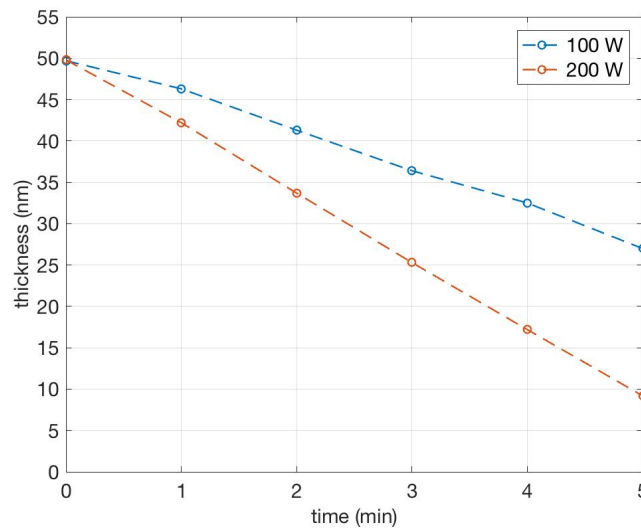


Figure 4.11: Thickness (nm) versus time (min) of the etching of annealed TiSiON with $\text{CF}_4:\text{O}_2$ 9:1 sccm, at 10 mTorr. Both powers of 100 W and 200 W are shown.

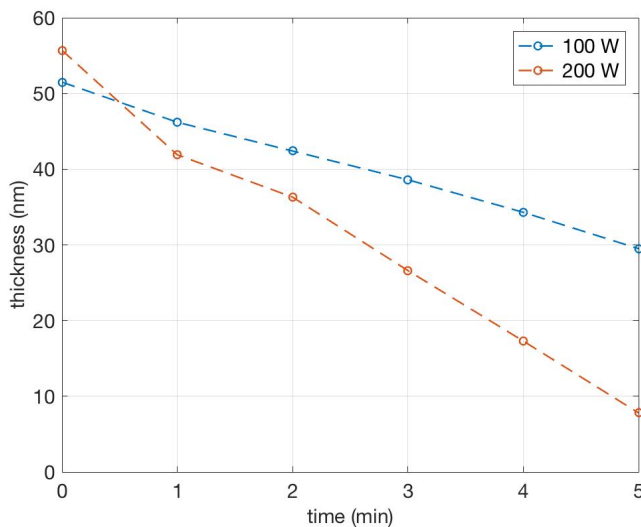


Figure 4.12: Thickness (nm) versus time (min) of the etching of as deposited TiSiON with CF_4 15 sccm, at 10 mTorr. Both powers of 100 W and 200 W are shown.

etch rate that could be measured. A high operating pressure reduces the etch rate but, at the same time, the directionality of the etching gets affected. A low gas concentration reduces the etch rate as well. For this reason, we started the etching with the following parameters:

- Power: 100 W
- Pressure: 20 mTorr
- Gas concentration: Cl_2 10 sccm

The etched thickness is a few nanometers. Thus, we decreased the pressure to 10 mTorr, in order to get a higher etch rate and a better directionality, ideally. The second step didn't bring any change to the film thickness. So as a last try, we raised the pressure back to 20 mTorr and we increased both the chlorine concentration to 20 sccm and the power to 150 W. No variation happened to the thickness for

the second time. Thus, we determined that chlorine plasma does not etch TiSiON. The superficial layer was etched because of its different stoichiometry due to the oxidation, but, as soon as we removed that layer, the etching stops. We presume this behavior is due to the presence of silicon and oxygen atoms in the lattice of the film. While chlorine is a good etchant for TiN, it is not an effective etchant for SiO₂. This issue could be solved by adding Ar into the gas flow in order to introduce a ballistic contribution to the etching process. However, the ballistic contribution could reduce the sidewall steepness of the etched profile.

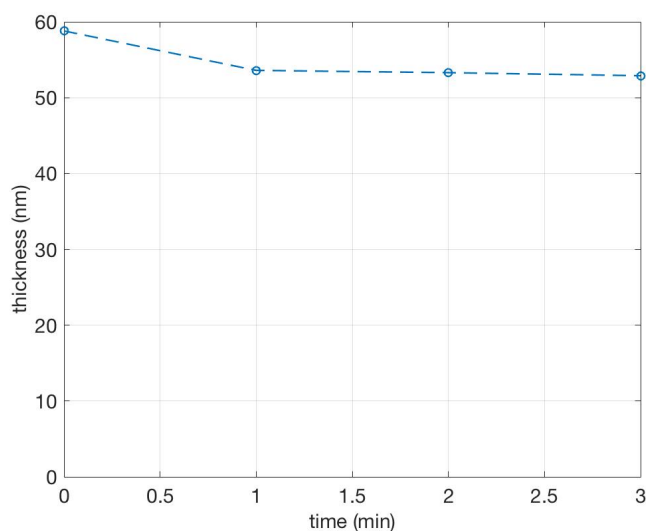


Figure 4.13: Thickness (nm) versus time (min) of the etching of as deposited TiSiON with Cl₂ plasma. Different parameters were used for each point. First step: 100 W, 10 sccm, 20 mTorr. Second step: 100 W, 10 sccm, 10 mTorr. Third step: 150 W, 20 sccm, 20 mTorr.

4.3.4 Other etchants for wet etching procedures

During our investigation, we also studied some etchants used for the wet etching of materials that can be used as hard masks for the patterning of nanostructures, as

we will see in Section 4.4. Basically, none of the tested etchants effectively removed TiSiON. Most of them only remove the superficial oxidized layer, as we have seen in the previous paragraphs. This gives us freedom in the choice of a suitable hard mask.

Etchant	Etch rate (nm/min)
BOE HF 7:1	0.2
Aluminum etch	not working
Cr-7 etch	not working
MF CD-26	not working
TMAH	not working

Table 4.4: Etchants used in wet etching procedures and etch rate on TiSiON.

4.4 Investigation of hard masks for patterning nanostructures of TiSiON

In this section, we will focus on the use of different materials as hard masks for the patterning of TiSiON nanostructures. The process we follow is shown in Figure 4.14. It starts with spinning the resist (i.e. PMMA in our case) on the sample and its exposure by electron beam lithography (see Figure 4.14(a-b)). We develop the resist and we will get a structure similar to the one reported in Figure 4.14(c). The process continues with the Physical Vapour Deposition of the metal we want to use as hard mask on the patterned sample (see Figure 4.14(d)). Thus, we perform the lift-off of the resist, in order to obtain on the metal a negative image of the one we had patterned on the PMMA (see Figure 4.14(e)). Now we can etch the TiSiON film by dry reactive ion etching. If the metal we are using is a good hard mask, we will obtain a profile as the one shown in Figure 4.14(f)). Finally, we can remove the

metal with a suitable wet etchant depending on the material. The final pattern we want to obtain is shown in Figure 4.14(g).

Now we will go through different metals and we will analyze their behavior in response to the two plasmas we have seen to be working in Section 4.3: CF_4/O_2 and CF_4 . In particular we will try both plasmas on the samples, starting with the etching parameters reported in Table 4.5. After each etching step, we allow the sample to cool down for several minutes, otherwise the profile's shape could be affected by the overheating of the substrate. The higher the power, the higher the heating. This is the reason why we wait for a longer time with CF_4 plasma at 200 W. If one of the two plasma works properly with these parameters, we investigate what happens with the other power we haven't used, that is to say 200 W for CF_4/O_2 and 100 W for CF_4 . This way, we properly characterize how the hard masks react with the different plasmas using different powers.

	CF_4/O_2	CF_4
Power (W)	100	200
Pressure (mTorr)	10	10
Gas concentration (sccm)	9:1	15
Time	6×2 minutes	7×1 minute
Stop after each step	3 minutes	4 minutes

Table 4.5: Etching parameters used for CF_4/O_2 and CF_4 for hard masks investigation.

For a general testing of the different plasmas and their behavior with the different hard masks, we will use a dose test that was designed for a different project we were carrying out in the group. Furthermore, since there are several devices (i.e. bow-ties, diodes and transistors), it allows us to carry out a better characterization over different types of structures. This is the recipe we will follow during our investigation on the hard masks:

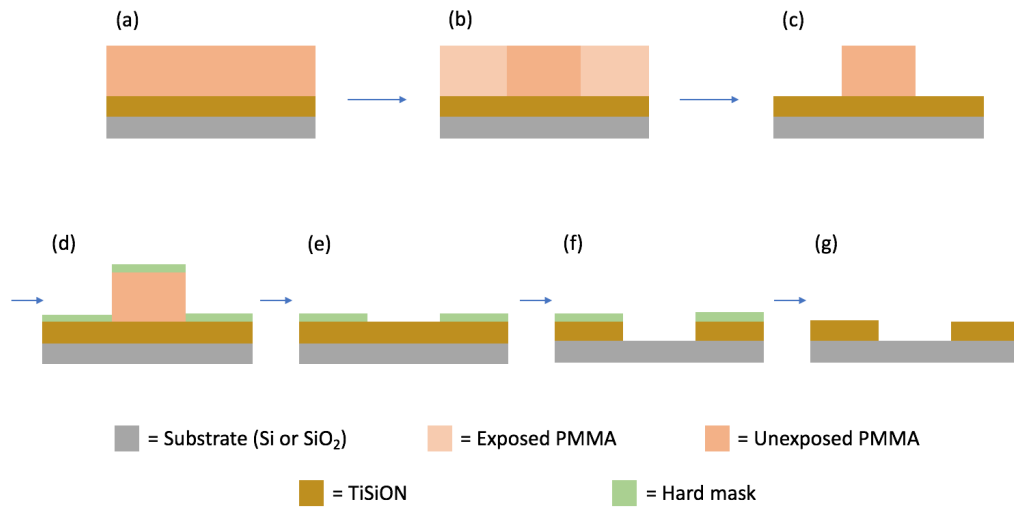


Figure 4.14: Fabrication steps for patterning nanostructures using a metal as hard mask. (a) Spin of e-beam positive resist. (b) Exposure with electron beam lithography. (c) Patterned resist after development. (d) Evaporation of the hard mask. (e) Resist lift-off. (f) Reactive ion etching of TiSiON. (g) Hard mask removal by wet etching.

- Solvent cleaning and oxygen plasma ashing at 50 W for 60 s
- Spin PMMA A2 at 2.5 krpm, bake at 180 °C for 2 minutes. PMMA spun at this speed has a thickness of about 80 nm.
- E-beam lithography with 3500/4000/4500/5000/5500/6000/6500 $\mu\text{C}/\text{cm}^2$ and a current of 2 nA
- Cold develop in 3:1 IPA:MIBK at 0 °C for 60 s
- Evaporation of 30-nm thick metal for hard mask
- PMMA lift-off in heated NMP at 60–70 °C for 1 hour
- RIE (see parameters reported in Table 4.5)

- Imaging with both conventional and tilted SEM

The materials we investigated as hard masks are aluminum, molybdenum, titanium, chromium and an aluminum/chromium bi-layer.

4.4.1 Aluminum

Aluminum and its oxides are widely used materials as hard masks both with CF_4/O_2 and SF_6 plasmas [51, 52, 53, 54]. Our study on aluminum starts with the fabrication of some structures over a SiO_2 substrate. On the same sample we fabricated four bunches of devices, then we cut it in order to carry out four different processes. Two samples were used to study aluminum, while the other two were used to study molybdenum. Since they were fabricated on the same sample and they went through the same steps before cutting before the metal evaporations, the correlation among these four samples is really high and we will image it only once before etching, assuming that all the others look the same.

Figure 4.15 shows a bow-tie structure obtained after the evaporation of the aluminum hard mask and the resist lift-off. The gap is about 37 nm wide. Exactly the same structure is shown after CF_4 plasma etching at 200 W in Figure 4.16, with a 45° tilting angle. As we can see, the profile looks rounded and the gap has become wider: it almost doubled, since the walls are not as steep as we desired. We can estimate the taper angle from the lines shown in Figure 4.17. Using the fundamental trigonometric formulas, we can calculate the taper angle as $70\text{-}75^\circ$.

Due to the insulating nature of the substrate, the sample had to be covered with several nanometers of gold, because the charging of the structures was preventing any imaging without a thin coating of a conductive layer. The Au coating made it impossible to recognize the different layers that were etched. Thus, we could not

determine how thick the aluminum layer is and we do not know if we were able to etch down to the substrate. Moreover, if we etched into the substrate, the gap between the actual electrodes would also be larger than 73 nm, which is undesirable.

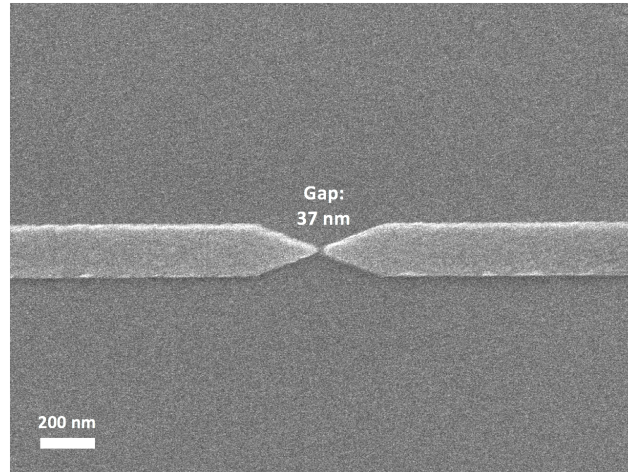


Figure 4.15: SEM image taken after 30-nm thick aluminum evaporation. Structure exposed with $3500 \mu\text{C}/\text{cm}^2$ dose. Gap dimension from design: 0 nm.

The same kind of study was carried out with CF_4/O_2 plasma at 100 W. With regard to the structures before etching, we can refer to the SEM image reported in Figure 4.15, since they were exposed together on the same sample. A bow-tie structure after etching is shown in Figure 4.18. As we can see, the profile is not as rounded as the ones we obtained with CF_4 plasma and the gap looks much more narrow. A better look at the profile can be taken from Figure 4.19. The walls are indented, but almost vertical. Also in this case we had the issue of the insulating substrate and we had to cover the sample with some nanometers of gold. Nevertheless, comparing all the SEM images we have just analyzed, we can assert CF_4/O_2 plasma works better than CF_4 plasma with an Al hard mask.

At this point, to carry out a better characterization of the CF_4/O_2 plasma, we exposed other samples on silicon substrate. This way, we can get rid of the charging

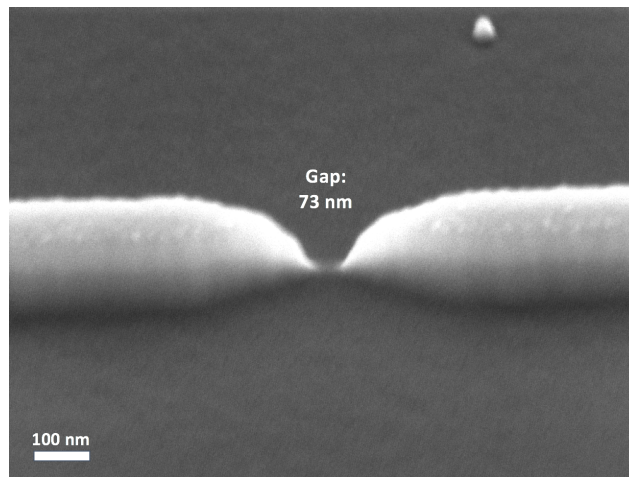


Figure 4.16: SEM image taken after CF_4 RIE at 200 W. The plasma has widened the gap. Some nanometers of gold cover the sample. Gap dimension from design: 0 nm. Dose of the exposure: $3500 \mu\text{C}/\text{cm}^2$.

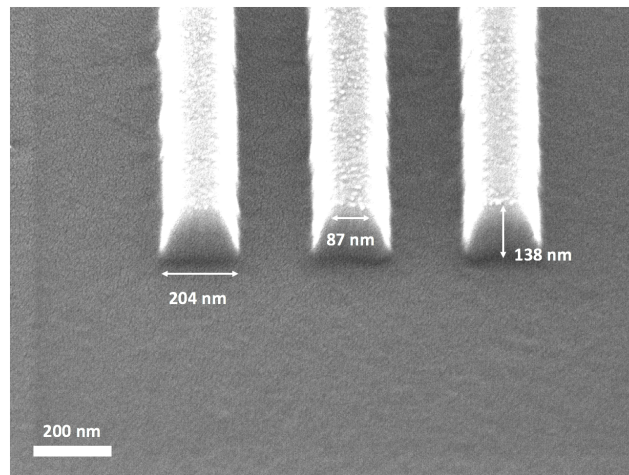


Figure 4.17: SEM image showing 200-nm wide lines after CF_4 RIE at 200 W. The walls have a taper angle of $70\text{-}75^\circ$. Some nanometers of gold cover the sample. Dose of the exposure: $3500 \mu\text{C}/\text{cm}^2$.

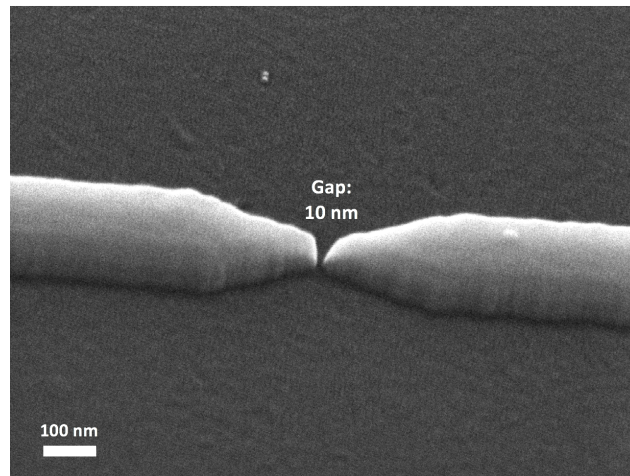


Figure 4.18: SEM image taken after CF_4/O_2 RIE at 100 W, using aluminum as hard mask. The gap is narrow and the profile are not rounded. Some nanometers of gold cover the sample. Gap dimension from design: 0 nm. Dose of the exposure: $3500 \mu\text{C}/\text{cm}^2$.

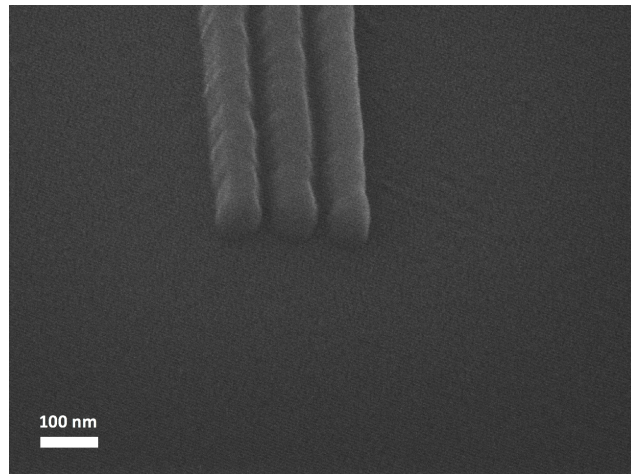


Figure 4.19: SEM image showing 50-nm wide lines after CF_4/O_2 RIE at 100 W, using aluminum as hard mask. Some nanometers of gold cover the sample. Dose of the exposure: $5000 \mu\text{C}/\text{cm}^2$.

effects and we are able to get better images of the gaps without sputtering gold.

In Figure 4.20 and Figure 4.21, we can see the same bow-tie structure before and after etching with CF_4/O_2 plasma at 100 W. We can clearly see how the gap becomes wider and how the profiles are tilted. The gap that was present in the aluminum before etching has been transferred to the bottom of the etched substrate. Now the gap is wider than before.

If we increase the power to 200 W, the sample will undergo more heating. Given a structure before etching as the one shown in Figure 4.22, we can see how the power affects our structures from Figure 4.23. The heating process widened the gap about 50 nm more than with 100 W.

In short, CF_4/O_2 plasma with 100 W was the best solution of those attempted. If we want to use aluminum as a hard mask, we need to find a way to remove it in the end of the fabrication process. We tested two different wet etching procedures: MF CD-26 and aluminum etch type A (their etch rate on TiSiON has already been showed in the end of Section 4.3). MF CD-26 is a water diluted TMAH-based developer with a concentration between 1% and 5% [55]. TMAH-based developers have an etch rate on aluminum of about 50-100 nm/min. After a 2 minutes soak in MF CD-26, the profiles looked like the one reported in Figure 4.24. We can see that some residues are still present on the surface, but the wet etching was effective. The problem could be easily solved by either performing a longer soak, or adding some agitation to the process with an ultrasound bath. The other etchant we tested to remove the aluminum hard mask, is an aluminum etch type A (Phosphoric Acid: 40-80%; Acetic Acid: 3-20%; Nitric Acid: 1-5%) with an etch rate at room temperature of $30 \text{ \AA}/\text{s}$ [56]. Figure 4.25 shows the surface of TiSiON after 1 minute soak in Al etch type A. We can see some spots on the surface. It is not easy to understand what they are, but since we want to use the final devices as optical detectors as well, it is

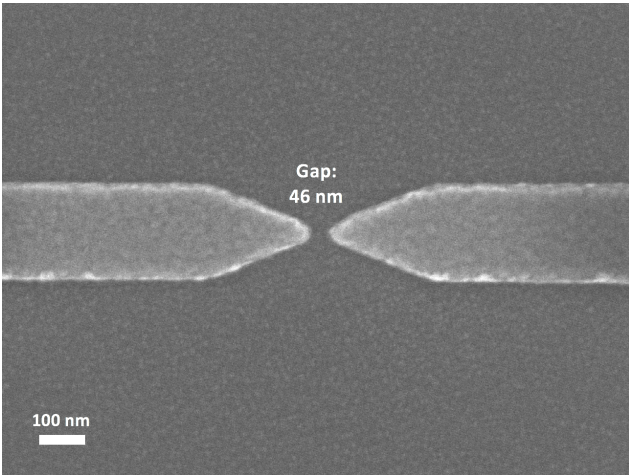


Figure 4.20: SEM image taken before etching. Gap dimension from design: 0 nm. Dose of the exposure: 3500 $\mu\text{C}/\text{cm}^2$.

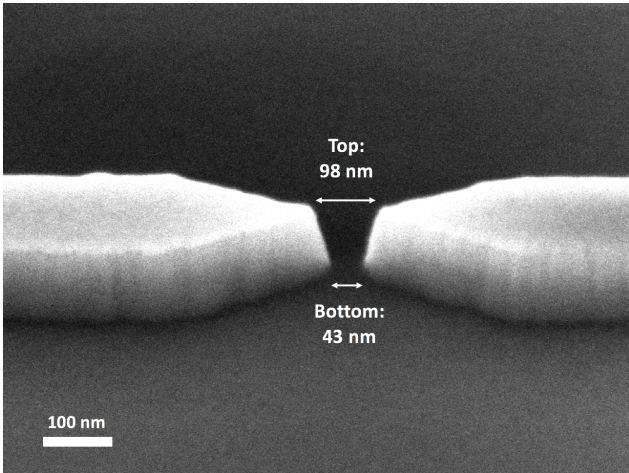


Figure 4.21: SEM image after CF_4/O_2 RIE at 100 W, using aluminum as hard mask. Gap dimension from design: 0 nm. Dose of the exposure: 3500 $\mu\text{C}/\text{cm}^2$.

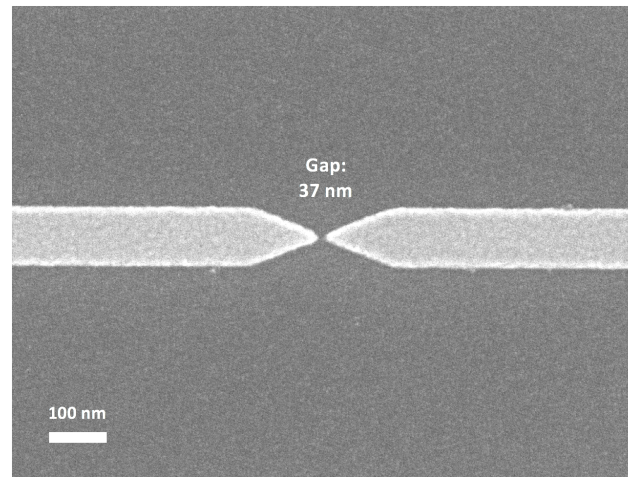


Figure 4.22: SEM image taken before etching. Gap dimension from design: 0 nm. Dose of the exposure: $3500 \mu\text{C}/\text{cm}^2$.

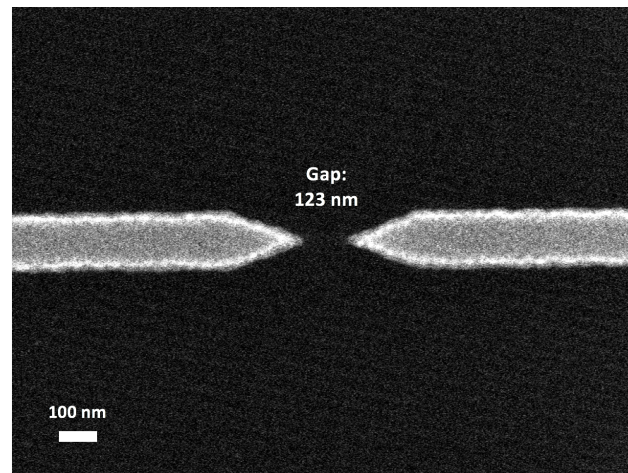


Figure 4.23: SEM image after CF_4/O_2 RIE at 200 W, using aluminum as hard mask. Gap dimension from design: 0 nm. Dose of the exposure: $3500 \mu\text{C}/\text{cm}^2$.

preferable to get a smooth surface so as to not perturb the surface properties.

4.4.2 Molybdenum

Molybdenum is another metal we want to investigate in its use as a hard mask [57]. For molybdenum, the structures were patterned on glass, on the same sample as the first structures we investigated for aluminum in subsection 4.4.1. Since glass is amorphous, many structures were lost during the cut of the sample, so we weren't able to evaluate any bow-ties with molybdenum. We were still able to qualitatively evaluate the CF_4/O_2 and CF_4 plasmas.

Figure 4.26 shows the same structure etched with CF_4 (see Figure 4.26a) and CF_4/O_2 dry etching (see Figure 4.26b). We can see how the CF_4/O_2 plasma has destroyed part of the structure, whereas it is still there after CF_4 etching. The profiles look a bit rough in both cases.

Figure 4.27 shows 50-nm wide lines etched with CF_4 (see Figure 4.27a) and CF_4/O_2 dry etching (see Figure 4.27b). Also in this case, the lines etched with CF_4/O_2 plasma result to be destroyed and damaged. The ones etched with CF_4 are not destroyed, but the profiles are not steep. It would be difficult to realize very small gaps with such a taper angle.

4.4.3 Titanium

Titanium is the third metal we tried to use as a hard mask during our study. The hard mask was etched during the dry etching procedures, both using CF_4 and CF_4/O_2 plasmas. Figure 4.28 shows the results obtained after dry etching with CF_4 plasma at 200 W (see Figure 4.28a) and CF_4/O_2 plasma at 100 W (see Figure 4.28b). Furthermore, since the thickness of the features was very thin, it was impossible to

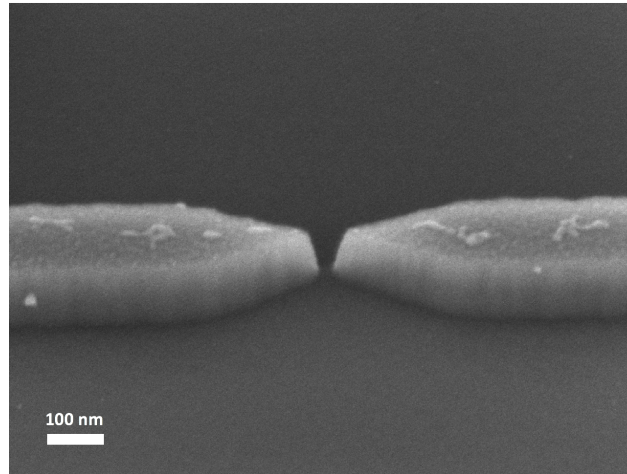


Figure 4.24: SEM image showing a bow-tie structure after 2 minutes of MF CD-26 soak.

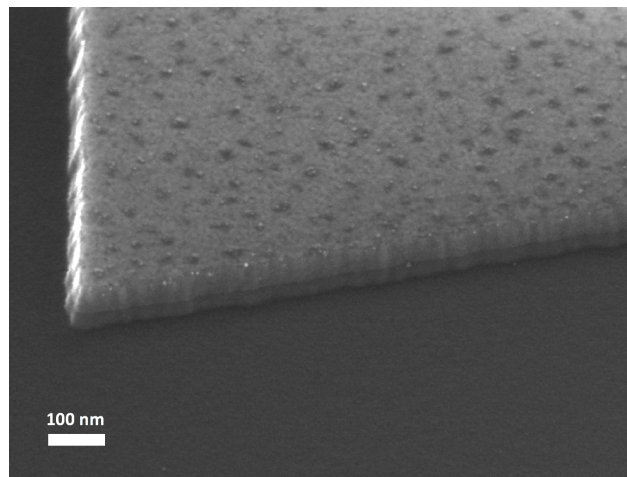
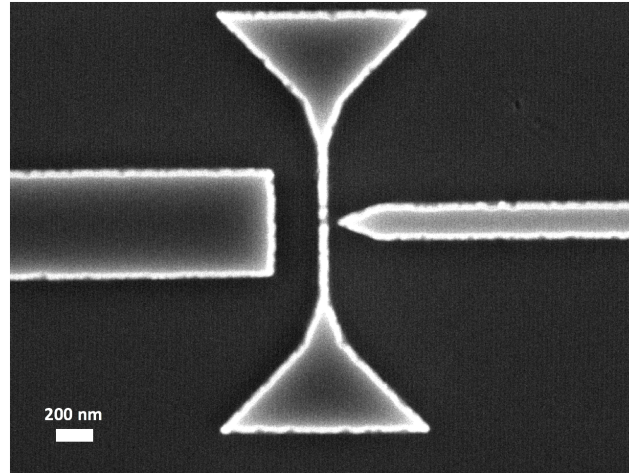
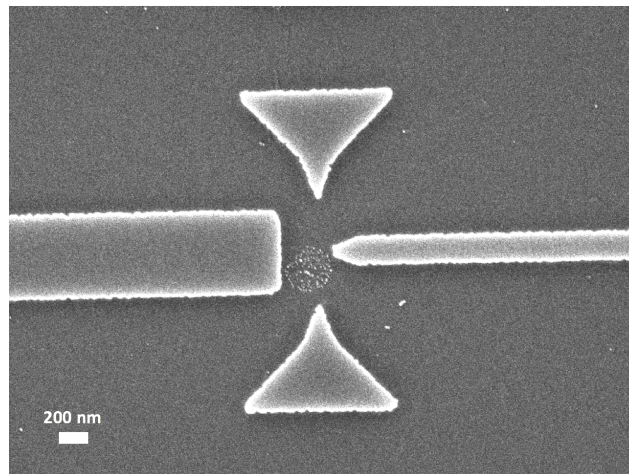


Figure 4.25: SEM image showing TiSiON after 1 minute of Al etch type A soak.

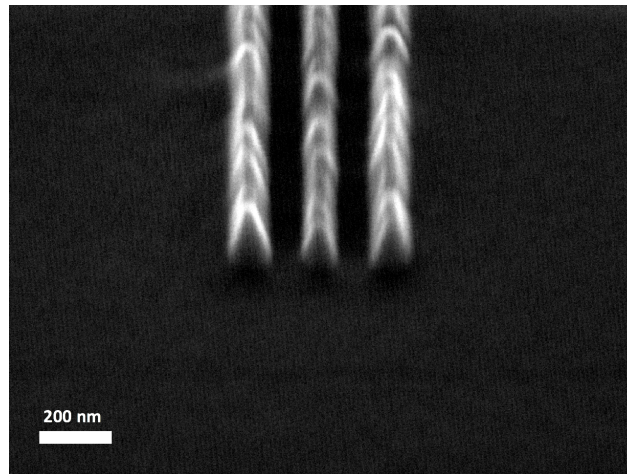


(a) SEM image after CF_4 RIE at 200 W.

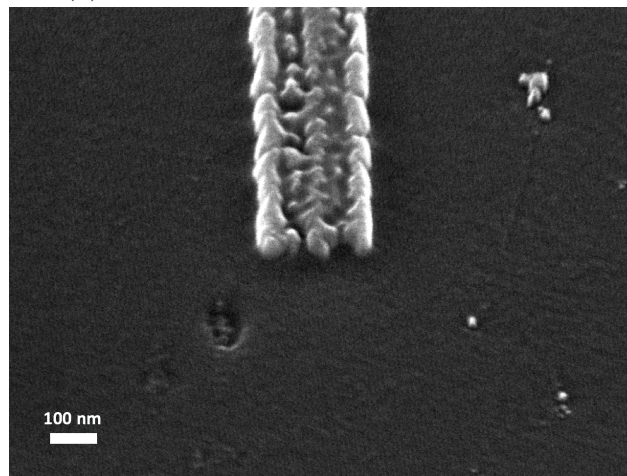


(b) SEM image after CF_4/O_2 RIE at 100 W.

Figure 4.26: Comparison of a structure etched with CF_4 and CF_4/O_2 plasmas, using molybdenum as hard mask. The structures were fabricated on the same sample and went through the same processes, except for the dry etching. The correlation is very high.



(a) SEM image after CF_4 RIE at 200 W.



(b) SEM image after CF_4/O_2 RIE at 100 W.

Figure 4.27: Comparison of etched lines with CF_4 and CF_4/O_2 plasmas, using molybdenum as hard mask. The lines were fabricated on the same sample and went through the same processes, except for the dry etching. The correlation is very high.

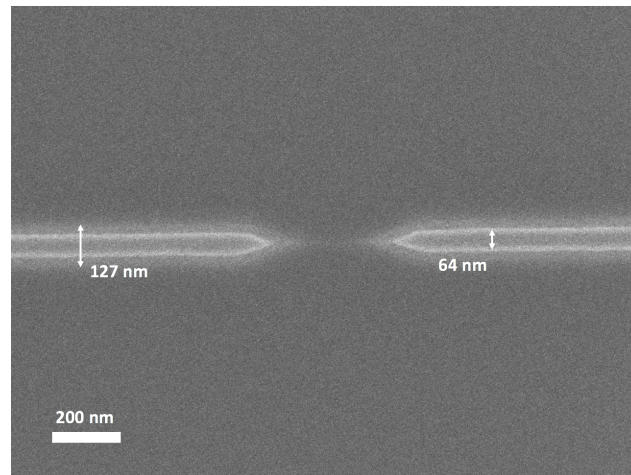
get a good contrast for a 45° tilted image.

4.4.4 Chromium

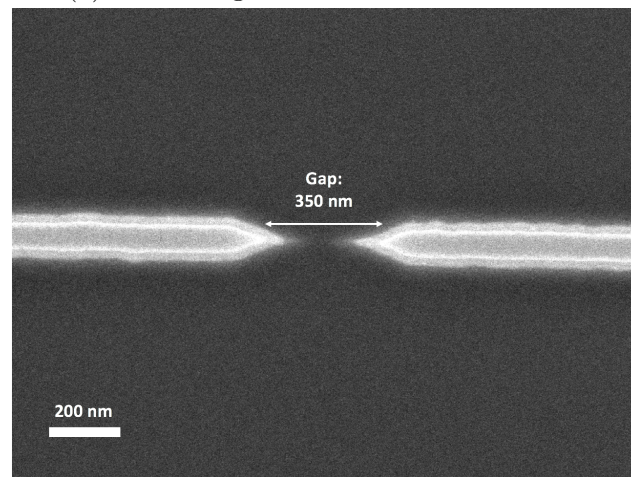
Chromium is a material that is widely used as hard mask, both in micro- and nanofabrication [58, 59, 60, 61]. After CF_4 plasma etching at 200 W, many structures came out connected, perhaps due to the increase in the temperature due to the high power. Figure 4.29 shows both a bow-tie structure (see Figure 4.29a) and a bunch of lines that were exposed with a dose of $3500 \mu\text{C}/\text{cm}^2$ (see Figure 4.29b) after etching. As we can see from Figure 4.29b, the smallest lines got all connected, even if the dose was low. Furthermore, the larger lines are spreading, and the trenches between them are getting narrow.

For the CF_4/O_2 plasma, we tried etching at both 100 W and 200 W. We got a very good result in both cases, as shown in Figure 4.30. The profiles are very steep, and narrow gaps were obtained. We will stick to 100 W just to avoid an overheating of the sample, which could damage the structures anyway.

Chromium, just like titanium, is a material that is widely used as adhesion layer in fabrication processes. Nevertheless, chromium is a very difficult material to remove, both due to its outstanding adhesion and its property of diffusing for some nanometers into the material it is in contact with [63]. We tried to remove the chromium hard mask with a Cr-7 etch (based on perchloric acid 7%) for 3 minutes. Its etch rate for a wet etching soak is of $24 \text{ \AA}/\text{s}$ [62]. Figure 4.31 shows the result of the wet etching. As we can see, the chromium hard mask is still there: the Cr-7 etch was completely ineffective. It could be due to a change in the stoichiometry of the hard mask after the diffusion mechanisms that may have happened with TiSiON. It is also possible that the etchant was not suitable to etch a chromium thin layer.

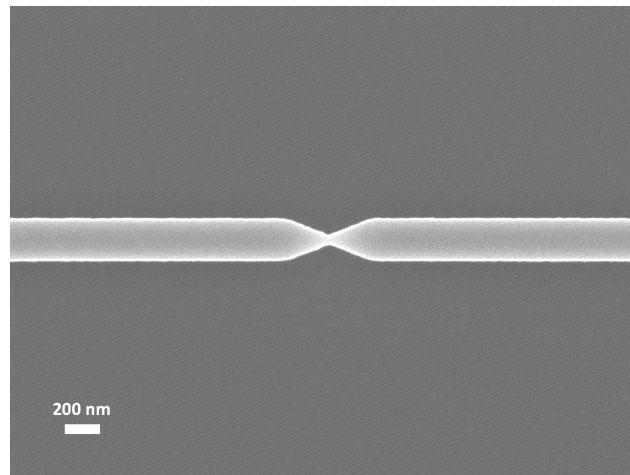


(a) SEM image after CF_4 RIE at 200 W.

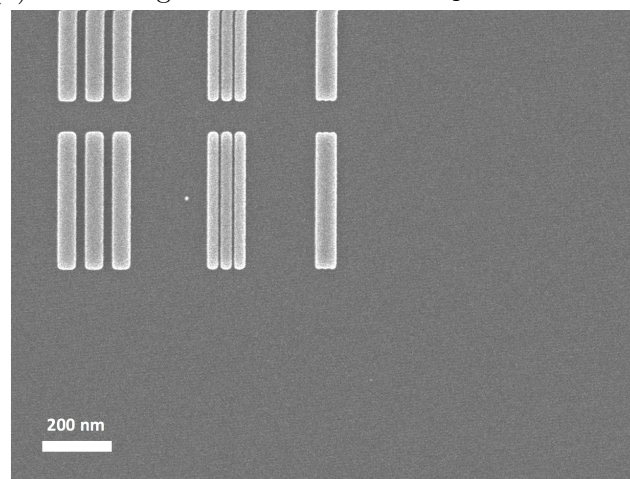


(b) SEM image after CF_4/O_2 RIE at 100 W.

Figure 4.28: Bowties etched with CF_4 and CF_4/O_2 plasmas, using titanium as hard mask.

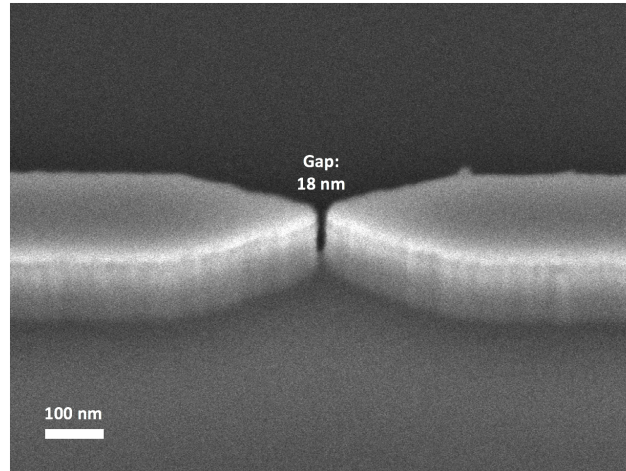


(a) SEM image of bow-ties after CF_4 RIE at 200 W.

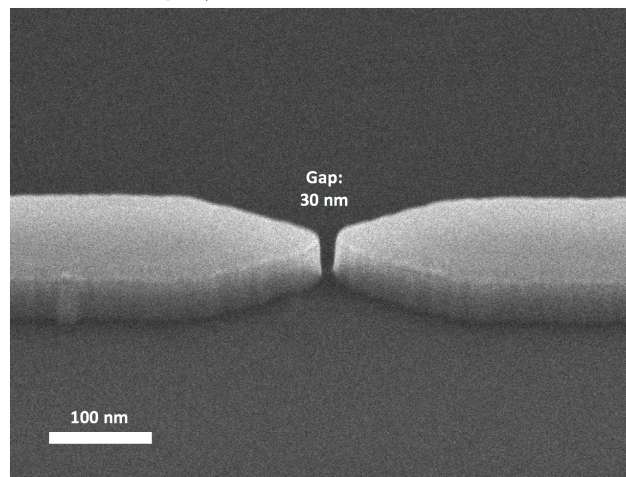


(b) SEM image of lines after CF_4 RIE at 200 W.

Figure 4.29: Bowties and lines etched with CF_4 plasma at 200 W, using chromium as hard mask.



(a) SEM image of bow-ties after CF_4/O_2 RIE at 100 W. Gap dimension from design: 0 nm. Dose of the exposure: $5000 \mu\text{C}/\text{cm}^2$.



(b) SEM image of lines after CF_4/O_2 RIE at 200 W. Gap dimension from design: 30 nm. Dose of the exposure: $6000 \mu\text{C}/\text{cm}^2$.

Figure 4.30: Bowties etched with CF_4/O_2 plasma at both 100 W and 200 W, using chromium as hard mask.

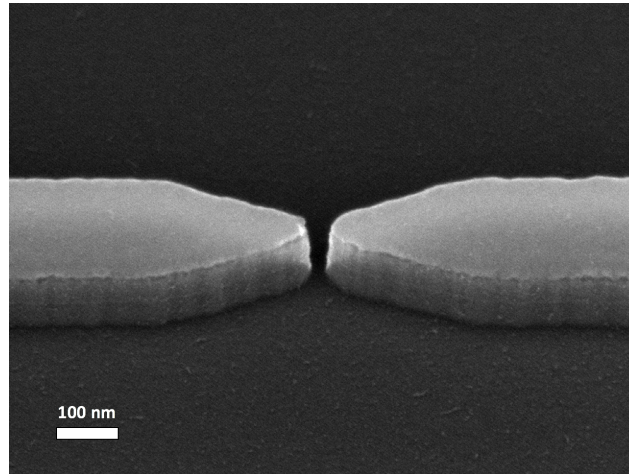


Figure 4.31: SEM image showing bow-ties fabricated with a chromium hard mask after 3 minutes of Cr-7 etch soak. The chromium thin layer was not removed.

4.4.5 Aluminum/Chromium bi-layer

As we have seen in subsection 4.4.4, chromium is a very good hard mask if we want to obtain high aspect ratio features, but it is impossible to remove through wet etching procedures. Since we are interested in the surface properties of TiSiON, we do need to find a way to remove the chromium hard mask. Thus, we tried to transform the removal process into a lift-off process. In particular, if we fabricate a bi-layer structure, chromium would not contact the TiSiON, preventing its diffusion into our material and the consequent surface modification. At the same time, if we properly choose the intermediate layer, we just need to find a way to remove it, transferring the removal issue from Cr to another material.

Since we already saw that aluminum is relatively easy to remove (see subsection 4.4.1), we decided to use it as intermediate layer. Our first attempt was to deposit 15 nm Al and 15 nm Cr. After etching with CF_4/O_2 plasma at 100 W, the performances we have seen with chromium in subsection 4.4.4 are maintained (see

Figure 4.32).

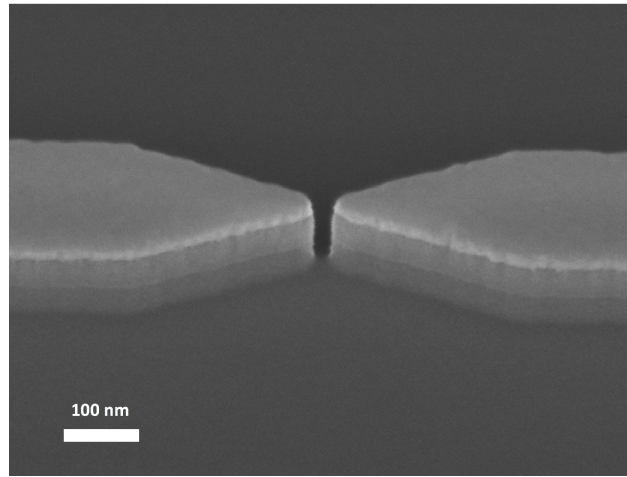
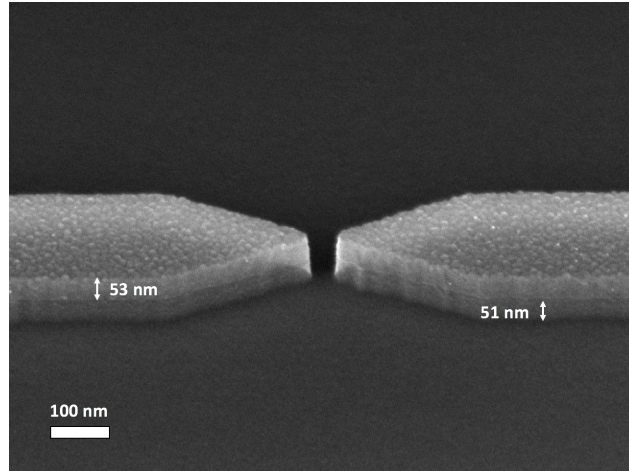


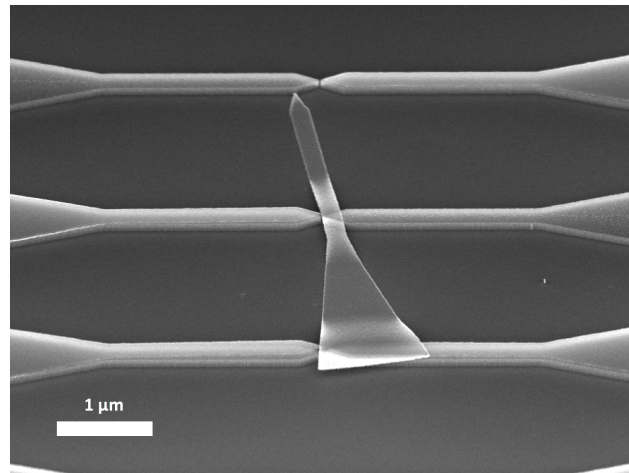
Figure 4.32: SEM image showing bow-ties fabricated with 15-nm thick aluminum and 15-nm thick chromium bi-layer hard mask after CF_4/O_2 RIE at 100 W. The overetched thickness into the silicon substrate is well-defined.

To perform the lift-off process, we have to remove the aluminum layer, and the chromium will get removed as well. In order to enhance the etch rate of the aluminum, we performed a 3 minutes soak in pure TMAH. The results are shown in Figure 4.33. We can see that TMAH is a good solution, because it doesn't leave residues on the structures after the lift-off. Nevertheless, since it is a very viscous base, the sample wasn't provided with a sufficient agitation, so many structures still have the hard mask on top, and, in some cases, the chromium redeposited on the structures.

To make sure we lift-off the Al-Cr bi-layer, we increased the aluminum thickness to 20 nm and we performed the sonication in an ultrasound bath for 15 minutes. This time, the lift-off worked and Figure 4.34 shows the final structure we obtain through the fabrication process we developed.



(a) SEM image of bow-ties after wet etching in TMAH. The hard mask has been removed.



(b) SEM image of structures after wet etching in TMAH. The hard mask has been removed from some structures, others are starting lifting off, and there are some chromium structures redepositing.

Figure 4.33: Structures after a 3 minutes long wet etching in pure TMAH. The lift-off worked with some structures, while the mask still has to lift-off on others.

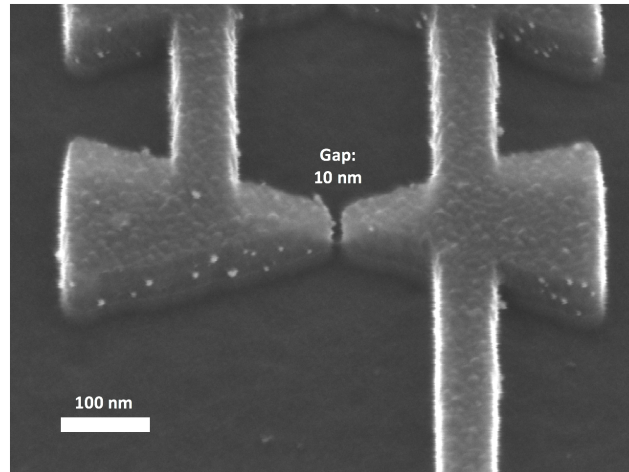


Figure 4.34: SEM image of a bow-tie structure with wires after 15 minutes soak in TMAH in an ultrasonic bath.

4.5 Bow-ties arrays patterning and pads fabrication

After developing the process we have seen in Sections 4.3 and 4.4, we wanted to fabricate different bow-tie arrays and connect them to gold pads in order to test them both electrically and optically. The process flow for the fabrication of the pads is shown in Figure 4.35. This process starts after the fabrication of the bow-ties arrays, with the removal of the hard mask. The full recipe we follow is:

- Spin PMGI SF-9 at 4.5 krpm, bake at 180 °C for 90 s
- Spin S1813 at 4.5 krpm, bake at 100 °C for 90 s
- Direct Writing Laser exposure with 10 W, 35%
- Develop in MF CD-26 for 80 s, then soak in DI water for 1 minute
- Evaporate 50 nm Ti + 250 nm Au
- Lift-off in acetone for 15 minutes, then sonicate for 1 minute

- Soak in MF CD-26 for 2 minutes, then soak in DI water for 1 minute
- Solvent cleaning

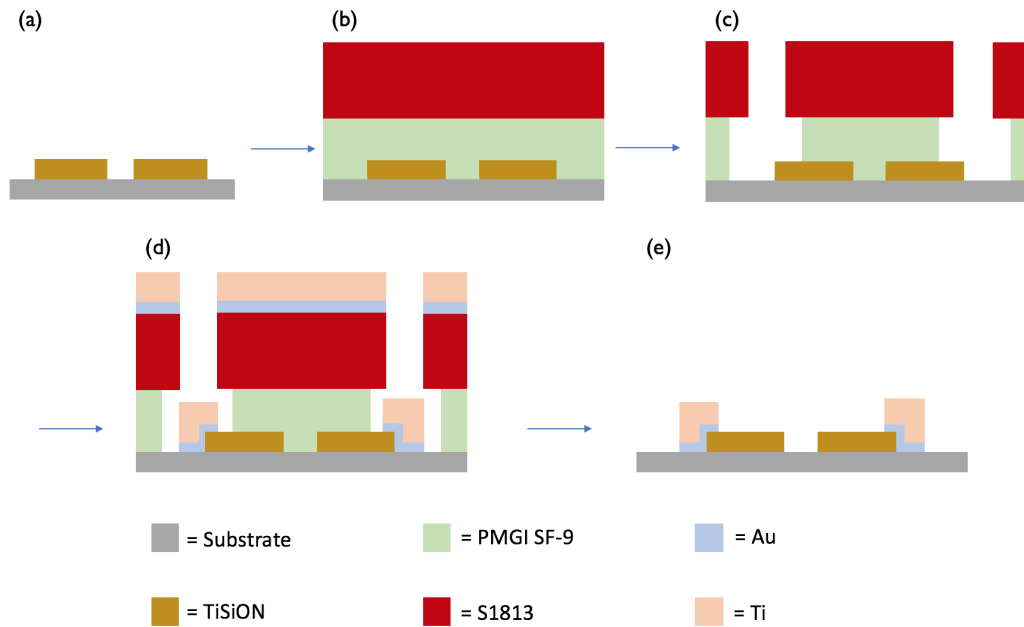


Figure 4.35: Process flow for pads fabrication. (a) Sample after hard mask removal from the previous step. (b) Spin a resist bi-layer: PMGI SF-9 and S1813. (c) Exposure with DWL and develop. (d) Evaporation of the pads: 50 nm Ti and 250 nm gold. (e) Resist bi-layer lift-off.

It is important to note that the process we use to fabricate the pads involves two different resists. The first one is PMGI SF-9, whose thickness when spun at 4.5 krpm is about 500 nm [64]. It is used as intermediate layer. The second resist is S1813, which is the one that is used as imaging resist to expose with the laser. Its thickness when spun at 4.5krpm is about 1.4 μm [65]. When we expose the sample with DWL, we are just exposing the top layer. When we develop with MF CD-26, the exposed S1813 gets developed and is dissolved. In the meantime, MF CD-26 attacks the

underlying PMGI SF-9 layer, creating an undercut under the not exposed S1813. This way, we manage to evaporate titanium and gold with a very high resolution, and the lift-off procedure will be safer. After lifting-off the S1813 using acetone, we need to add an additional step to remove PMGI SF-9. This is the reason why we soak the sample in MF CD-26 just before the end of the process.

The final layout we developed for our process is shown in Figure 4.36. The layout was scripted with Python and then transferred to LayoutEditor. We designed eight different sets of six arrays, paired in two groups of four arrays. In each group, we exposed the arrays with four different doses (4500/5000/5500/6000 $\mu\text{C}/\text{cm}^2$). In the first four rows, a study on the altitude will be carried out: for each dose we fabricate bow-ties with six different altitudes (from 200 nm to 300 nm, with steps of 20 nm). On the other hand, in the last four rows, we will carry out two different studies: for each dose, the left column is thought to fabricate bow-ties with three different base/altitude ratios (0.5, 0.75 and 1), whereas in the right column we find three different widths of the wires (40 nm, 80 nm and 120 nm). The gap dimensions will be set by the dose, while by layout they are designed as 0 nm. Every bow-ties array is $25\ \mu\text{m} \times 25\ \mu\text{m}$ large, containing 2016 bow-ties.

We fabricated four samples in parallel: two with TiSiON as deposited (one on silicon and one on glass), two with annealed TiSiON (one on silicon and one on glass). Since the arrays are very dense, we used PEC to correct the dose during the exposure with electron beam lithography (see subsection 3.1.1). This way, the differences between the two substrates should be taken into account and the dose should be adjusted properly. Figure 4.37 shows an SEM image of a fabricated bow-ties array made of TiSiON as deposited on silicon.

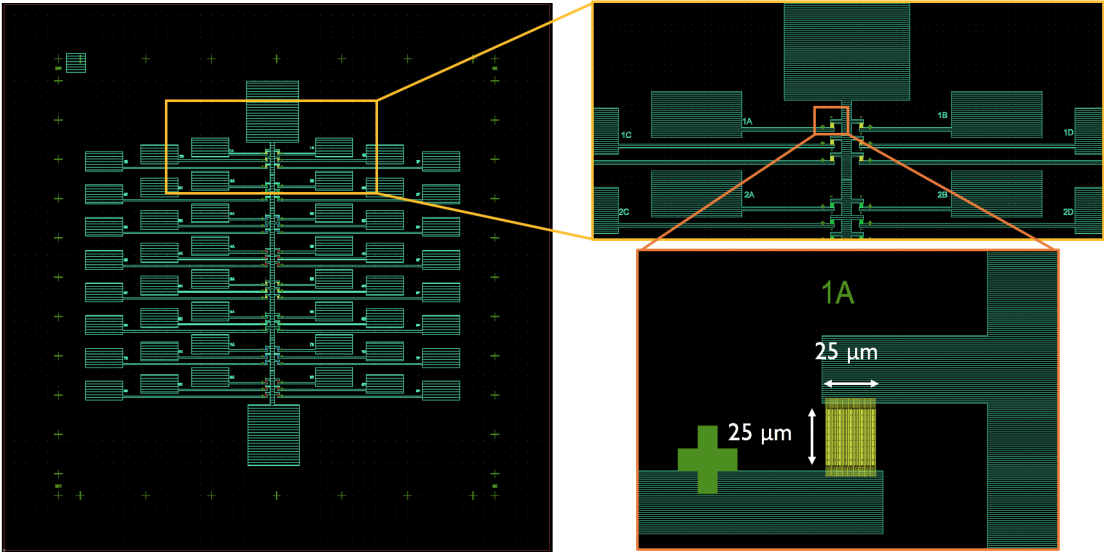


Figure 4.36: Final layout. First zoom in on two groups of arrays with two different doses. Second zoom in on a single array.

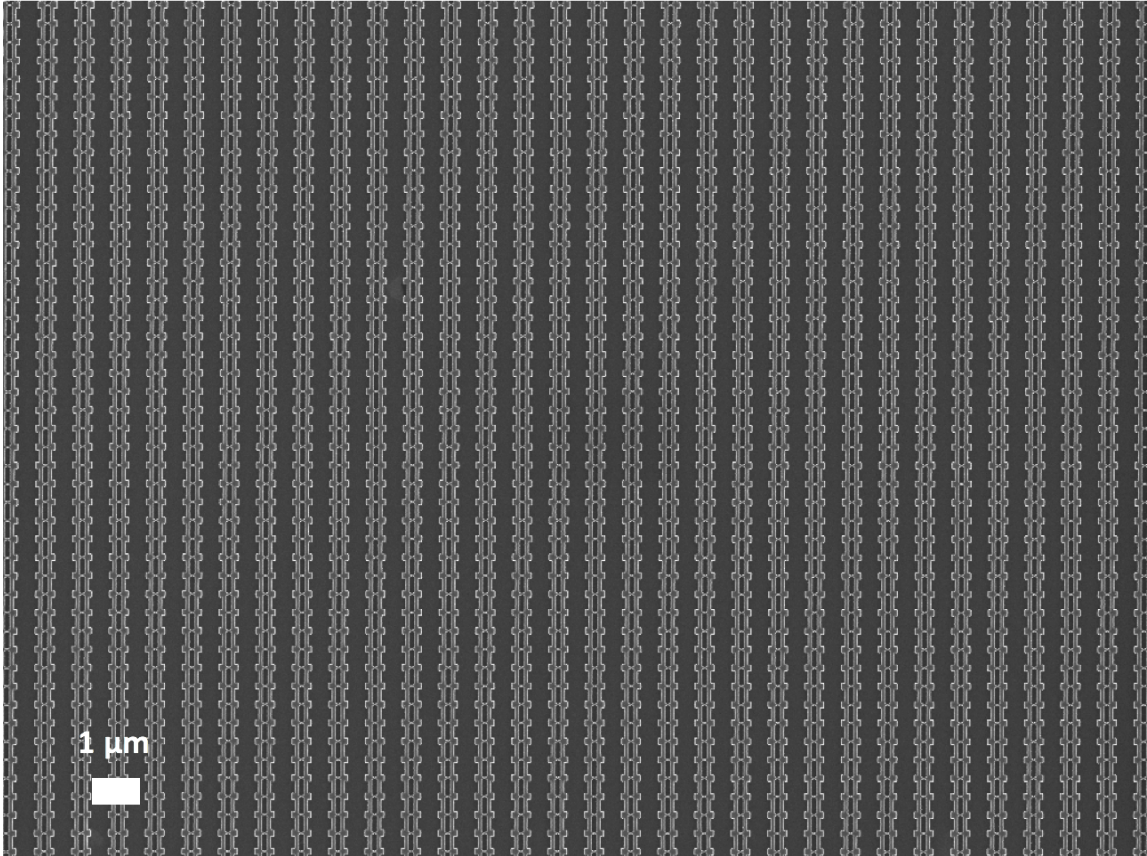


Figure 4.37: Array of bow-ties fabricated on silicon with TiSiON as deposited.

Chapter 5

Electrical and optical testing

In this chapter, we discuss the electrical and optical testing of the bow-tie arrays fabricated on glass, both with TiSiON as deposited and annealed. First we will show the experimental setup we used to carry out the measurements, then the obtained results will be shown. We tested arrays with all disconnected bow-ties (not shorted gaps) and we also performed electromigration on some arrays where some bow-ties were connected. When an array has some shorted gaps, its behavior is resistive and the noise floor is very high. By biasing the structures with a high voltage for a long time, the connected gaps will disconnect by electromigration, allowing us to perform both an electrical and optical characterization of the structures. Thus, it's possible to test very narrow gap arrays as well, where the probability to have some connected gaps becomes very high.

5.1 Electrical testing: experimental setup

The experimental setup we used for the electrical testing is shown in Figure 5.1. We bias a transimpedance amplifier with a voltage source. This voltage is fixed on the other input of the amplifier as well, independently on the current that will flow in. Thus, the voltage source biases the one side of the bow-ties array, while the other one is fixed to ground. We perform a sweep of the voltage in time: when the bias is positive, the electron will be emitted from the grounded bow-ties and the current entering in the amplifier will be negative, whereas the electron will be emitted from the other side of the bow-ties if the bias is negative, causing a positive current to flow in the amplifier. The transimpedance amplifier takes a current as input and translates it into a voltage at the output, amplified with a gain G . We read the output with an oscilloscope. If the bow-ties are all disconnected, then the curve we expect to see in output is given by the Fowler-Nordheim field emission equation (see Eq. (1.1)). We used a Yokugawa GS200 voltage source, a LeCroy WaveSurfer 24Xs 200 MHz oscilloscope and a DDPCA-300 fA transimpedance amplifier.

5.2 Optical testing: experimental setup for photocurrent detection

The experimental setup we used to perform the optical testing of the devices is shown in Figure 5.2. We bias a transimpedance amplifier with a voltage source. This voltage is transferred on the bow-ties array as well. A certain current due to the Fowler-Nordheim field emission mechanism will flow into the amplifier (as explained in Section 5.1). At the same time, we illuminate the bow-ties array with a laser source. The laser pulses go through a chopper, whose chopping frequency

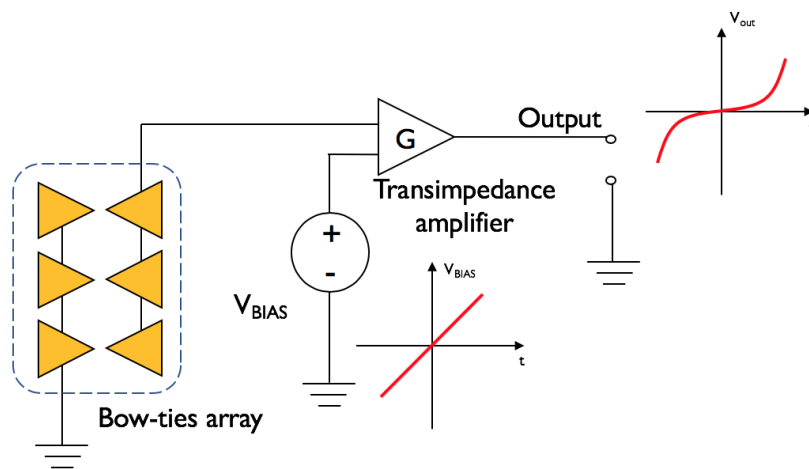


Figure 5.1: Experimental setup for electrical testing.

is set to 100 Hz by the chopper control unit. During its rotation period, the laser will get shut for half the time. Thus, at the output of the amplifier, we will see a square-wave voltage curve, with an offset due to the bias. For half the time, the output will be given just by the bias, due to the chopper's rotation. The chopper control unit is also connected to a lock-in amplifier and its frequency is passed to it as lock-in frequency. The output of the transimpedance amplifier is connected to the input of the lock-in amplifier. Thus, at its output we will read the component of the input voltage at 100 Hz. It means that the offset due to the bias will be cut, since it is at 0 Hz, and we will just read the voltage due to the photocurrent generated by the laser. We will also read a certain phase shift with respect to the chopper duty cycle.

The laser we use for the optical testing is a supercontinuum [66] generated radiation. Supercontinuum generation is a process where a source with a high power in a very limited frequency range is converted to a light with very broad spectral

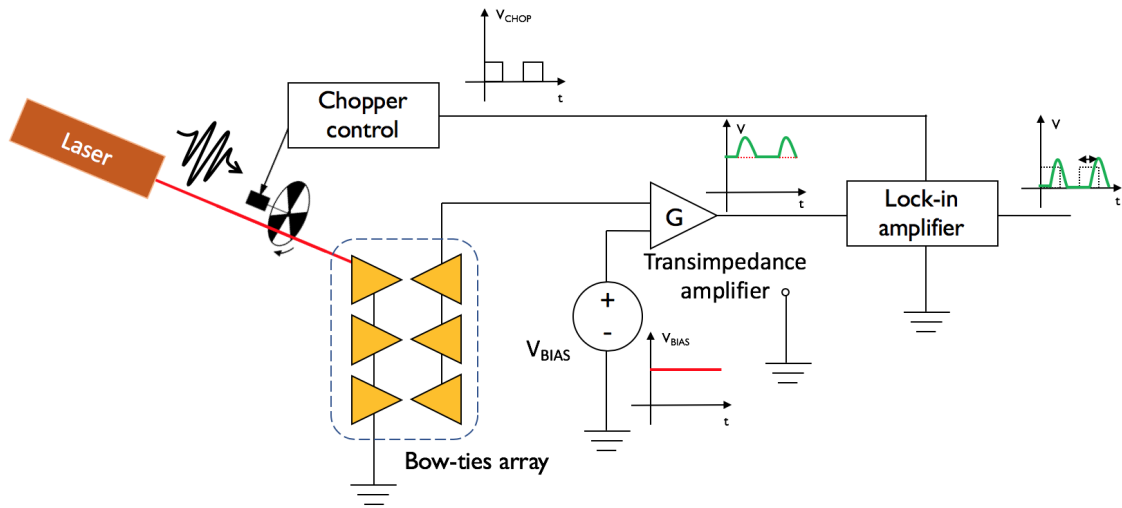


Figure 5.2: Experimental setup for optical testing.

bandwidth thanks to a strongly nonlinear device. Our laser is generated by pulses propagating through an optical fiber [67]. At the end of our setup, we obtain 10-fs long pulses. Figure 5.3 shows the source's spectral power density in the near infrared.

5.3 TiSiON17: film as deposited

We started the electrical testing from the film as deposited, after wire bonding the devices to a PCB. We measured many different devices, and in the following sections we will show the results we obtained with the sets 6C and 6B. The former had all the gaps already disconnected when we started measuring, while the latter had a resistive behavior, so we first needed to electromigrate it and then we were able to test it.

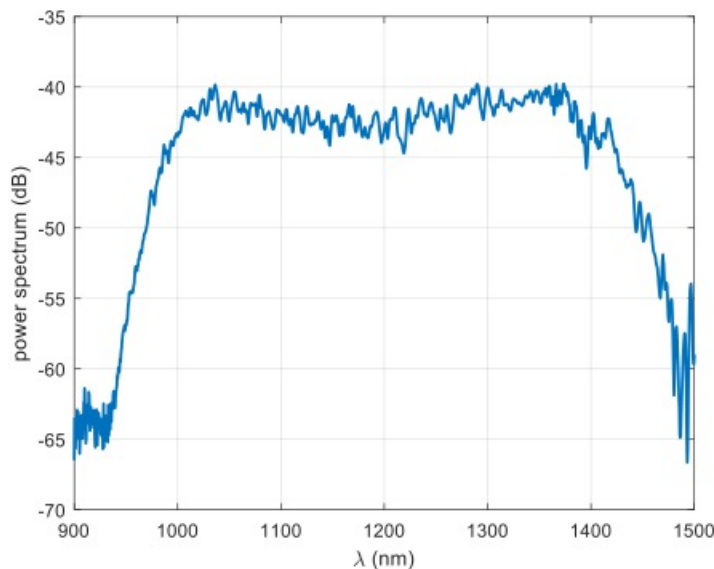


Figure 5.3: Source's spectral power density used for optical testing.

5.3.1 TiSiON17 set 6C

Figure 5.4 shows an SEM image of the set 6C. After fabrication of the pads, the charging issue due to the insulating substrate was solved and we were able to image the fabricated structures. From this image we can measure all the geometric parameters of the bow-ties and carry out a statistic. In Table 5.1 both the nominal parameters set by layout and the ones that were actually obtained with the fabrication are reported.

Parameter	Nominal dimension (nm)	Obtained dimension (nm)
Gap	0	14.0 ± 2.2
Altitude	250	270.2 ± 3.2
Base	187	212.6 ± 3.2
Wires	50	85.9 ± 2.7

Table 5.1: Nominal and obtained dimensions of the TiSiON17 set 6C of bow-ties before testing.

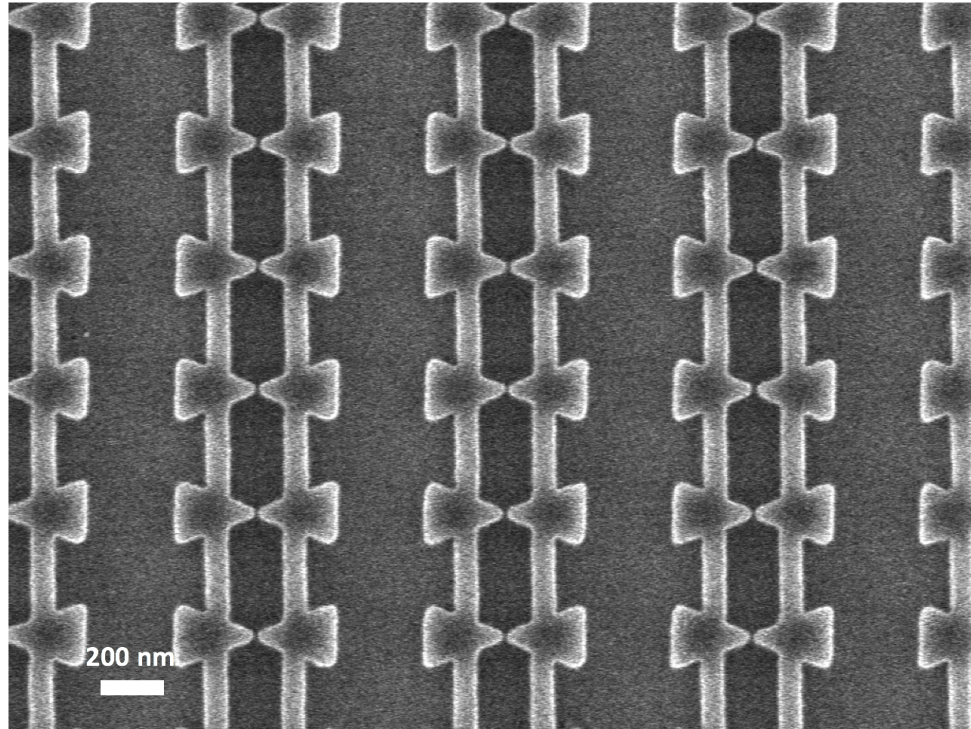


Figure 5.4: SEM image of TiSiON17 set 6C.

Electrical testing

We biased the bow-ties and we performed a voltage sweep going from -10 V up to 10 V. The results we obtained are shown in Figure 5.5. The current has an exponential behavior, which confirms the nature of the emitted electrons. We obtained about $\approx 100 \mu\text{A}$ by applying a 10 V bias. Since every array contains 2016 bow-ties structures, a single bow-tie of the array drives $\approx 5 \text{ nA}$ of current, on average. Note that the current is not perfectly repeatable if we go up and down with the voltage, but this is typical of field emission currents.

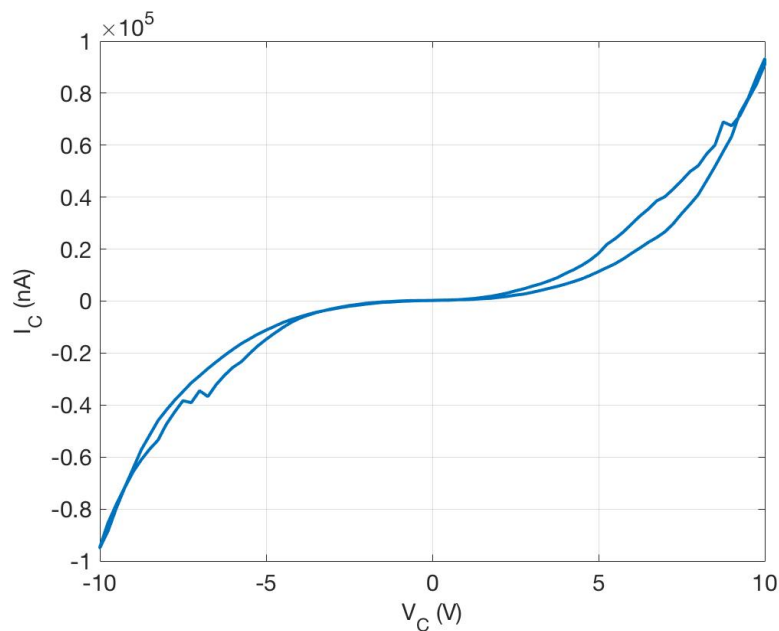


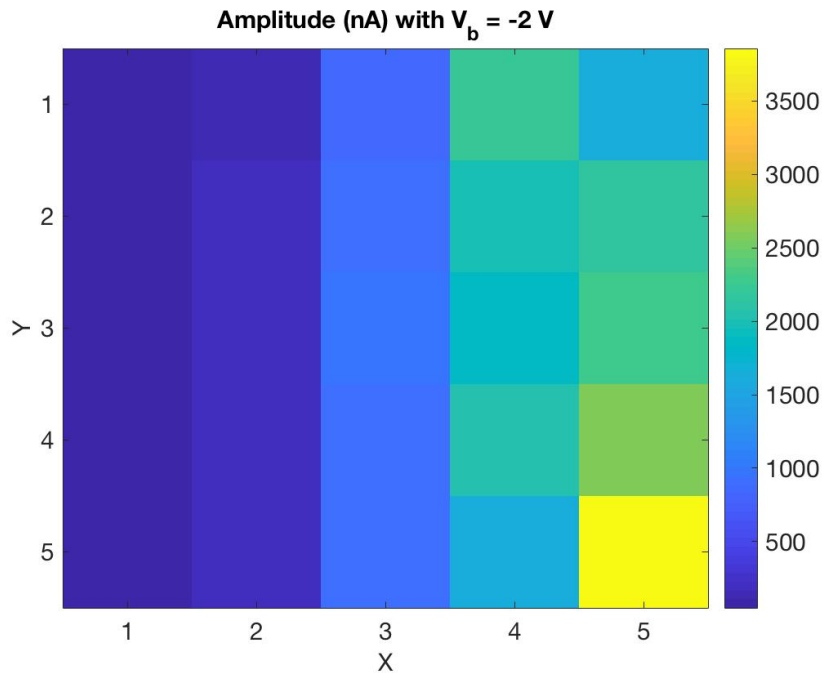
Figure 5.5: Field emitted current of TiSiON17 set 6C. Voltage sweep from -10 V up to 10 V.

Optical testing

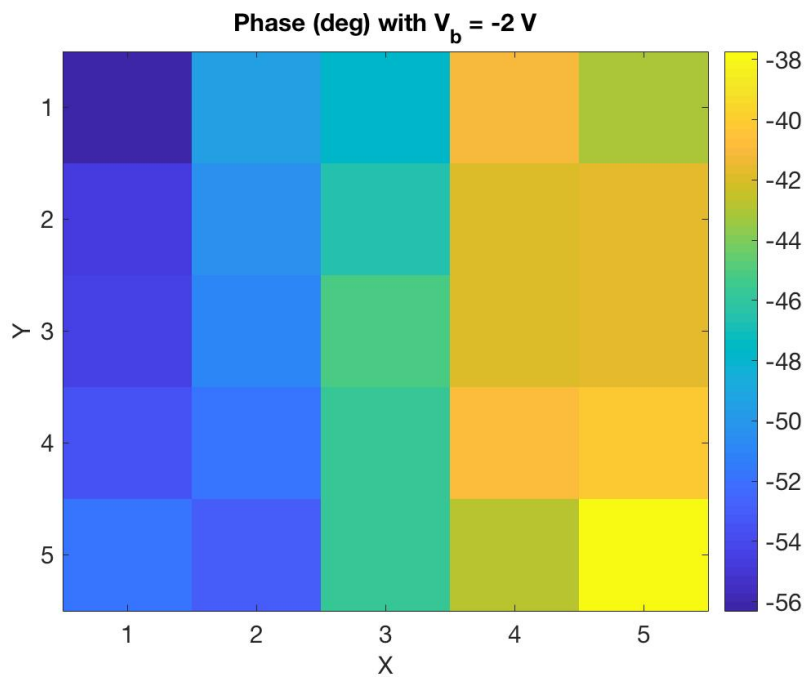
For the optical testing, we made a pzt scan along the x and y axis of the array. We moved the sample along the two directions, so we lighted the array with the laser radiation in different spots in time. For each spot, we measured both the photocurrent and its phase delay with respect to the chopper. We carried out this kind of measurement for different bias voltages on the bow-ties array and we made a map for amplitude and phase delay for each spot that was scanned on the array. The laser power was about 13 mW. An example of these maps is the one reported in Figure 5.6, using a bias voltage of -2 V. Note how the current is not homogeneous over the array, since there are spots that are more active than others. This could be related to the different dopant concentrations in the thin film, as we have seen in

subsection 4.2.2. The different optical properties of the material in different locations could affect the homogeneity of the optical response of the structures in the array. Figure 5.7a shows the amplitude of the voltage at the output due to the photocurrent excited by the laser on the structures. In Figure 5.7b we can see the phase delay of the different spots with respect to the phase of the chopper. The phase indicates the directionality of the current flow. A stable phase also indicates that the measured current indeed comes from photoemission. As we can notice, different spots of the array are more active than others. We made these measurements sweeping the bias from -5 V up to 5 V. Then we calculated the average of both the amplitude and the phase in each map at different bias voltages and we plotted the results in a single curve. Figure 5.7a shows the average photocurrent obtained at different voltages in the whole array, while the phase delay is shown in Figure 5.7b. With a 5 V bias, the total photocurrent generated by the array is about $6 \mu\text{A}$. The laser spot size is of about $2.4 \mu\text{m} \times 5 \mu\text{m}$. When we are lighting the array with the laser, about 40 bow-ties. Thus, when illuminated with an optical power of 13 mW, a single bow-tie structure of the array drives a current of about 150 nA, on average.

It is important to analyze the phase plot carefully. As we can see, the phase switches of 180° when the sign of the bias voltage changes. It means that in a bow-tie, depending on the sign of the applied voltage, one side will emit predominantly to the other. When we change the voltage, since the phase moves of 180° , the predominant emission is transferred to the other side of the bow-tie. Figure 5.8 shows the two cases of positive and negative applied bias voltage. When the bias voltage changes sign, the charge flow switches direction. When we then measure the magnitude and phase of the photocurrent, this change of sign is translated into a phase shift of π . At 0 V, the phase is not well-defined, since the amplitude drops to zero.

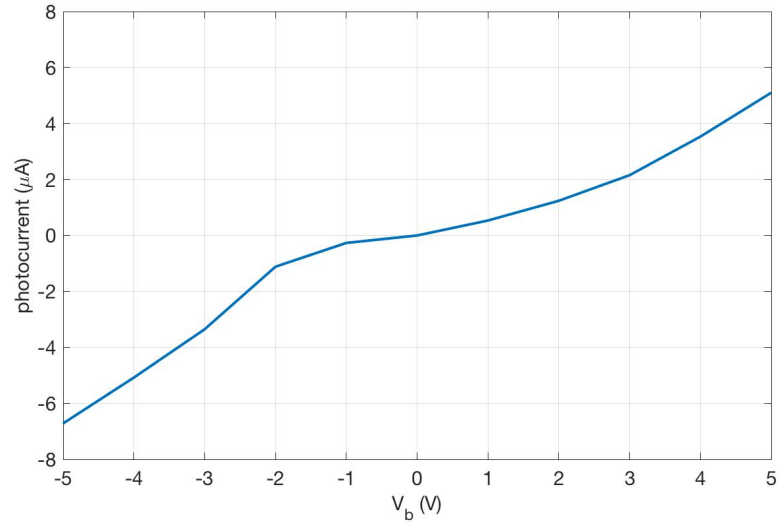


(a) Pzt scan map of voltage amplitude.

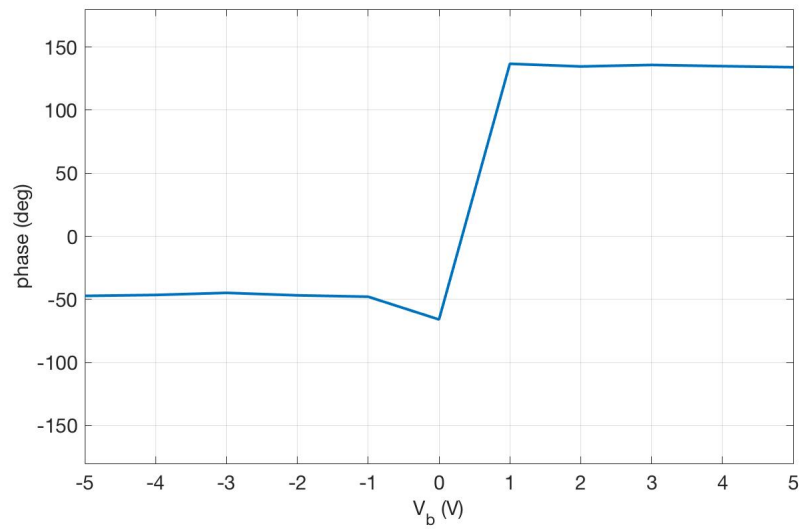


(b) Pzt scan map of phase delay.

Figure 5.6: Pzt scan maps of both voltage amplitude and phase delay on TiSiON17 set 6C with a bias voltage of -2 V. Some regions are more active than others.



(a) Excited photocurrent of TiSiON17 set 6C.



(b) Phase delay of TiSiON17 set 6C with respect to the chopper.

Figure 5.7: Photocurrent and phase delay of TiSiON17 set 6C. Voltage sweep from -5 V up to 5 V.

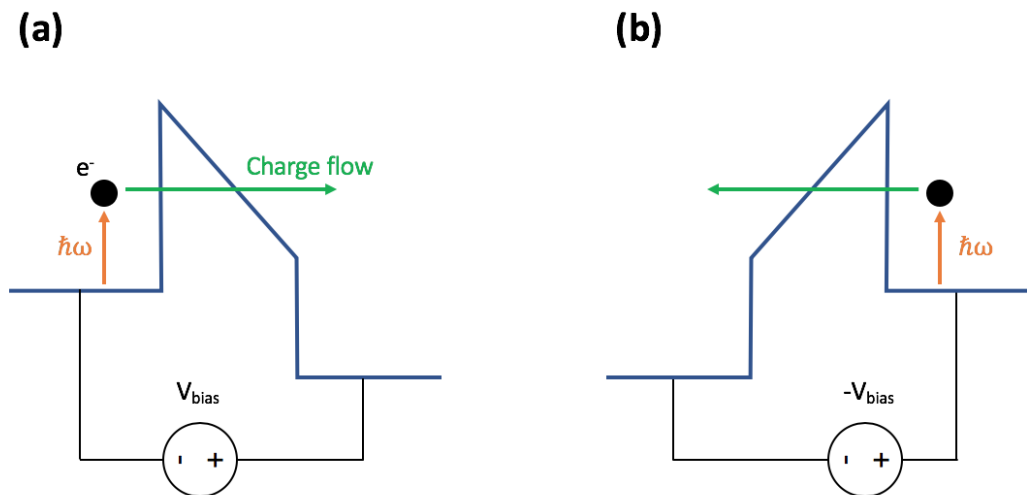


Figure 5.8: Potential of the structures when a bias voltage is applied. An opposite bias flips the current sign, which is equivalent to a phase shift of π . (a) Positive applied bias voltage. (b) Negative applied bias voltage.

As last thing, we tried to see if our bow-ties are CEP sensitive by using a f -to- $2f$ interferometer [68]. We couldn't detect CEP sensitivity, whereas it is possible with gold nanoantennas [8, 15]. We measured an extinction spectrum to evaluate the plasmonic resonance of the structures. Figure 5.9 shows the measured extinction. We don't see a peak, which means the plasmonic resonance either has not been activated due to a too small field enhancement factor or has shifted at lower wavelengths. In our working range of frequencies, we weren't able to obtain optical field photoemission and we are likely working in the multiphoton regime (see subsection 1.2.1).

5.3.2 TiSiON17 set 6B: after electromigration

The dimensions of the geometric parameters of the set 6B are reported in Table 5.2.

The set 6B of TiSiON17 presented some connected gaps in the beginning: the

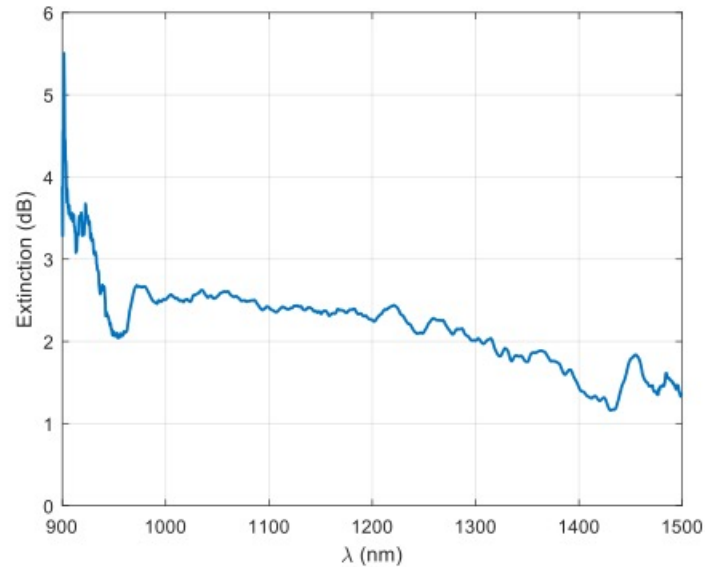


Figure 5.9: Measured extinction spectrum of TiSiON17 set 6C. No peak is present in the near infrared, we are probably working in the multiphoton emission because of a too small field enhancement factor of the structures.

noise floor was really high and its behaviour was resistive. We tried to electromigrate the shorted gaps. We set the Yokugawa GS200 at 10 V and we biased the array for 1 hour. In Figure 5.16 we can see the current variation in time. We can see that a first large step happened in the very first seconds. Other smaller steps kept happening during the remaining time. Each step is due to the opening of some connections: the larger the connection that is opening, the larger will be the variation in the current. Thus, the largest connections opened very fast, since the most of the current was passing through them, whereas smaller connections require longer time, since they drive less current and their resistance is higher.

Parameter	Nominal dimension (nm)	Obtained dimension (nm)
Gap	0	14.6 ± 2.3
Altitude	250	275.9 ± 6.0
Base	187	214.4 ± 3.7
Wires	40	82.1 ± 3.1

Table 5.2: Nominal and obtained dimensions of the TiSiON17 set 6B of bow-ties before testing.

Electrical testing

After electromigrating the array, we measured the electrical current driven by the bow-ties with a sweep of the bias voltage. The results we obtained are reported in Figure 5.11. The behavior is not resistive anymore: the emission is due to the Fowler-Nordheim mechanism. In subsection 5.3.2 we will also make sure this current doesn't come from any leakage in the oxide, which could also have been broken during the electromigration. The curve is not symmetric, which reveals an asymmetry in the fabricated structures. For a bias voltage of -10 V, a single bow-tie structure drives about 3 nA. It is reasonable if we compare it to the set 6C we measured in subsection 5.3.1. Indeed, the current is lower, even if the structures are very similar in terms of dimensions, some columns of bow-ties have been cut during the electromigration, so the actually active devices have decreased in number.

Optical testing

During the optical testing of the set 6B, we carried out a power characterization to evaluate the dependance of the photocurrent on the laser power. We measured the photocurrent with 0.3 mW, 3.8 mW and 9.7 mW, sweeping the bias voltage from -5 V up to 5 V. These measurements also confirm us that the current we are measuring is actually coming from photoemission, since the lock-in amplifier cuts

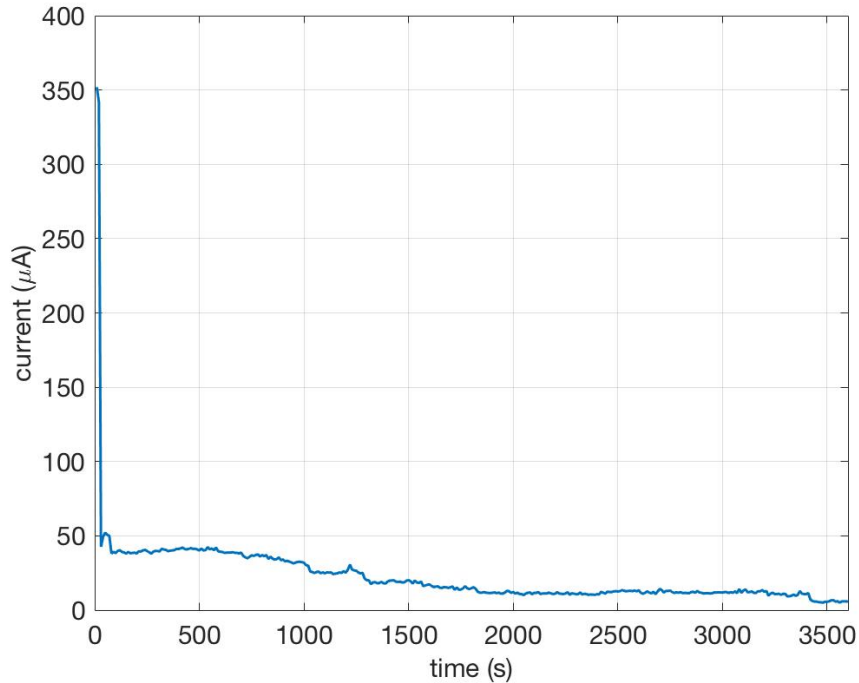


Figure 5.10: Electrical current in time to electromigrate the connected bow-ties of the set 6B. Bias voltage set to 10 V. The steps in the current derive from openings in the connections.

all the contributions deriving from the bias. The results in linear and logarithmic scales are shown in Figure 5.12. From Figure 5.12a, we can see that the trend in linear scale is reasonable, and with the highest power, the array drives about 3-4 nA of photocurrent. Still considering 40 bow-ties illuminated at a time, each bow-tie drives about 100 pA on average. We can see that with low power, the photocurrent is very low, but, by plotting the results in logarithmic scale, all the powers show the same behaviour (see Figure 5.12b).

The phase delay plot (see Figure 5.13) shows the existence of a predominance of one side of the bow-ties on the other depending on how we bias the voltage. The phase is not as constant as it was for the set 6C, but this is probably due to differently

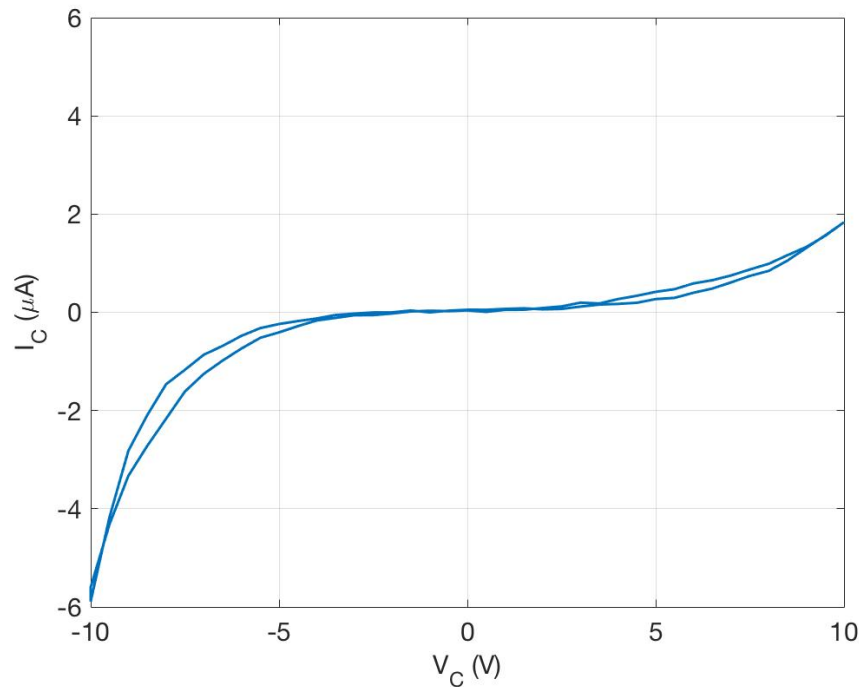
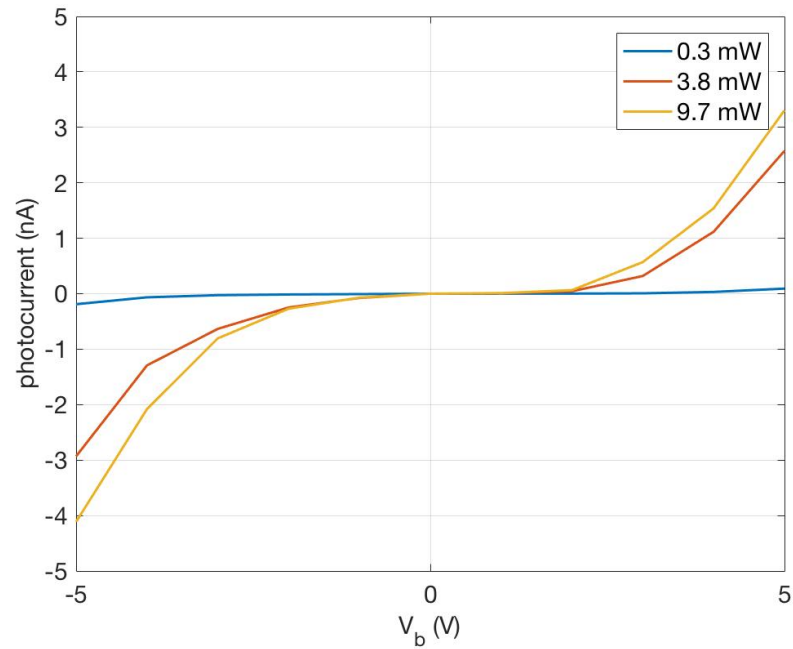


Figure 5.11: Electrical current of the set 6B. Bias voltage sweep from -10 V up to 10 V.

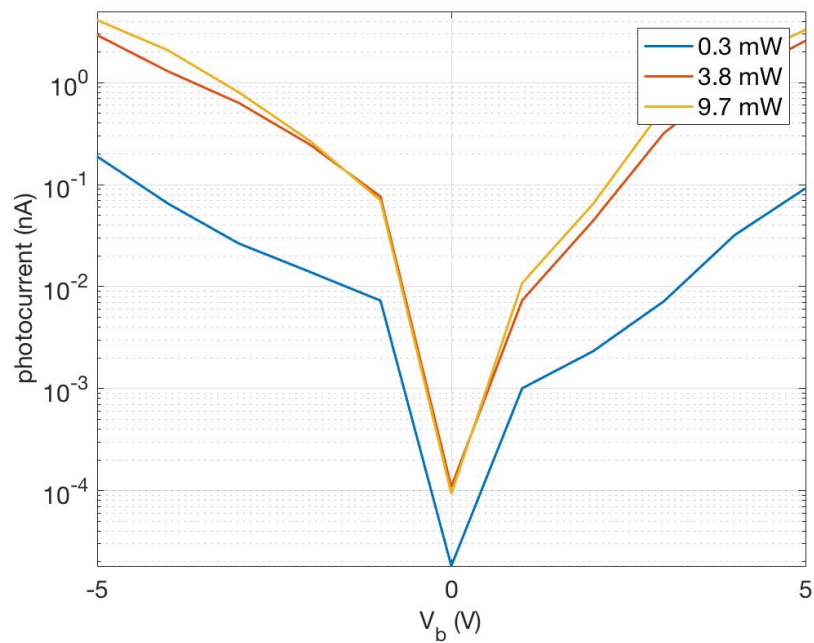
active sites created during the electromigration, which affected the general behavior of the devices in precise regions of the array.

Structures degradation study

We imaged the structures after testing in order to evaluate the degradation of the material derived to electrical and optical stress. Figure 5.14 shows an SEM image of the bow-ties after testing. The gap dimension has reduced from $(14.0 \pm 2.2 \text{ nm})$ to $(10.6 \pm 2.7 \text{ nm})$. Besides, many gaps were smaller than the resolution of the SEM and the charging effects due to the insulating substrate prevented us to image the structures with a larger magnification. We can also see that somewhere some bubbles



(a) Linear plot of the photocurrent for different laser power.



(b) Logarithmic plot of the photocurrent for different laser power.

Figure 5.12: Linear and logarithmic plots of the photocurrent of set 6B after electromigration. Voltage sweep from -5 V up to 5V.

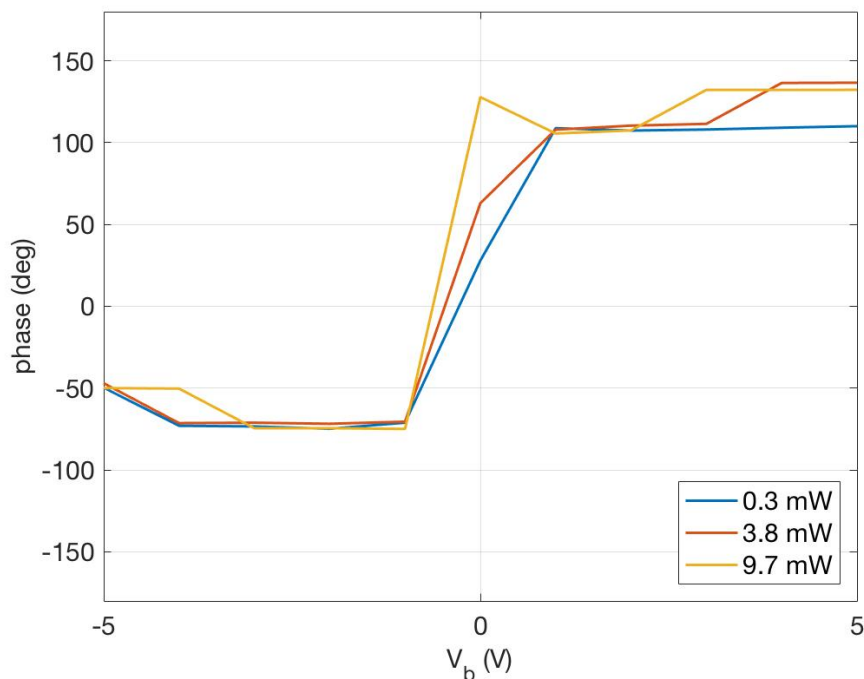


Figure 5.13: Phase delay of the set 6B for different laser power. Bias voltage sweep from -5 V up to 5 V.

appear close to the tip on the surface of TiSiON, modifying the geometric shape of the tip.

As regards the set 6B, the one that also went under electromigration, Figure 5.15 shows the structures after testing. Again, the gap dimension has reduced from $(14.6 \pm 2.3 \text{ nm})$ to $(9.8 \pm 2.0 \text{ nm})$. The decrease in the gap is larger than the one we have seen for the set 6C. It is due to the long electromigration time.

Figure 5.16 shows the main consequences of the electromigration on the array. As we can see, many bubbles are present on the surface of the array and many wires got cut from the leads because of the high current that has flown through them. Entire columns of bow-ties have been electrically disconnected, explaining

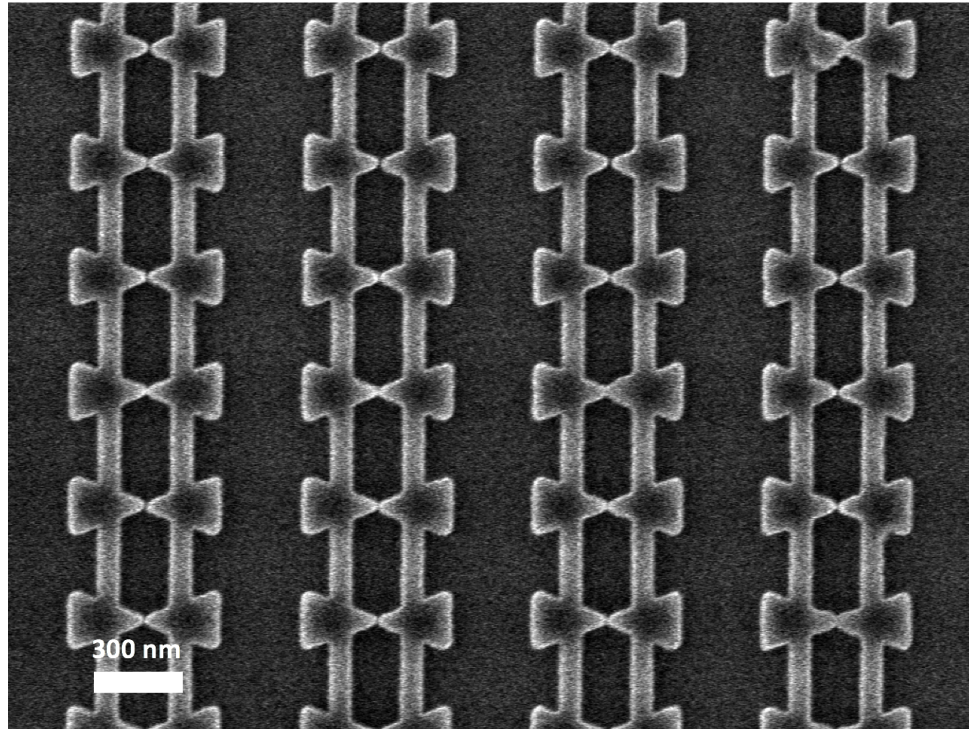


Figure 5.14: SEM image of the set 6C of bow-ties after electrical and optical testing. The gaps shrank and some damages are present on the surface.

the reason why we are measuring a smaller current. Moreover, because of bubbles and surface defects, the surface properties of some structures have been modified, affecting the optical response of those bow-ties to the incident laser radiation. It is interesting to note how the wires where the large amount of current has flown have also become wider than the others.

Compared to gold, which retracts when is heated up with a current flow, TiSiON structures better maintain their shape and the small gaps dimensions between the electrodes. Since the gap is the most important parameter we want to maintain in order to avoid a heavy degradation, TiSiON seems to be a good candidate to withstand harsh environments.

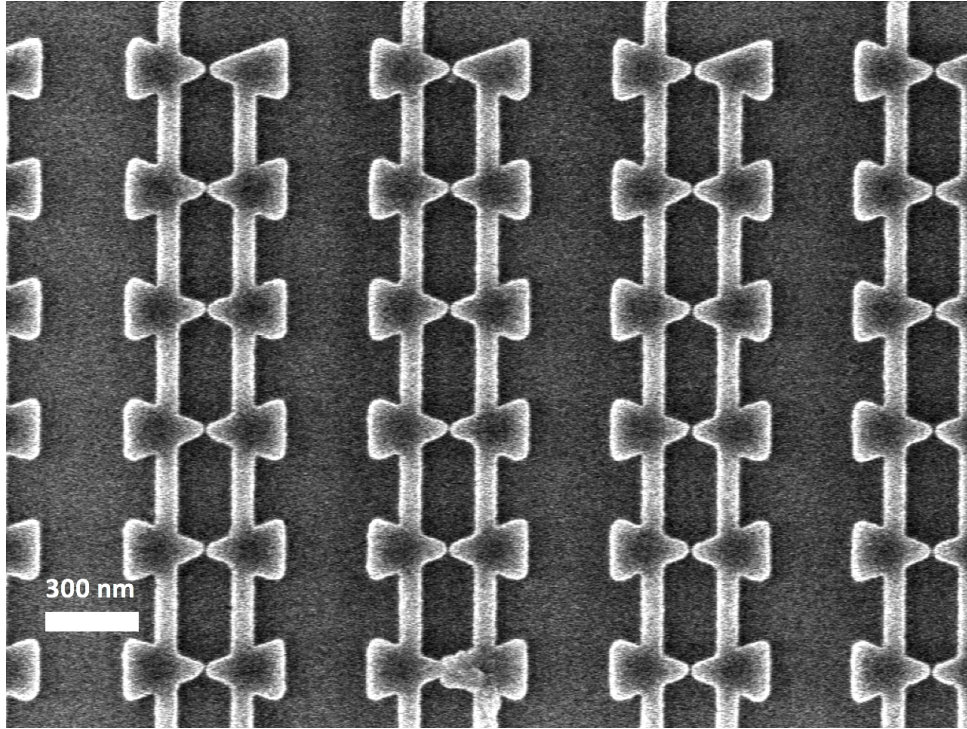


Figure 5.15: SEM image of the set 6B of bow-ties after electrical and optical testing. The gaps shrank.

5.4 TiSiON19 set 7C: annealed film

We performed the same kind of tests for the annealed film. This time, we tested the set 7C, which was characterized by an average gap size of (10.2 ± 1.8) nm. An SEM image of the array before testing is reported in Figure 5.17.

Some gaps of the array were connected, so we first electromigrated those connections. After electromigration, we could see a Fowler-Nordheim-type current passing through the devices. The electrical I-V characteristic of this array is reported in Figure 5.18. The current is comparable to the one we observed for TiSiON17 set 6C, even if we have broken some columns. This is mainly due to the narrower average gap size, which leads to a higher current flowing through each tip.

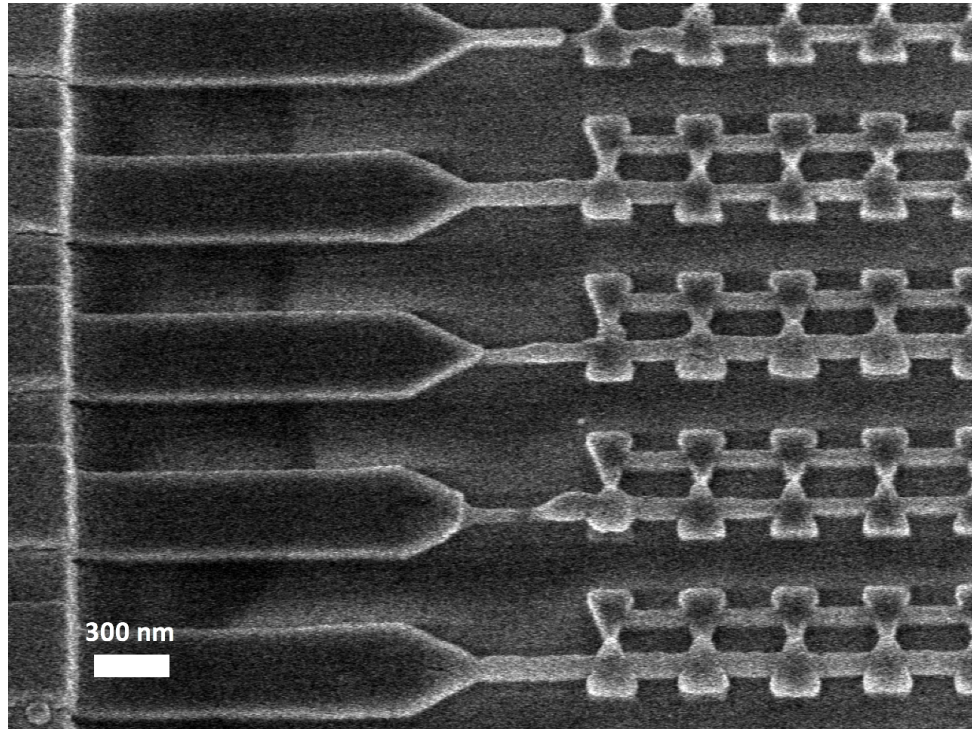


Figure 5.16: SEM image of the leads of the set 6B of bow-ties after electromigration. Many leads got cut and the wires that were connected to them are wider than the others.

For the optical testing, we detected a photocurrent sweeping the voltage from -5 V up to 5 V Figure 5.19a. Also in this case, we obtain a photocurrent comparable to the one we had obtained for the film as deposited in subsection 5.3.1. Such a high current after electromigration is mainly due to the narrow gaps and to the better optical properties achieved by the annealed film (see Section 2.2). Figure 5.19b shows that there is a predominance of a side of the array over the other depending on the direction of the DC current flow due to the applied bias.

As last thing for the optical testing, we couldn't detect CEP sensitivity with the annealed TiSiON film either. A further improvement of the optical properties by engineering the dopant concentrations is needed to achieve a higher field enhance-

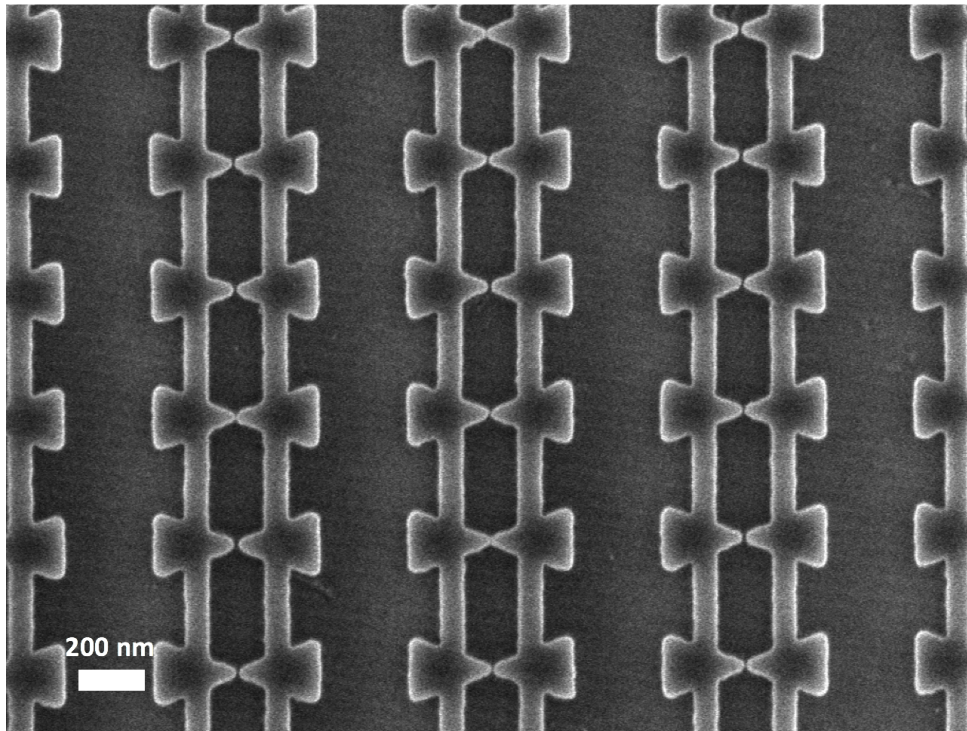


Figure 5.17: SEM image of TiSiON19 set 7C before testing.

ment factor to allow the devices to work in the optical-field emission regime (see subsection 1.2.1).

Finally, we imaged the devices after testing. Figure 5.20 shows a part of the array that didn't get seriously damaged during the testing. The resolution of the SEM wasn't able to image the small gaps between the tips, also because of the usual charging effects due to the insulating substrate. Nevertheless, we can clearly deduce that the gaps have shrunk down to few nanometers during testing. The field emission behaviour is ensured by the Fowler-Nordheim I-V curve we got during the electrical testing. Figure 5.21a shows a damaged part of the array due to the high currents that flew through the structures during the electromigration process. We can notice that many contact leads got broken, some gaps got damaged and have an unusual

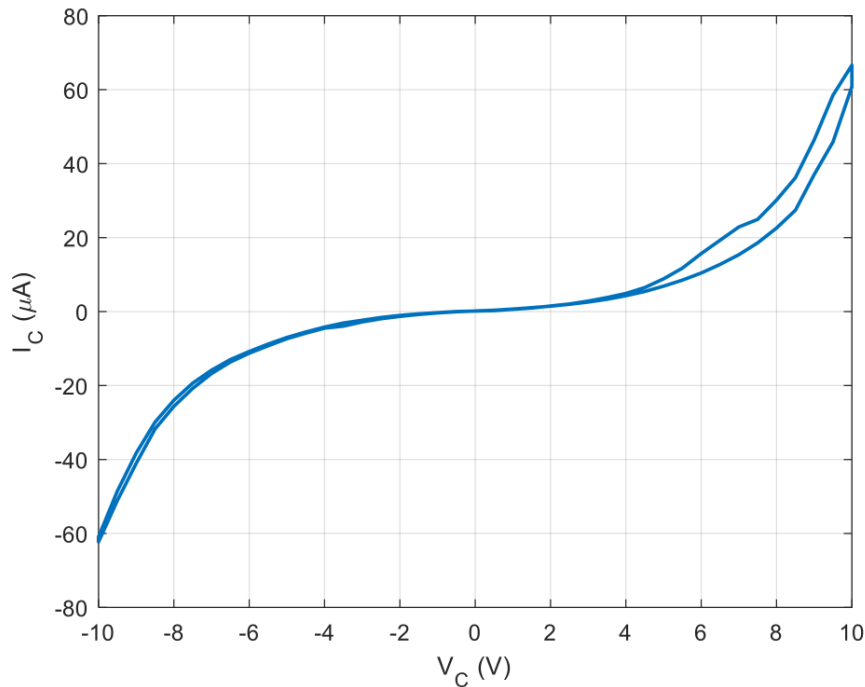
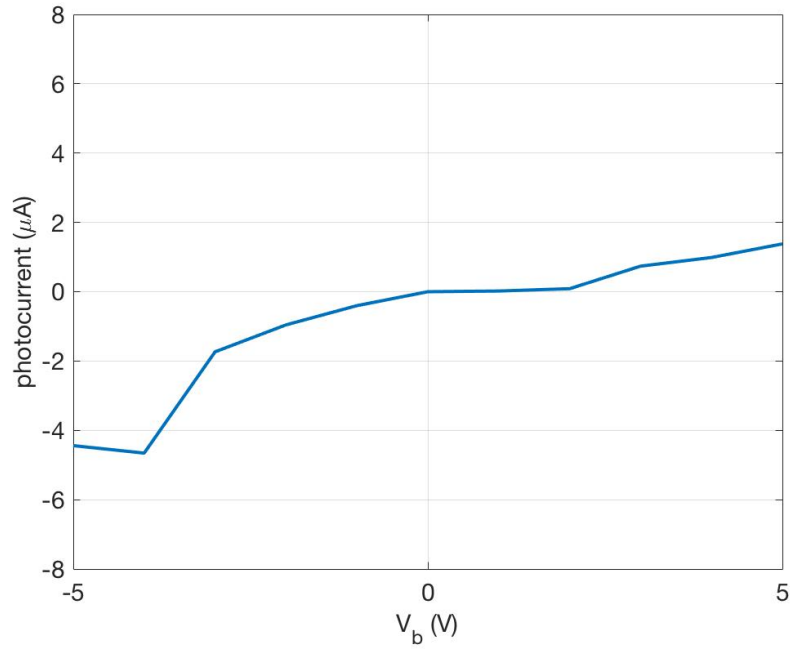


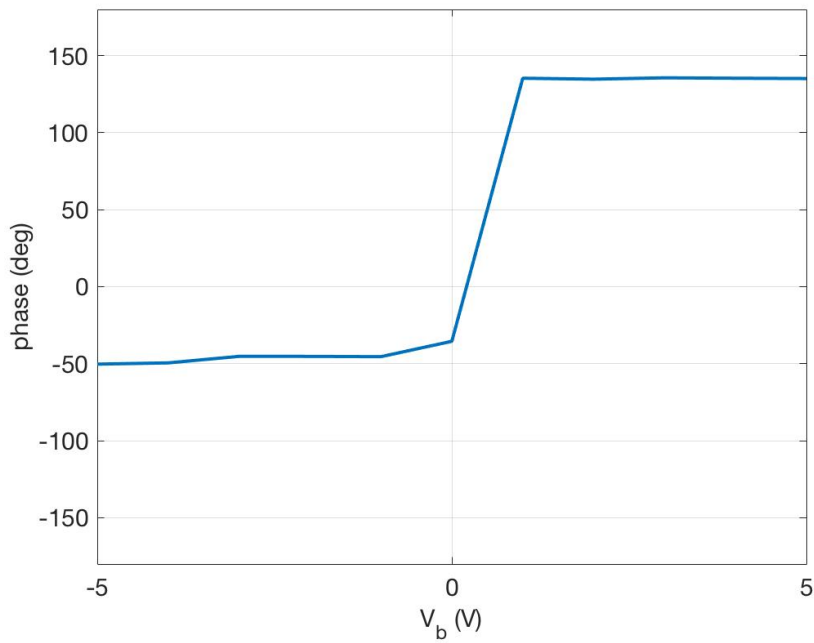
Figure 5.18: I-V curve of TiSiON19 set 7C after electromigration.

tridimensional shape due to some bubbles that are raised on the surface. Some bowties also seem to have gotten fused. Figure 5.21b is a tilted SEM image offering a different point of view to image the surface damages. These damages heavily affect the surface properties of the material.

The high photocurrent we obtained during the optical testing represents an interesting result, considering the serious surface damages we have seen and taking into account how many columns of the array aren't contributing to the conduction anymore. It could be reasonable to fabricate slightly larger gaps and let them shrink down by burning the tips with high voltages, in order to save as many columns as possible and to avoid the formation of surface defects that could seriously affect the optical properties of the devices.



(a) Excited photocurrent.



(b) Phase delay.

Figure 5.19: Excited photocurrent and phase delay of TiSiON19 set 7C after electromigration. Voltage sweep from -5 V up to 5V.

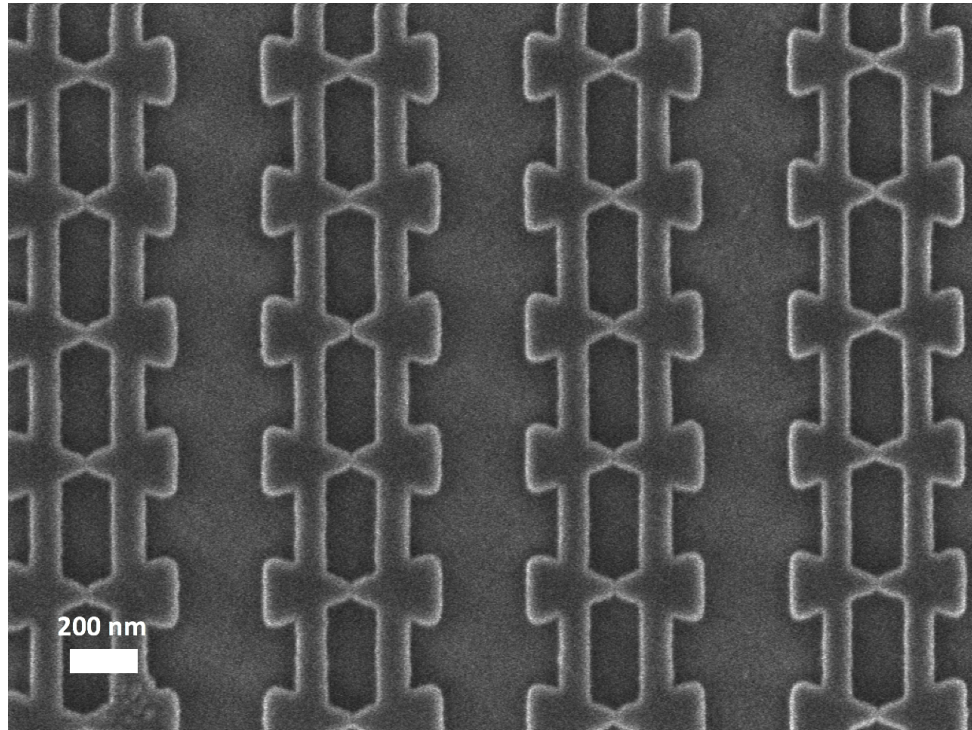
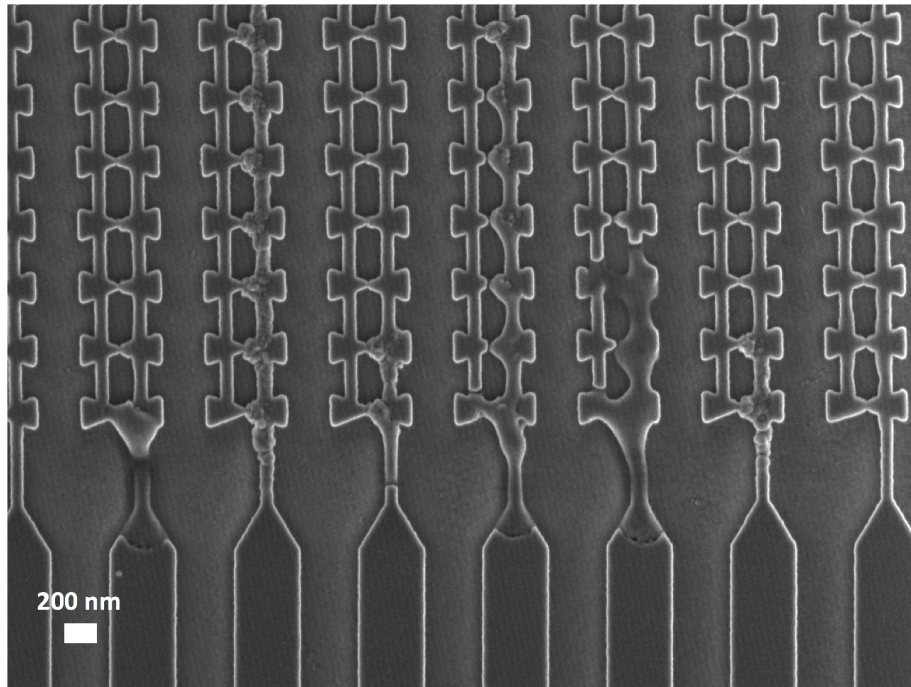
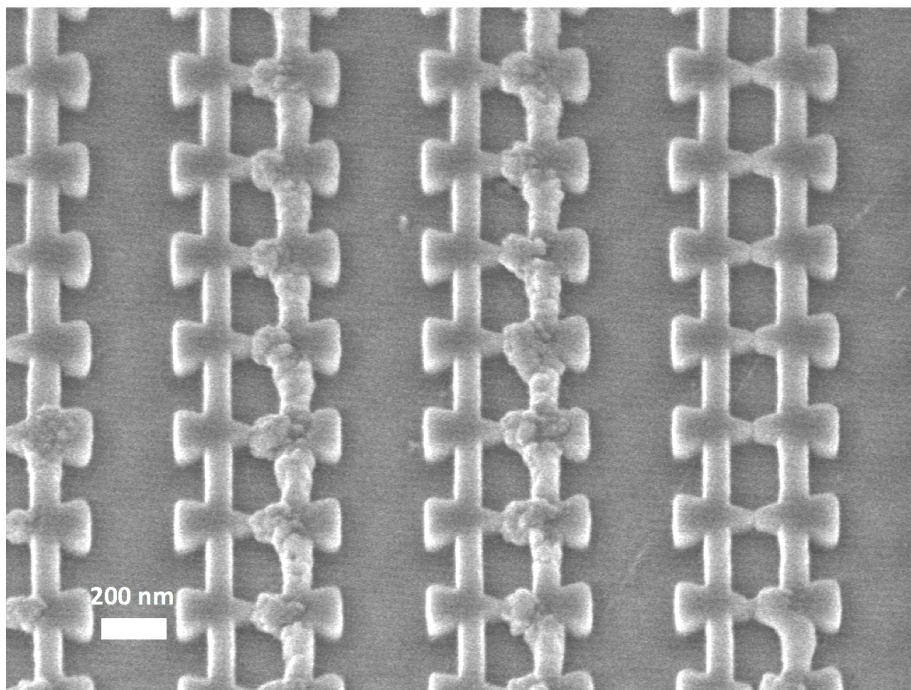


Figure 5.20: SEM image of TiSiON19 set 7C after testing. No damage is present in this area and we can see how the gaps shrank down to dimensions smaller than the SEM resolution.



(a) Top view of the damages: some leads got broken, some bubbles appeared on the surface of many tips, some bow-ties got fused.



(b) Tilted image of the bubbles appeared on the tips' surface.

Figure 5.21: SEM images showing the damages the electrical and optical testing caused to TiSiON19 set 7C.

Chapter 6

Conclusions and future work

In this chapter we will review the work performed for this master's thesis project, pointing out the results we obtained and the future work that should be carried out for further development of this project.

6.1 Summary

In this master's thesis project we have studied novel field electron emission devices fabricated with a new refractory plasmonic material: titanium silicon oxynitride. In particular, we focused on the fabrication of bow-tie nanostructures that can be used both in vacuum nanoelectronics and in optoelectronics applications. We studied the film both as deposited and after annealing at 700 °C. We started from the simulation of the device, comparing TiSiON with a state-of-the-art plasmonic material like gold and with other materials that are not usually used for plasmonic applications. We pointed out the advantages and the drawbacks of using such a new material. Noble metals are largely used in plasmonics, but their applications are limited due to low

melting points, narrow bandwidth, lack of compatibility with the CMOS processing and degradation in harsh environments. TiSiON is thought to be helpful in resolving these issues. We also carried out a study in the geometric parameters (Chapter 2). Then we developed a reliable fabrication process based on reactive ion etching for bow-tie nanostructures arrays. The TiSiON film was first sputtered on silicon and glass substrates at Boston University. We studied different types of etchants both for dry and wet etching procedures. Both fluorine and chlorine chemistries have been analyzed for reactive ion etching. We mainly focused on CF_4 , CF_4/O_2 and Cl_2 plasmas. Furthermore, a thorough study on materials (i.e. Al, Mo, Ti, Cr, Al/Cr bi-layer) used as hard mask has been carried out (Chapter 4). Finally, we tested the fabricated devices electrically and optically. In particular we measured the Fowler-Nordheim tunnelling current and the photocurrent produced by an exciting laser. We also analyzed the devices before and after testing, in order to evaluate the degradation induced by the testing (Chapter 5)

6.2 Results and conclusions

From the simulations we carried out, we pointed out that the optical response of TiSiON shows a stronger resemblance to an exciting incident field than gold, even if it does not reach the same performances as gold in terms of field enhancement factor, due to a lower quality factor. The field enhancement of the bow-ties increases with the triangle altitude, the base/altitude ratio and is inversely proportional to the gap size between the electrodes. The annealed film shows higher quality factor and field enhancement compared to the film as deposited.

We successfully fabricated bow-tie nanostructures array by using an Al/Cr bi-layer hard mask in a reactive ion etching procedure based on CF_4/O_2 plasma. We

developed a reliable process to achieve sub-10-nm gaps and aspect ratio larger than 5. We connected the bow-ties arrays to Ti/Au contacts with direct writing laser photolithographic procedures.

The electrical testing showed that a fabricated single bow-tie structure of the array with a 14-nm wide gap, after activation, can drive an average current of about 5 nA with a bias voltage of 10 V. Optically, the same activated bow-tie structures can drive 150 nA on average with a bias voltage of 5 V. Nevertheless, we could not detect CEP sensitivity of the devices and the extinction spectra didn't show a peak in the near infrared. We are likely not achieving a sufficiently large field enhancement factor to allow us to work in the optical-field emission regime, thus why we are still working in the multiphoton emission regime. Furthermore, we proved that if some bow-ties are connected, we can electromigrate the single gap or the entire column of the array were the connected devices are. We analyzed the degradation of the devices after testing: some bubbles appear on the surface of the devices where a high current has passed (i.e. during the electromigration process), and the gap sizes decrease after testing. In order to maintain the surface properties, it would be convenient to fabricate a bit larger gaps to ensure all of them are disconnected, and shrink the gaps down to about 10 nm by activating the structures with a proper bias voltage and current flow.

6.3 Future works

Future works for improvements in this project are:

- Engineering of TiSiON elemental concentrations to enhance the field enhancement and the plasmonic response of the structures. With a larger field enhance-

ment, we might be able to measure the CEP of an incident ultrafast laser, as it is already possible with gold bow-tie structures;

- Carry out a thorough experimental study on fabricated structures with different geometrical parameters;
- Further characterization of the difference between experimental results coming from as deposited and annealed TiSiON.

Bibliography

- [1] S. Nie, S. R. Emory, "Probing Single Molecules and Single Nanoparticles by Surface-Enhanced Raman Scattering", *Science*, 275, 1102–1106 (1997).
- [2] K. Imura, T. Nagahara, H. Okamoto, "Near-Field Optical Imaging of Plasmon Modes in Gold Nanorods", *J. Chem. Phys.*, 122, 154701–154705 (2005).
- [3] Y. Zhao, A. Alú, "Tailoring the Dispersion of Plasmonic Nanorods to Realize Broadband Optical Meta-Waveplates", *Nano Lett.*, 13, 1086–1091 (2013).
- [4] K. M. Mayer, J. H. Hafner, "Localized Surface Plasmon Resonance Sensors", *Chem. Rev.*, 111, 3828–3857 (2011).
- [5] J. N. Anker, W. P. Hall, O. Lyandres, N. C. Shah, J. Zhao, R. P. Van Duyne, "Biosensing with Plasmonic Nanosensors", *Nat. Mater.*, 7, 442–453 (2008).
- [6] D. M. Koller, A. Hohenau, H. Ditlbacher, N. Galler, F. Reil, F. R. Aussenegg, A. Leitner, E. J. W. List, J. R. Krenn, "Organic Plasmon-Emitting Diode" *Nat. Photonics*, 2, 684–687 (2008).
- [7] G. Volpe, M. Noack, S. S. Aćimović, C. Reinhardt, R. Quidant, "Near-Field Mapping of Plasmonic Antennas by Multiphoton Absorption in Poly(methyl methacrylate)", *Nano Lett.*, 12, 4864–4868 (2012).

-
- [8] W. P. Putnam, R. G. Hobbs, P. D. Keathley, K. K. Berggren, F. X. Kärtner, "Optical-field-controlled photoemission from plasmonic nanoparticles", *Nat. Phys.* 13, 335–339 (2017).
- [9] T. Rybka et al., "Sub-cycle optical phase control of nanotunnelling in the single-electron regime", *Nat. Photon.* 10, 667–670 (2016).
- [10] M. Kruger, M. Schenk, P. Hommelhoff, "Attosecond control of electrons emitted from a nanoscale metal tip", *Nature* 475, 78–81 (2011).
- [11] G. Herink, D. R. Solli, M. Gulde, C. Ropers, "Field-driven photoemission from nanostructures quenches the quiver motion", *Nature* 483, 190–193 (2012).
- [12] M. Schenk, M. Krüger, P. Hommelhoff, "Strong-field above-threshold photoemission from sharp metal tips", *Phys. Rev. Lett.* 105, 257601 (2010).
- [13] T. Paasch-Colberg et al., "Solid-state light-phase detector", *Nat. Photon.* 8, 214–218 (2014).
- [14] B. Ahn et al., "Attosecond-controlled photoemission from metal nanowire tips in the few-electron regime", *APL Photon.* 2, 036104 (2017).
- [15] P. D. Keathley, W. P. Putnam, P. Vasireddy, R. G. Hobbs, Y. Yang, K. K. Berggren, F. X. Kärtner, "Vanishing carrier-envelope-phase-sensitive response in optical-field photoemission from plasmonic nanoantennas", *Nat. Phys.* (2019).
- [16] Richard G. Hobbs, Yujia Yang, Arya Fallahi, Philip D. Keathley, Eva De Leo, Franz X. Kärtner, William S. Graves, Karl K. Berggren, "High-Yield, Ultrafast, Surface Plasmon-Enhanced, Au Nanorod Optical Field Electron Emitter Arrays", *ACS Nano*, Vol. 8, No. 11, 11474-11482 (2014).

-
- [17] Y. Wang, A. Capretti, and L. Dal Negro, "Wide tuning of the optical and structural properties of alternative plasmonic materials", *Opt. Mater. Express* 5(11), 2415–2430 (2015).
- [18] D. Shah, H. Reddy, N. Kinsey, V. M. Shalaev, and A. Boltasseva, "Optical properties of plasmonic ultrathin TiN films", *Adv. Opt. Mater.* 5(13), 1700065 (2017).
- [19] W. A. Britton, Y. Chen, L. Dal Negro, "Double-plasmon broadband response of engineered titanium silicon oxynitride", *Optical Materials Express* (2019).
- [20] Fowler Ralph Howard, Nordheim L., "Electron emission in intense electric fields", 119. *Proc. R. Soc. Lond. A*.
- [21] J.-W. Han, D.-I. Moon, M. Meyyappan, *Nano Lett.* 2017, Supporting Information 17, 4, 2146-2151.
- [22] Fujimoto J. G., Liu J. M., Ippen E. P. and Bloembergen N., *Phys. Rev. Lett.* 53 1837 (1984).
- [23] Katherine A. Willets, Richard P. Van Duyne, "Localized Surface Plasmon Resonance Spectroscopy and Sensing", *Annu. Rev. Phys. Chem.* 2007. 58:267-97.
- [24] Van Duyne R. P., "Molecular plasmonics", *Science* 306:985–86 (2004).
- [25] Haes A. J., Haynes C. L., McFarland A. D., Zou S., Schatz G. C., Van Duyne R. P., "Plasmonic materials for surface-enhanced sensing and spectroscopy". *MRS Bull.* 30:368–75 (2005).

- [26] Brockman J. M., Nelson B. P., Corn R. M., "Surface plasmon resonance imaging measurements of ultrathin organic films", *Annu. Rev. Phys. Chem.* 51:41–63 (2000).
- [27] *J. Phys. Chem. B* 2003, 107,3,668-677 (2002).
- [28] Keldysh L. V., "Ionization in the field of a strong electromagnetic wave", *Sov. Phys.—JETP* 20 1307 (1965).
- [29] Bunkin F. V. and Fedorov M. V., *Sov. Phys.—JETP* 21 896 (1965).
- [30] Augst S., Meyerhofer D. D., Strickland D. and Chint S. L., *J. Opt. Soc. Am. B* 8 858 (1991).
- [31] M. Krüger, M. Schenk, M. Förster and P. Hommelhoff, "Attosecond physics in photoemission from a metal nanotip", *J. Phys. B: At. Mol. Opt. Phys.* 45 (2012) 074006.
- [32] Urcan Guler, Alexandra Boltasseva, Vladimir M. Shalaev, "Refractory Plasmonics", *Science*, Vol. 344 (2014).
- [33] P. R. West, S. Ishii, G. V. Naik, N. K. Emani, V. M. Shalaev, and A. Boltasseva, "Searching for better plasmonic materials," *Laser Photonics Rev.* 4(6), 795–808 (2010).
- [34] G. V. Naik, A. Boltasseva, "Semiconductors for plasmonics and metamaterials," *Phys. Status Solidi Rapid Res. Lett.* 4(10), 295–297 (2010).
- [35] C. Bohren and D. Huffman, "Absorption and Scattering of Light by Small Particles", 1983.

-
- [36] Alexandre Vial, Anne-Sophie Grimault, Demetrio Macías, Dominique Barchiesi, and Marc Lamy de la Chapelle, "Improved analytical fit of gold dispersion: Application to the modeling of extinction spectra with a finite-difference time-domain method", *Physical Review B* 71, 085416 (2005).
- [37] J. Y. Horiba, "Lorentz dispersion model", *Spectroscopic Ellipsometry*, Technical Note 08.
- [38] Thomas Mikael Schmidt, "Engineering of gold and aluminum plasmonic structures: Fabrication and fluorescence enhancement", PhD thesis, 2013.
- [39] Sebastian Thomas, Georg Wachter, Christoph Lemell, Joachim Burgdörfer and Peter Hommelhoff, "Large optical field enhancement for nanotips with large opening angles", *New J. Phys.* 17, 063010 (2015).
- [40] *Optical Engineering* 32 (10), 246—2451 (October 1993).
- [41] Nan Yao and Alexander K. Epstein, "Surface nanofabrication using focused ion beam", *Microscopy: Science, Technology, Applications and Education*.
- [42] Ludwig Reimer, "Transmission Electron Microscopy - Physics of Image Formation and Microanalysis", Springer-Verlag Berlin Heidelberg GmbH, 1984.
- [43] R. F. Egerton, "Electron energy-loss spectroscopy in the TEM", *Rep. Prog. Phys.* 72 (2009).
- [44] FS-1 Manual, Film Sense Multi-Wavelength Ellipsometers, 2017.
- [45] *Journal of Vacuum Science and Technology B: Microelectronics and Nanometer Structures Processing, Measurement, and Phenomena* 21, 2163 (2003).

-
- [46] Journal of Vacuum Science and Technology A 19, 455 (2001).
- [47] Journal of Vacuum Science and Technology B 34, 02M102 (2016).
- [48] Journal of Vacuum Science and Technology A 13, 335 (1995).
- [49] Chang Ju Choi et al 1998 Jpn. J. Appl. Phys. 37 801.
- [50] Journal of Applied Physics 49, 3796 (1978).
- [51] Jae-Whan Kim, Yong-Chun Kim, Won-Jong Lee, "Reactive ion etching mechanism of plasma enhanced chemically vapor deposited aluminum oxide film in CF₄/O₂ plasma", J. Appl. Phys. 78 (3) (1995).
- [52] Journal of Vacuum Science and Technology B: Microelectronics Processing and Phenomena 8, 5 (1990).
- [53] Vladimir Bliznetsov, Hua Mao Lin, Yue Jia Zhang, David Johnson, "Deep SiO₂ etching with Al and AlN masks for MEMS devices".
- [54] K Grigoras, L Sainiemi, J Tiilikainen, A Säynätjoki, V-M Airaksinen, S Franssila, "Application of ultra-thin aluminum oxide etch mask made by atomic layer deposition technique", Journal of Physics: Conference Series 61 (2007).
- [55] MICROPOSIT MF-CD-26 developer, Material Safety Data Sheet, DOW.
- [56] Aluminum Etch Type A, Material Data Sheet, Transene.
- [57] Frederik Ceyssens, Robert Puers, "Deep etching of glass wafers using sputtered molybdenum masks", Journal of Micromechanics and Microengineering, Volume 19, Number 6 (2009).

-
- [58] N. Khamnualthong et al., "Study of Chromium Hard Mask Formation and Wall Angle Control for Deep Etching Application", *Procedia Engineering* 32 (2012) 922 – 928.
- [59] *Journal of Vacuum Science and Technology B* 35, 06GB01 (2017).
- [60] Adam Richard Pawloski, Bruno La Fontaine, Harry J. Levinson, Stefan Hirscher, Siegfried Schwarzl, Klaus Lowack, Frank-Michael Kamm, Markus Bender, Wolf-Dieter Domke, Christian Holfeld, Uwe Dersch, Patrick Naulleau, Florian Letzkus, and Joerg Butschke, "Comparative study of mask architectures for EUV lithography", *Proc. SPIE* 5567, 24th Annual BACUS Symposium on Photomask Technology, (6 December 2004).
- [61] Md Nazmul Hossain et al., *2014 Nanotechnology* 25 355301.
- [62] CR7 Chrome Etch without Surfactant, Perchloric Acid Type, Material Data Sheet, KMG.
- [63] Carmen Ostwalda, Hans J. Grabkeb, "Initial oxidation and chromium diffusion. I. Effects of surface working on 9–20% Cr steels", *Corrosion Science* 46 (2004) 1113–1127.
- [64] MicroChem, LOR and PMGI Resists, Data-sheet.
- [65] Microposit S1800 Series Photo Resists, Shipley.
- [66] John M. Dudley, "Supercontinuum generation in photonic crystal fiber", *Rev. Mod. Phys.*, Vol. 78, No. 4 (2006).
- [67] William P. Putnam, Phillip D. Keathley, Jonathan A. Cox, Andreas Liehl, Alfred Leitenstorfer, and Franz X. Kärtner, "Few-cycle, carrier-envelope-phase-

stable laser pulses from a compact supercontinuum source", *J. Opt. Soc. Am. B* 36, A93-A97 (2019).

- [68] U. Keller, "Ultrafast solid-state laser oscillators: a success story for the last 20 years with no end in sight", *Appl Phys B* 100: 15–28 (2010).